STRUCTURE AND DYNAMIC STUDIES OF THE NUCLEAR PORE COMPLEX AT THE SINGLE-MOLECULE LEVEL

By

Nicholas E. Dickenson
B.S., Lewis Clark State College, 2003

Submitted to the Department of Chemistry and the Faculty of the
Graduate School of the University of Kansas in partial fulfillment of the
requirements for the degree of Doctor of Philosophy

Robert C. Dunn, Ph.D. (Chairman)

Craig E. Lunte, Ph.D.

Heather Desaire, Ph.D.

Michael A. Johnson, Ph.D.

William D. Picking, Ph.D.

Date Approved: July 9, 2008

The Dissertation Committee for Nicholas E. Dickenson certifies
that this is the approved version of the following dissertation:

STRUCTURE AND DYNAMIC STUDIES OF THE NUCLEAR PORE COMPLEX AT THE SINGLE-MOLECULE LEVEL

Committee:

Robert C. Dunn, Ph.D. (Chairman)

Craig E. Lunte, Ph.D.

Heather Desaire, Ph.D.

Michael A. Johnson, Ph.D.

William D. Picking, Ph.D.

Date Approved: July 9, 2008

ABSTRACT

Nicholas E. Dickenson, Ph.D.
Department of Chemistry, July 2008
University of Kansas

Nuclear pore complexes are large macromolecular structures forming the only known direct route across the double bilayer membrane of the nuclear envelope. Depletion of calcium from within this cisternal space has been directly linked to alterations in NPC conformation and possibly regulation of cyto-nuclear transport. Perhaps the most striking effect is the appearance and apparent displacement of a central mass or plug within the lumen of the pore upon depletion of cisternal calcium. Although the Ca^{2+} dependence on the relative location of the central mass within the pore has been well-studied, neither its identity nor functional role have been elucidated.

Similarities in the size and shape of the central mass to those of vault ribonucleoproteins has led to speculation that vaults caught transiting the nuclear pore may represent this enigmatic structure, however, no direct evidence has been presented. Here, this relationship is directly investigated through measurements of Förster resonance energy transfer (FRET) which is an optical technique sensitive to spatial relationships on the nanometer level. These studies found not only that vaults specifically colocalize with NPCs at the nuclear envelope, but that their spatial relationship is sensitive to cisternal calcium levels in much the same manner as that between NPCs and the central mass. This strongly suggests that transiting vaults may in fact represent the NPC central mass.

Although FRET measurements located vaults to NPCs in a calcium-dependent manner, they lack the ability to locate vaults to individual pores, which would further confirm the role of vaults as the central mass. Near-field scanning optical microscopy (NSOM) is a scanning probe technique which affords the simultaneous collection of high-resolution fluorescence and topographical data and has the ability to directly visualize the specific location of vaults at NPCs. While NSOM offers a unique

ability to probe biological samples on a scale that is consistent with protein interactions, many challenges have limited its application in the biological sciences. One concern involves heat transfer from the NSOM probe to the sample. Previous studies in our lab found minimal sample heating from NSOM probes fabricated with the pulling method. In an effort to explore alternate NSOM probe designs, sample heating from the more efficient chemically etched NSOM probes was investigated with the use of a thermochromic polymer. It was found that sample heating resulting from etched probes is strikingly similar to that arising from probes produced by the pulling method, although the ultimate light-induced failure mechanisms were found to be unique. Ultimately, this demonstrates that NSOM utilizing either etched or pulled probes should be amendable with biological samples allowing for its use to probe the interaction between vaults and NPCs. The resulting high-resolution images precisely located vaults to NPCs in isolated nuclear membranes, further suggesting that transiting vaults represent the central mass within NPCs.

Both the FRET and NSOM studies investigating vaults and NPCs were able to provide sensitive measurements mapping the location and interactions between them. In order to probe transport dynamics through nuclear pores, a novel single-molecule fluorescence transport assay was developed. Investigations of single-molecule transport times of small fluorescent dextrans unveiled a dependence of dwell times on the availability of the phenylalanine-glycine (FG) rich repeat domains located within the lumen of the pore. These domains had previously been implicated in facilitated transport of large cargo, but now it seems likely that they also play a role in regulating passive diffusion.

Dedicated to Liz and Alana

Acknowledgements

As I look back on the last five years that I have spent here in grad school at KU, I realize the number of people who have been instrumental in every accomplishment that I can lay claim to. Specifically, I believe that the success of any graduate student is a direct result of his/her advisor. For this reason, I owe a great thanks to Bob Dunn for not only guiding my personal knowledge and growth as a scientist, but making the lab a fun and relaxing environment to work in. I am sure that the skills that I have developed under his guidance, as well as those which he exhibits and I someday hope to hone, will follow me in many aspects of my life and prove invaluable as I venture into the "real world". Again, Bob, thank you for everything you have done to make my time at KU a truly positive experience.

I would also like to thank the other members of the Dunn group for their help and friendship during my time in the lab. Specifically, I would like to thank Beth Erickson, Olivia Mooren, and David Moore as they welcomed me into the lab when I first joined. Beth and Olivia were second-year graduate students from whom I was able to not only draw scientific knowledge, but enjoyed countless drunken conversations about random topics that I seem to not be able to recall at the moment. Dave was an extremely valuable resource and instrumental in helping me to develop cell culture and immunolabeling techniques for the vault studies. The current members, Philip Livanec and Heath Huckabay have proven great additions to the group and I am sure that they will be able to carry on the legacy of the Dunn lab far after I am gone.

The faculty and staff in the KU chemistry department are exceptional and I specifically appreciate the personal interest that the faculty has taken in the success of the graduate students and me personally. Although looking at the department from the outside in, one might think that the faculty are responsible for the successful day-to-day operation of the department, but after five years on the "inside", I realize that it is the support staff that really gets things done. Specifically, I would like to

acknowledge Jan Akers, Sonjia Payne, Susan Teague, Yvonne Martinez, Teri Herberger, Gary Webber, Carla Ramirez, and Ann Smith. I always knew that if I really needed something done, I could ask one of them and if they didn't know how to do it, they certainly knew who to contact in order to find out. I hope that wherever I go, I am able to find people who are as good at their jobs and as willing to help as they have been.

At the beginning of my third year, I was lucky enough to be included into the NIH Dynamic Aspects in Chemical Biology Training Program. Being a part of the program has been a great experience and I think that it has given me a unique insight into the importance of collaboration and the need for cross-disciplinary research. I would like to specifically thank professors Kristin Bowman-James and Paul Hanson for making the time in their busy schedules to direct the program and make it possible. Their hands-off approach really allowed us (the trainees) to organize and run the program, giving us a valuable experience that I doubt most graduate students have the opportunity to go through.

I would like to be able to tell you that every minute of the last five years of my life have been spent slaving away in the research lab, but I know that no one would believe me and it would be a terrible lie. I have had the opportunity spend time with some great friends here and their support and friendship is something that I will remember and cherish for the rest of my life. Specifically Megen Miller, Matt Culpepper, Ryan Shook, Joe Nguyen, Olivia Mooren, Beth Erickson, Phil Livanec, and Maggie Livanec have proven to be the kind of friends that you can count on no matter what the circumstances. I have always heard that it is easy to have a lot of friends in life, but finding one true friend can be nearly impossible. I want to thank Phil for being that true friend and I consider myself lucky found this friendship. It was never too hard to talk him into ditching lab early after one of my experiments went to Hell in order to go play some pool or darts and drink away our sorrows. So, for that and everything else, thank you Phil.

When I first came to KU and joined the graduate program, I thought that earning my degree would be the best thing to come of my decision, however, it turns out that it is the third best thing. It was through the program that I met Wanda Liz Cuadrado Santana, a gorgeous, spunky Puerto Rican girl also attending graduate school in chemistry. After a lot of smooth talking and a couple of years, she became Wanda Liz Dickenson and made me the happiest I have ever been. That was until we had our beautiful daughter, Alana Marie Dickenson, making me now not only a lucky husband, but also a proud father. Liz and Alana have been my support system and I don't believe that I could be where I am without them by my side. Liz and Alana… I love you and thank you for everything.

Finally, I would like to thank my family who has always supported me in everything that I have chosen to do. My parents taught me that when you want something, you need to work hard and never give up until you achieve it. I think that it is this perseverance that has gotten me to this point and will continue to allow me to achieve the goals that I set for myself. I have also been lucky to have brothers who are also great friends and confidants. So, to my family, I just want to thank you for everything that you have done and continue to do for me and it is for your unconditional love and support that I will always be grateful.

Table of Contents

Chapter 1: Nuclear Pore Structure and Function

Chapter 2: Localizing Vault Ribonucleoproteins to the Nuclear Pore Complex

Chapter 3: Extending of Near-Field Scanning Optical Microscopy to Biological Samples

Chapter 4: Characterization of Power-Induced Heating and Damage in Fiber Optic Probes for Near-Field Scanning Optical Microscopy

Chapter 5: High-Resolution Near-Field Scanning Optical Microscopy Studies of the Nuclear Membrane and Nuclear Pore Complexes

Chapter 6: Single-Molecule Transport Measurements through NPCs

Chapter 7: Conclusions and Future Directions

List of Figures

List of Tables

Chapter 1

Nuclear Pore Structure and Function

1.1 Structure of the Nuclear Pore Complex

The nuclear envelope (NE) is a double bilayer membrane which encases the genetic material of all eukaryotic cells. Regulation of the passage of essential cellular components across the nuclear envelope is accomplished by large protein channels called nuclear pore complexes (NPCs). These complex channels represent the sole route of cyto-nuclear transport across both bilayers of the nuclear envelope. Because of the importance in regulating movement across the nuclear envelope, much effort has been devoted toward the study of the NPC architecture and its functional role in facilitating transport.

The functional importance of NPCs is exemplified by their ubiquitous appearance and highly conserved structure across eukaryotic cells. Structurally, NPCs are comprised of ~30 different proteins known as nucleoporins or Nups[1, 2] with an estimated molecular weight of ~125 MDa in vertebrates while the similarly structured yet smaller version in yeast is ~60 MDa.[3, 4] Each of the nucleoporins exist in multiples of eight copies within the complex, giving rise to an observed eight-fold rotational symmetry in NPCs. Though many of the specific roles of these Nups remain unclear, their identification and characterization has led to many insights into the pore structure. Figure 1.1 shows a cartoon representation of a nuclear pore complex located within the nuclear envelope. This illustration outlines the unique nature in which the nuclear envelope bilayers are continuous at NPCs, allowing for the primarily soluble complex to span both membranes and form a channel between the cytoplasmic and nuclear compartments of the cell. Because of this unique geometry, and the lack of traditional trans-membrane proteins, early studies of NPCs described them as nature's grommets.[5] It is now known that the complex does contain at least two trans-membrane proteins which may act to anchor the NPCs to the NE.[6-8]

The large size and flexible nature of NPCs preclude the use of many traditional approaches such as NMR and crystallography for studying in tact NPCs, although studies of individual NPC components have been achieved. Recently, the atomic structure of the heterodimeric Sec13-Nup145C complex of the NPC core domain was achieved by x-ray diffraction, forming the groundwork for an atomic model of the nuclear pore complex.[9] Complete views of NPC structure however, have relied heavily on high-resolution techniques such as electron microscopy (EM) in order to structurally map nuclear pores.[10-16] A myriad of such EM studies in conjunction with three-dimensional reconstructions and density mapping have produced detailed renditions of nuclear pore complexes, from which much structural information has been delineated. As shown in Fig. 1.1, NPCs consist of cytoplasmic and nuclear rings which reside on the respective faces of the NE and are connected by eight spoke-like structures spanning the nuclear envelope.[1, 2, 15, 17] Mimicking the symmetry of the spokes, eight short filaments reach ~50 nm into the cytoplasm while eight longer fibrils form a basket-like structure on the nuclear face, terminating at a narrow ring approximately 120 nm from the nuclear face.[17, 18] The Nups that comprise these filaments include highly conserved regions of short amino acid repeats containing primarily the hydrophobic residues phenylalanine and glycine (FG).[4, 19, 20] The exact function of these filaments is not completely clear, though many studies have implicated FG rich Nups in the transport of cargo. This proposed function was supported by the direct visualization of the cytoplasmic filaments interacting with gold coated nucleoplasmin molecules in a series of EM images.[21] The filaments were apparently recruiting the cargo to the NPC channel in preparation for transport. Further implications of FG rich Nups in transport will be discussed in detail in subsequent sections.

1.2 Proposed Mechanisms of Translocation through the Nuclear Pore Complex

As previously mentioned, NPCs play an essential role in the transport and regulation of cargo across the nuclear envelope. Though the exact mechanisms of cyto-nuclear transport are not known, it is well understood that the specific role of NPCs is mandated largely by the size of the transiting cargo.[22] Studies suggest that molecules smaller than ~10kDa passively diffuse through a small channel in the pore driven by concentration gradients between cytoplasmic and nuclear spaces.[22-24]

Transport of large molecules greater than ~40 kDa, on the other hand, have been shown to be highly dependent on a number of more complex factors including a Ran-GTP/GDP gradient,[25, 26] the expression of either nuclear localization (NLS) or

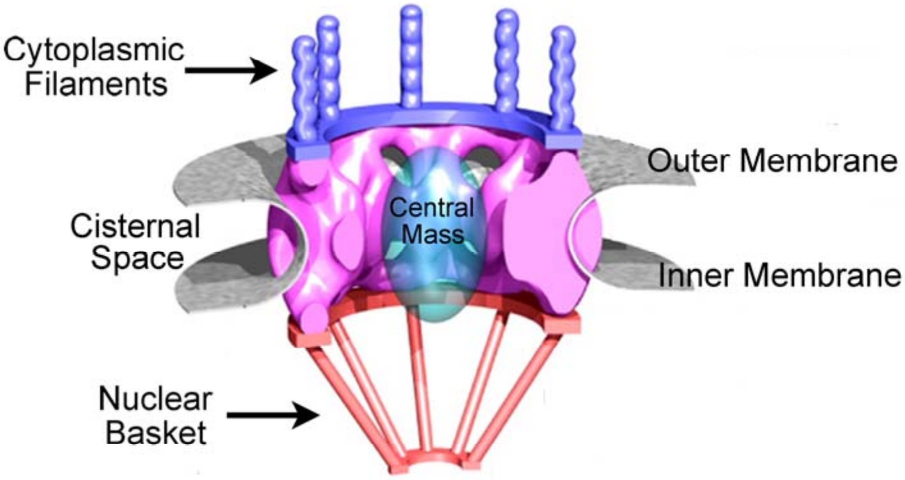

Figure 1.1 Three-dimensional reconstruction of a nuclear pore complex (NPC). The cytoplasmic and nuclear rings are connected by eight spoke-like structures, forming the pore across both the outer and inner membranes of the nuclear envelope. Cytoplasmic filaments are found extending from the cytoplasmic face while nuclear filaments form a basket-like structure extending into the nucleoplasm. The unidentified central mass and the cisternal space are also shown. This figure was modified with permission from reference 14.

nuclear export sequences (NES),[27, 28] and a complex class of proteins collectively known as karyopherins.[29-31] A basic diagram outlining the currently understood cascade of events involved in active transport is outlined in Figure 1.2. It has been found that large cargo crossing the nuclear envelope into the nucleoplasm must express a short, primarily basic amino acid sequence known as a nuclear localization sequence (NLS).[23] For active transport into the nucleus, the molecule to be transported must first complex with importin α through a specific recognition site for the NLS.[32, 33] The importin α-cargo heterodimer then binds to another import chaperone, importin β, which allows for the initiation of active import through the hypothesized docking of the import complex with the FG rich cytoplasmic filaments which will be detailed later.[34, 35] The exact mechanism by which the trimeric complex passes through the NPC is not clear, although it is known that once it reaches the nucleoplasm, it dissociates through the binding of Ran-GTP. As illustrated, the importin β/Ran-GTP complex is then shuttled back to the cytoplasm while importin α must bind a complex of the exportin CAS and Ran-GTP in order to be recycled back to the cytoplasm as importin α is unable to bind Ran-GTP alone.[36] Once in the cytoplasm, the hydrolysis of Ran-GTP to Ran-GDP by a Ran GTPase activating protein, Ran-GAP, releases the import karyopherins freeing them to bind yet another cargo molecule.[37]

A similar energy dependent mechanism exists for nuclear export of large molecules containing a short amino acid sequence primarily comprised of hydrophobic leucine residues referred to as a nuclear export sequence (NES).[28, 38] For the active transport of molecules from the nucleus into the cytoplasm, the cargo first binds with the exportin CRM1 and Ran-GTP through specific recognition of the NES. The complex then transits the NPC into the cytoplasm where the hydrolysis of the Ran-GTP by Ran-GAP results in the release of the cargo and exportin chaperone, followed by the return of the empty CRM1 to the nucleus.[39] These examples outline the importance of maintaining a Ran-GDP/Ran-GTP gradient across the NE as it is responsible for the directionality of cyto-nuclear transport. This gradient is maintained by the specific shuttling of Ran-GDP into the nucleus by nuclear transport factor 2 (NTF2), where it is then phosphorylated by Ran-GEF.[40, 41] Though many key components have been identified and mechanisms of active import and export through nuclear pore complexes have been elicited, the actual mode of translocation of molecules through the pore is not well understood and remains a topic of great interest.

As described previously, Nups containing various repeating patterns of the amino acids phenylalanine and glycine (FG) have been found in the internal lumen of the pore as well as the periphery of the membrane rings. More specifically, the FG repeats appear as intrinsically unfolded lengths of protein containing as many as 50 repeats of short hydrophobic sequences of the form GLFG or FxFG (where x represents any amino acid, but generally a small residue such as Gly, Ser, or Ala) separated by longer hydrophilic spacers.[4] The exact role of the FG repeats in transport through the pore is not known, but they are thought to interact with specific karyopherins during transport.[34, 42] Their necessary involvement in transport has been

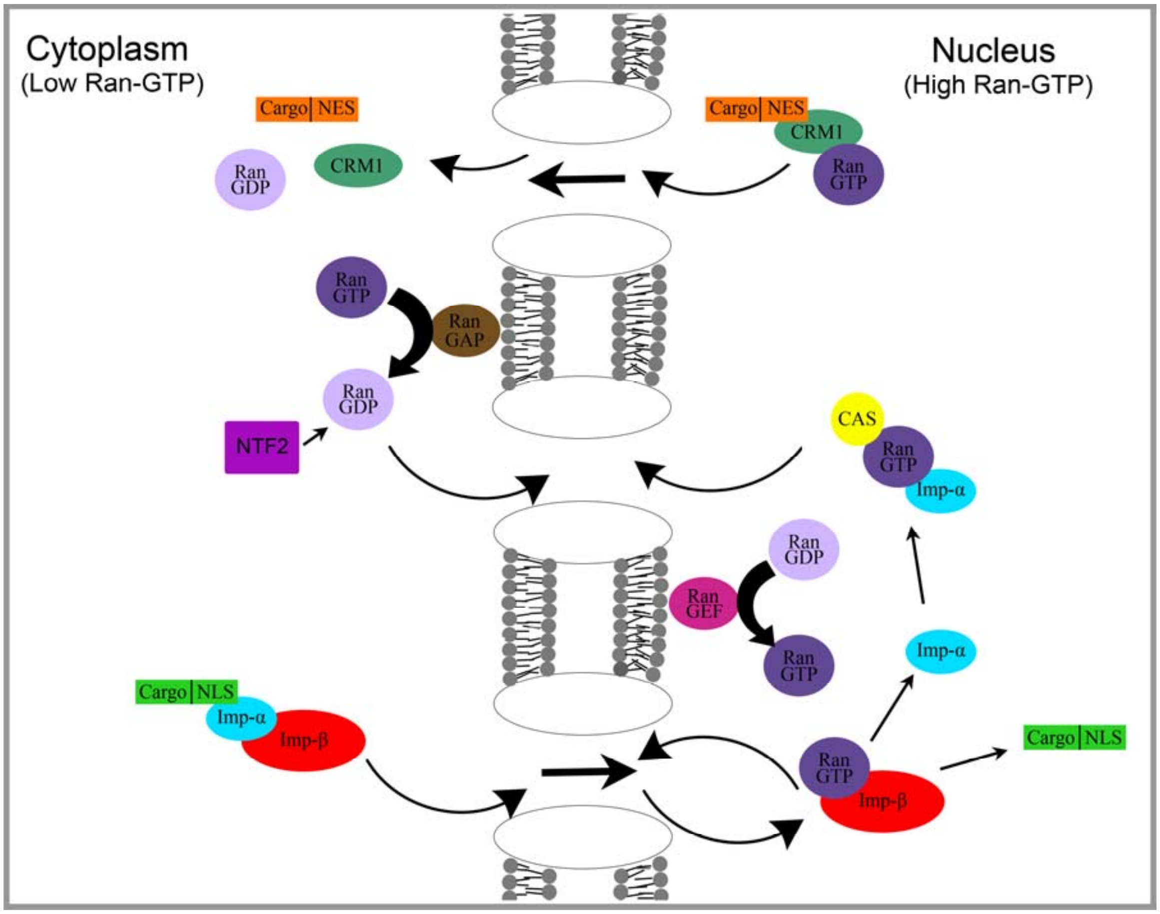

Figure 1.2 Schematic of the processes involved in signal mediated import and export through nuclear pore complexes. Nuclear import first requires the recognition of cargo containing a nuclear localization sequence (NLS) by the import chaperone importin α. This complex then interacts with a second import protein, importin β, allowing the heterotrimeric complex to be shuttled into the cell's nucleus. Release of the cargo is achieved as Ran-GTP binds importin β. The released importin α binds Ran-GTP through complexation with an exportin, CAS. The GTP bound forms of the karyopherins are recycled back into the cytoplasm. A similar cascade of events occurs for nuclear export in which cargo containing a nuclear export sequence (NES) specifically binds the exportin CRM1 and Ran-GTP. The directionality of transport is regulated by the Ran-GTP/Ran-GDP gradient as illustrated above.

shown as both mutation and immuno-blocking of the FG sites halts active transport through the pore.[43] The presence of the fibrils extending into the cytoplasmic and nuclear spaces is believed to enable the filaments to catch and retrieve molecules appropriately complexed with karyopherins in an initiation step for transport,[21] although later studies by Wente and co-workers showed that the deletion of Nups comprising both the cytoplasmic and nuclear filaments resulted in NPCs capable of both facilitated import and export. These findings have led to great debate as to the role of FG Nups in cyto-nuclear transport.[20]

The small dimensions of the pore and short transit times of cargo (~7 ms) have made the direct study of transport mechanisms quite challenging and though several mechanisms of transport have been hypothesized, they can basically be categorized into four slightly differing models; oily spaghetti,[44] virtual gating,[45] affinity gradient,[46, 47] and selective phase partitioning.[48] The common thread amongst all of these models is the direct involvement of the FG Nups in the selection and transport of cargo. Specifically, the oily spaghetti and virtual gating models hypothesize that the FG repeat domains within the pore can only be penetrated by molecules intended to be transported, while they are impenetrable to all other molecules. The slight difference between the two models is that the oily spaghetti model assumes a meshwork of non-interacting FG repeat domains while the virtual gating model describes a weak interaction between the hydrophobic FG repeats. The affinity gradient model attributes transport to an increasing affinity of the cargo for subsequent FG domains as the molecule moves through the pore, resulting in directed translocation across the membrane. Finally, the selective phase model describes a tight meshwork of highly interacting hydrophobic FG repeat domains which act like a size exclusion sieve, preventing the passage of large molecules through the pore. These interactions can be disrupted though by transport karyopherins, allowing the large cargo to pass through the enlarged meshes of the FG network. Recent studies have found evidence that suggests the selective phase model most accurately reflects the method of transport through NPCs, though studies continue.[49, 50]

The concentration of FG repeat domains in the pore has been calculated and suggested to form a hydrogel-like meshwork within the central channel.[51] The gel is believed to act like a molecular sieve with a mesh size of ~3 nm. Molecules too large to pass through the hydrophobic gel must then utilize the karyopherin chaperones to traverse the hydrogel-like sieve. The recruitment of importins and exportins exhibiting specific FG binding domains are believed to disrupt the hydrogel network, allowing the passage of complexes as large as ~50 nm in diameter or $\geq 10^6$ daltons.[50, 52, 53] In addition to the central pore, the presence of alternate diffusional channels within the periphery of the complex has also been suggested.[54, 55] These channels are believed to be free of FG repeats and to have a diameter of ~10 nm. The presence of these peripheral channels is supported by several studies that have blocked the central transport channel and found no effect on the transport of small, passively diffusing molecules across the NE. Furthermore, the 10 nm diameter of the peripheral channels is consistent with the ~9 nm size limit found for passive diffusion.[24]

While mechanisms describing the passive diffusion of molecules smaller than ~10kDa and the active transport of those larger than ~40kDa continue to evolve, for molecules with molecular weights between these cutoffs, the observations are much more varied.[56-61] Transport of these mid-sized molecules does not require the presence of the traditional components in active transport such as NLS or NES signals. However, their ability to transit the pore has been linked to other regulated systems such as intracellular calcium levels. In particular, several studies have specifically linked NPC permeability toward mid-sized molecules to cisternal calcium levels within the NE. Though some controversy exists, studies have shown that the diffusion of 10 kDa – 40 kDa cargo was diminished following release of cisternal calcium, suggesting a more complicated mechanism than simple diffusion through an open channel.[56, 57, 59]

Further investigations suggest that there may be a calcium dependence of both passive and active transport as well,[56, 57] although this work has been met with a series of studies suggesting that calcium levels play no role in regulating NPC transport.[58, 61] Clearly, these opposing conclusions require further work in order to elicit specific effects and mechanisms involving cisternal calcium. As depicted in Fig. 1.1, the NPCs reside in the double bilayer membrane of the nuclear envelope, the outer bilayer of which is contiguous with the endoplasmic reticulum (ER). The ER is a well known Ca^{2+} store for the cell, and the cisternal region located between the two bilayers of the NE, being contiguous with the ER, therefore also serves as an important calcium store. These cisternal calcium stores can be selectively released through signal-mediated pathways resulting in activation of membrane-bound inositol triphosphate (IP_3) and ryanodine (Ry) receptors.[59, 62, 63]

1.3 The Central Mass of the Nuclear Pore Complex

Interestingly, an insight into this Ca^{2+} dependent NPC permeability was found in the EM images of many of the pores themselves. The appearance of a central mass or plug was often found to be present in the central channel and its appearance was linked to sample preparation conditions including calcium concentrations within the NE.[10, 11, 64] The identity of this central mass has been highly debated as many groups have suggested that it represents an integral part of the NPC structure,[65, 66] that it is simply an artifact of sample preparation where the filamentous nuclear basket has collapsed and occluded the pore,[13, 67] or that is cargo caught transiting the NPC.[15, 64, 68] Given several studies, it seems most likely that the central mass most likely represents transiting cargo.[15, 69] Specifically, studies blocking transport through the use of methods such as exposure to low temperature and sequestration of ATP have been found to result in "plugged" NPCs similar to those seen upon cisternal calcium release, while warming of the samples and addition of an ATP regenerating system resulted in the disappearance of many of the plugs.[15] This suggests that the plugs located within the NPCs were a direct result of the hindered transport and that they represent cargo caught while transiting NPCs. The implication that the central mass represents transiting cargo was further supported by the ability to remove it from the pore by repetitively scanning a region of NPCs with atomic force microscopy (AFM) as it is assumed the minimal forces exerted would be unable to remove an integral component of the NPC, but could displace cargo.[69] Despite the unclear identity of the central mass, its link to NPC permeability initiated numerous studies in an effort to characterize its specific relationship with NPCs. Because of its high resolution and ability to image in biologically benign environments, AFM became a popular technique for these studies.

AFM is a scanning probe technique in which the sample surface topography is precisely mapped through its interaction with a sharp stylus protruding from a flexible AFM cantilever. Figure 1.3 illustrates how the tip tracks the sample surface as a feedback laser is reflected from the back of the cantilever to a quadrant photodiode detector. In constant force mode, interactions between the tip and the sample are monitored by the position of the reflected laser on the detector. Through an active feedback mechanism, the height of the AFM probe is precisely controlled, generating a high-resolution three-dimensional view of the sample surface. This technique has proven especially effective for monitoring NPC conformation including the presence and location of the central mass.[66, 70-72]

As with the transport studies, the characterization of NPC morphology as a function of calcium treatments was met with great controversy.[63, 67, 70-72] Initial AFM studies by Perez-Terzic and co-workers found that NPCs located in isolated *Xenopus laevis* oocyte nuclear envelopes became blocked by the central mass upon specific depletion of cisternal calcium through IP_3 mediated calcium channels.[66] Specifically, incubating the membranes in a 1 μM solution of inositol 1,4,5 triphosphate for 10

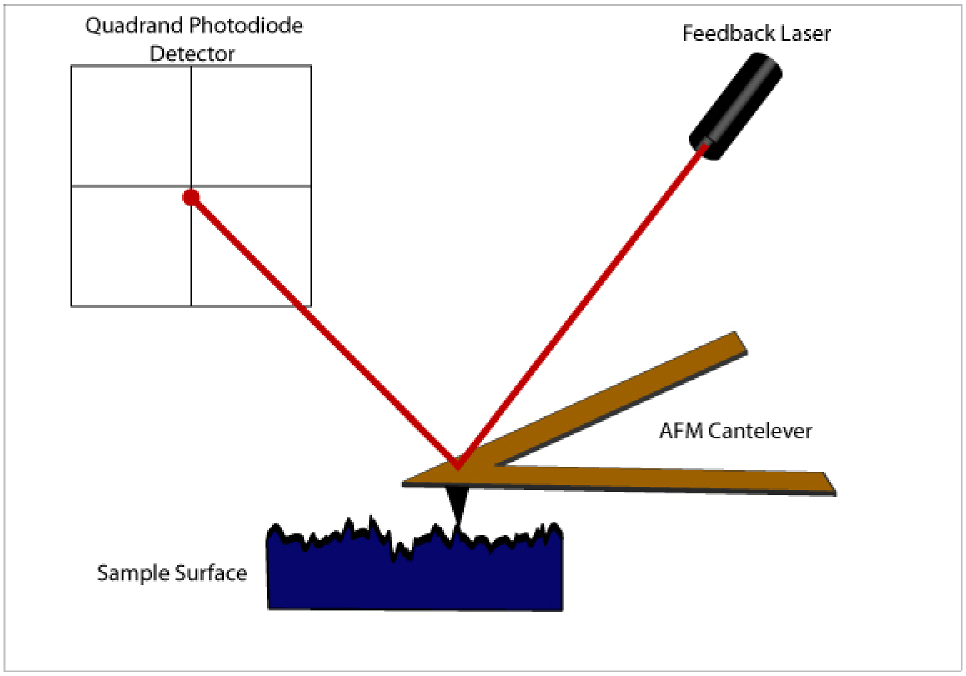

Figure 1.3 Basic illustration of the interaction between the probe and surface in atomic force microscopy (AFM). A feedback laser is reflected off from the back side of an AFM cantilever and onto a quadrant photodiode detector. In constant force mode the flexion of the probe resulting from interaction with the surface is recorded by the position of the laser on the detector. This allows for an active feedback system responsible for controlling the height of the cantilever and three-dimensional reconstructions of the sample surface.

minutes resulted in the appearance of a central plug within 91.9 ± 1.2% of NPCs measured, which is a drastic increase from the 6.9 ± 0.5% found to be plugged when the NEs were incubated in buffer containing a physiological free Ca^{2+} concentration (200 nM) prior to fixation. Furthermore, AFM linecuts through individual NPCs found that exposure to IP_3 also resulted in the apparent displacement of the central mass towards the nuclear rim of the NPC, as the measured pore depth decreased from 11.6 ± 0.8 nm to 2.1 ± 0.2 nm for NEs bathed in 200 nm Ca^{2+} and 1 μM IP_3, respectively. Control experiments in which NEs were bathed in 1 μM solutions of several alternate inositol phosphates which exhibit low affinities for IP_3 receptors found that NPCs exhibited no further plugging than when in physiological buffer. This suggests that the appearance and apparent displacement of the central mass was likely linked directly to release of cisternal calcium by the activation of IP_3 receptors within the NE, although questions as to the reliability of the measurements resulting from the chemical fixation, dehydration, and rehydration of the NEs arose.

In an effort to address these concerns, Stoffler and co-workers utilized AFM to observe the morphology of unfixed *Xenopus* NPCs as a function of external calcium conditions.[67] Their results found that the addition of significant amounts of free calcium (100 μM) into the surrounding buffer solution resulted in no affect on the appearance or position of the aforementioned central masses, but rather that it did affect the morphology of the nuclear basket. This was investigated by AFM in which unfixed, isolated *Xenopus* NEs were laid onto carbon coated TEM grids nuclear face up to expose the basket structures. Subsequent scans were taken of a field of NPCs as the buffer was changed from no free calcium to 100 μM calcium, to no calcium again through the addition of a calcium chelator, EGTA. Aligned and averaged profiles of 40 NPCs in each of the treatment conditions resulted in the apparent reversible closing and opening of the nuclear basket as calcium was added and chelated, respectively. Although the NEs remained unfixed and hydrated throughout the course of the experiments, the results are somewhat ambiguous as the addition and removal of exceedingly high concentrations of free calcium ions in the surrounding buffer does not represent a physiological stimulus within the system. Rather, calcium concentrations within the cell are controlled by the selective uptake and release of calcium from the cisternal space between the bilayers of the nuclear envelope and the endoplasmic reticulum.

In an effort to directly observe the effects of cisternal calcium levels on NPC conformation, previous members in our group undertook a series of studies utilizing AFM measurements of nuclear pores.[63, 70, 72] The first study investigated the cytoplasmic structure of *Xenopus laevis* oocyte nuclear pores as a function of cisternal calcium levels.[70] The selective release of calcium from the cisternal regions of the nuclear envelope and the ER was achieved through activation of inositol 1,4,5-trisphosphate receptors (IP_3Rs) with the potent and specific agonist Adenophostin A. It was found that as greater amounts of calcium were released through the increase in concentration of Adenophostin A treatments (0.08 nM – 250 nM), a dose-dependent displacement of the central mass towards the cytoplasmic face was observed as shown in Fig. 1.4. Specifically, Fig. 1.4A represents a field of NPCs treated with 80 pM Adenophostin A in which the small toroidal NPCs appear to be either devoid of the central mass completely or it is recessed deep within the pore. Fig. 1.4B is a similar field of nuclear pores in which the nucleus has been treated with 2 nM Adenophostin A and the presence of a protruding central mass is evident in nearly every pore. Figure 1.4C is a plot of NPC depth, measured from the top of the central mass to the level of the cytoplasmic ring, as a function of Adenophostin A treatments. The dose response curve revealed an EC_{50} of ~1.2 nM, which is consistent with that found previously for the activity of Adenophostin A.[73] Furthermore, careful observation of individual nuclear pores also correlated an increase in NPC diameter to Adenophostin A treatments where under low Adenophostin A conditions (high cisternal calcium) the mean pore diameter was ~75 nm while under high Adenophostin A conditions (low cisternal calcium), the mean diameter increased to ~90 nm. As a control, NPC morphology was monitored before and after the addition of Xestospongin C, a strong inhibitor of IP_3 receptors, simultaneously with the IP_3 agonist Adenophostin A. This resulted in no measureable change in NPC morphology, indicating that both the apparent displacement of the central mass and the change in NPC diameter were specifically linked to the release of cisternal calcium through the activation of IP_3Rs. In an effort to better understand the calcium dependent conformational changes observed in the previous study, further work was done to monitor the nuclear side conformational dependence of NPCs on calcium.[72] Monitoring of NPC morphology with AFM and selective release of cisternal calcium with Adenophostin A were carried out as before, but this time the nuclear envelopes

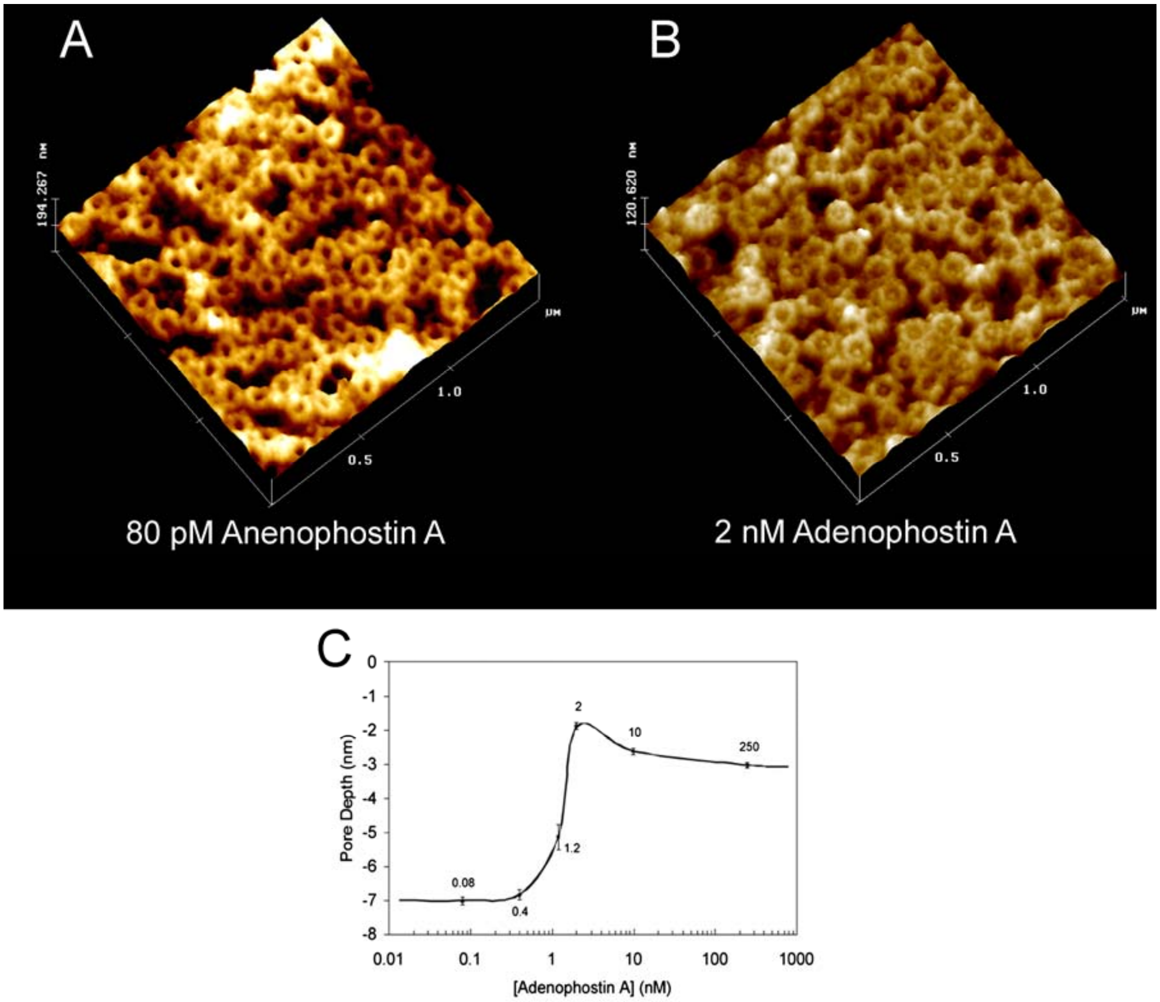

Figure 1.4 AFM images of NPCs in isolated nuclear envelopes illustrating the effects of cisternal calcium levels on NPC morphology. The many toroidal structures in the images represent nuclear pores under conditions of physiological cisternal calcium concentrations (A) and following the release of cisternal calcium via specific activation of IP_3Rs with a large dose of the potent agonist Adenophostin A. In Fig. 1.4A, the pores appear empty consistent with an open channel while release of cisternal calcium initiates the presence of a central mass or plug within the pores (B). The pore depth as a function of Adenophostin A treatment (C) reveals an EC_{50} of ~1.2 nm. This figure was modified with permission from reference 71.

were laid nuclear side up, exposing the NPC conformations on the nuclear face. Surprisingly, these measurements revealed a nearly identical dose response for the displacement of the central mass towards the nuclear face of the NPC, apparently suggesting that the central mass is simultaneously moving toward both the cytoplasmic and nuclear rings of the NPC rather than undergoing a unidirectional motion.

Taken together, this series of studies demonstrates a direct link between nuclear pore complex conformational changes and the specific alteration of cisternal calcium levels. The apparent displacement of the central mass towards both the nuclear and cytoplasmic faces and the evidence of a widening of the nuclear pores upon cisternal calcium release suggest a mechanism that is not as simple as the plug moving through the pore like a piston. Rather, we suggest a mechanism in which the NPC rings may collapse towards each other around the central mass. This significant structural change in the NPC would not only account for the apparent displacement of the central mass in both directions, but in the increase in NPC diameter as well as the necessary rearrangement of the nucleoporins would result in the broadening of the overall structure. Recent studies attempting to explain this strong dependence on cisternal calcium concentrations have led to the mapping of the location and structure of several individual nucleoporins with NPCs. Specifically, it has been found that one of the two trans-membrane Nups, gp210, exhibits numerous putative EF-hand calcium binding domains which extend into the cisternal region between the bilayers constituting the NE, possibly acting as a calcium ion sensor for the NPCs.[7, 56, 74]

Blocking this potential interaction by the specific binding of antibodies to gp210 significantly decreased cyto-nuclear transport of both signal mediated rhodamine-conjugated nucleoplasmin and non signal-mediated 10 kDa fluorescent dextran molecules. Although not conclusive, this study strongly suggests that gp210 plays a key role in sampling calcium levels within the NE and may act to regulate transport through the NPC conformational changes described above. Further studies of Ca^{2+} dependent morphologies and the proteins involved, including identification of the central mass, will lead to a better understanding of NPC transport regulation and the signaling pathways.

1.3.1 Identification of the Central Mass

Though there has been a significant amount of work done in an effort to understand the appearance, dynamics, and implications of the location of the central mass within NPCs, the identity of this enigmatic structure remains unclear. Many studies utilizing techniques such as EM and AFM have found the mass to be present under various conditions, although its location within the pore appears to be highly dependent upon cisternal calcium levels.[63, 70-72] As mentioned previously, studies correlating the specific arrest of transport to the appearance of plugs within NPCs strongly suggest that the central mass is cargo transiting the NPC. As numerous cellular components ranging from transcribed mRNA to enormous ribosomal subunits transit through NPCs, the identity of the central mass could include many cellular components. However, due to striking similarities in size and shape, its proposed transport functions, and expression of putative NLS and NES signals, vault ribonucleoproteins have been implicated as a particularly good candidate.[75-77]

Vault ribonucleoproteins are 13MDa hollow, barrel shaped structures comprised of repeats of three proteins and a variable number of untranslated RNA strands.[78-80] The very size, shape, and hollow nature of this ubiquitous protein have led to the speculation that it is involved in a shuttling or sequestering role.[80, 81] This idea is further supported by numerous studies in which MVP, the most abundant vault protein, has been found to be upregulated in multi drug resistant (MDR) cancer cell lines where they are believed to actively shuttle chemotherapeutic agents from the cell.[82, 83] Though MVP knockout models generally show no obvious phenotypic affects, one knockout mouse model was found to be significantly more prone to infection. This was attributed to the ability of vaults to directly uptake pathogens into exposed epithelial cells as a first effort in fighting infection.[84] These studies, in conjunction with many others implicating vaults in intracellular transport, support the idea that vaults are capable of crossing the NE via NPCs.[77, 85-87] The implications of identifying a cellular transport vessel that can be transported through NPCs leads to countless possibilities including gene therapy and directed drug delivery. Though a significant number of studies, including the ones discussed above, have provided valuable insights into NPC structure and conformation, it is clear that much work needs to be done in order to understand the details of the complete composition and function of the nuclear pore complex and its central mass.

1.4 Motivation and Overview of this Dissertation

As indicated in the previous sections, much work has been done in order to understand the structure and function of the nuclear pore complex. Through the use of imaging techniques such as EM and AFM, the NPC structure has been accurately mapped with high resolution and calcium dependent conformational changes have been explored, lending insight into its role in transport.[10, 11, 15, 25, 63, 66, 71, 72] Even with this knowledge, the details of transport through the nuclear pore complex remain largely unknown. By understanding the mechanisms and components involved in cyto-nuclear transport, advances in drug delivery, gene therapy, and a plethora of other fields could be realized.

Chapter 2 of this thesis will discuss a series of studies utilized to investigate the interaction of vault ribonucleoproteins with nuclear pore complexes. Specifically, studies involving Förster resonance energy transfer (FRET) found that there is a significant colocalization between vaults and NPCs in isolated *Xenopus laevis* oocyte nuclear envelopes. The use of high-resolution transmission electron microscopy (TEM) confirmed the colocalization as gold immuno-labeled vaults were found to coincide with NPCs in *X. laevis* nuclear envelopes. Finally, the dependence of the interaction on calcium was investigated as energy transfer efficiencies were calculated as a function of cisternal calcium levels. These measurements found a dependence strikingly similar to that reported in previous AFM measurements where the relative location of the central mass within NPCs was found to be strongly dependent on the cisternal calcium levels.[63, 70, 72]

The sensitivity of energy transfer to small changes in distance made FRET an ideal choice for the study of interaction between NPCs and vaults as it was able to discern nanometric changes in spatial relationship as a function of cisternal calcium levels. The small dimensions of nuclear pores and the limited resolution afforded by traditional optical techniques, however, mean that the FRET studies were limited to bulk average measurements of energy transfer and were unable to directly observe the interaction of vaults and individual NPCs. Though the use of TEM offers the necessary resolution, it requires that the sample undergo harsh preparatory steps and be imaged under extreme vacuum. Near-field scanning optical microscopy (NSOM) is a scanning probe technique which has been extensively used in solid state applications to obtain simultaneous high-resolution fluorescence and topographical data. The use of NSOM for investigating biological samples, such as the localization of vaults to NPCs, will allow for valuable high-resolution data not afforded by traditional optical techniques. Further advantages of NSOM result from the specificity of the fluorescent immunolabeling used and the simultaneous collection of topographical data. Chapter 3 addresses the advantages of NSOM as well as the modifications and difficulties associated with extending NSOM to biological samples.

One major concern in the extension of NSOM measurements to fragile biological samples surrounds heat transfer from the NSOM probe to the sample. Chapter 4 investigates the specific sample heating resulting from the use of nanometric NSOM probes. These studies used a polymer consisting of perylene and N-allyl-N-methylaniline (NA) which exhibits a “two-color” emission spectrum that changes with temperature.[88] The bulk emission spectrum consists of two peaks located at ~475 nm and ~510 nm. Upon heating, the ratio between the 475 nm and 510 nm peaks increases, providing a marker of sample heating that is not sensitive to light intensity or sample concentration. These studies alleviated concerns surrounding heating of sensitive biological samples such as nuclear membranes as temperatures were not found to exceed ~65°C. As a part of the study, light-induced probe failure was also investigated and found distinctly different mechanisms of failure for NSOM probes fabricated by heating and pulling and chemically etching. These findings provide previously unrealized insights into not only mechanisms of NSOM probe failure, but also possible methods for increasing NSOM probe efficiency and destruction thresholds.

Chapter 5 outlines a study in which NSOM was used to directly image interactions between vaults and NPCs on a pore by pore basis. Chapter 5 also discusses the advantages of NSOM for this particular study and the valuable insights afforded by the simultaneous collection of high-resolution optical data outlining vault distribution and topographical data defining the location of nuclear pores. The direct visualization of vaults and NPCs on *X. laevis* nuclear envelopes further indicated a significant correlation between vaults and NPCs, consistent with the previous FRET and EM studies.

While a number of investigations including the calcium dependent conformational studies of the nuclear pore complex and the works summarized in this dissertation provide great mechanistic insight into NPCs, they essentially provided snapshots in time of NPC conformation and interactions. As one of the main goals of the work was to identify transport mechanisms and cargo, dynamic studies of transport through NPCs were undertaken. Chapter 6 concerns a series of studies encompassing active and passive transport across the nuclear envelope. Nuclear transport events are exceptionally difficult to monitor as the large number of simultaneous events at neighboring NPCs and the short timescales on which these events occur make the measurements susceptible to ensemble averaging by bulk measurements. By developing a single-molecule transport assay utilizing the finite excitation field of total internal reflection fluorescence microscopy (TIRF-M) and a charged coupled device (CCD) with millisecond-scale time resolution, individual transport events were measured as a function of cargo size and various environmental factors. Dependences of transport times on such events lends further insight into the dynamics and mechanistic processes involved in cyto-nuclear transport.

Chapter 7 is reserved for the discussion of future work related the studies covered in the prior 6 chapters. As with all science, the work outlined in Chapters 1-6 may have provided many answers to important questions, but ultimately it leaves us wanting more. Possible future directions for the described studies will be outlined and their implications discussed.

1.5 References

(1) Cronshaw, J. M.; Krutchinsky, A. N.; Zhang, W.; Chait, B. T.; Matunis, M. J., Proteomic analysis of the mammalian nuclear pore complex. *J. Cell Biol.* **2002,** 158, (5), 915-27.

(2) Rout, M. P.; Aitchison, J. D.; Suprapto, A.; Hjertaas, K.; Zhao, Y.; Chait, B. T., The yeast nuclear pore complex: composition, architecture, and transport mechanism. *J. Cell Biol.* **2000,** 148, (4), 635-51.

(3) Reichelt, R.; Holzenburg, A.; Buhle, E. L., Jr.; Jarnik, M.; Engel, A.; Aebi, U., Correlation between structure and mass distribution of the nuclear pore complex and of distinct pore complex components. *J. Cell Biol.* **1990,** 110, (4), 883-94.

(4) Rout, M. P.; Wente, S. R., Pores for thought: nuclear pore complex proteins. *Trends Cell Biol.* **1994,** 4, (10), 357-65.

(5) Green, N. M., The nuclear pore--a biological grommet? *Nature* **1982,** 297, (5864), 287-8.

(6) Gerace, L.; Ottaviano, Y.; Kondor-Koch, C., Identification of a major polypeptide of the nuclear pore complex. *J. Cell Biol.* **1982,** 95, (3), 826-37.

(7) Greber, U. F.; Senior, A.; Gerace, L., A major glycoprotein of the nuclear pore complex is a membrane-spanning polypeptide with a large lumenal domain and a small cytoplasmic tail. *Embo. J.* **1990,** 9, (5), 1495-502.

(8) Hallberg, E.; Wozniak, R. W.; Blobel, G., An integral membrane protein of the pore membrane domain of the nuclear envelope contains a nucleoporin-like region. *J. Cell Biol.* **1993,** 122, (3), 513-21.

(9) Hsia, K. C.; Stavropoulos, P.; Blobel, G.; Hoelz, A., Architecture of a coat for the nuclear pore membrane. *Cell* **2007,** 131, (7), 1313-26.

(10) Akey, C. W., Interactions and structure of the nuclear pore complex revealed by cryo-electron microscopy. *J. Cell Biol.* **1989,** 109, (3), 955-70.

(11) Akey, C. W.; Radermacher, M., Architecture of the Xenopus nuclear pore complex revealed by three-dimensional cryo-electron microscopy. *J. Cell Biol.* **1993,** 122, (1), 1-19.

(12) Beck, M.; Lucic, V.; Forster, F.; Baumeister, W.; Medalia, O., Snapshots of nuclear pore complexes in action captured by cryo-electron tomography. *Nature* **2007,** 449, (7162), 611-5.

(13) Fahrenkrog, B.; Stoffler, D.; Aebi, U., Nuclear pore complex architecture and functional dynamics. *Curr. Top. Microbiol. Immunol.* **2001,** 259, 95-117.

(14) Pante, N.; Aebi, U., Toward the molecular details of the nuclear pore complex. *J. Struct. Biol.* **1994,** 113, (3), 179-89.

(15) Stoffler, D.; Feja, B.; Fahrenkrog, B.; Walz, J.; Typke, D.; Aebi, U., Cryo-electron tomography provides novel insights into nuclear pore architecture: implications for nucleocytoplasmic transport. *J. Mol. Biol.* **2003,** 328, (1), 119-30.

(16) Yang, Q.; Rout, M. P.; Akey, C. W., Three-dimensional architecture of the isolated yeast nuclear pore complex: functional and evolutionary implications. *Mol. Cell* **1998,** 1, (2), 223-34.

(17) Lim, R. Y.; Fahrenkrog, B., The nuclear pore complex up close. *Curr. Opin. Cell Biol.* **2006,** 18, (3), 342-7.

(18) Goldberg, M. W.; Allen, T. D., High resolution scanning electron microscopy of the nuclear envelope: demonstration of a new, regular, fibrous lattice attached to the baskets of the nucleoplasmic face of the nuclear pores. *J. Cell Biol.* **1992,** 119, (6), 1429-40.

(19) Dilworth, D. J.; Suprapto, A.; Padovan, J. C.; Chait, B. T.; Wozniak, R. W.; Rout, M. P.; Aitchison, J. D., Nup2p dynamically associates with the distal regions of the yeast nuclear pore complex. *J. Cell Biol.* **2001,** 153, (7), 1465-78.

(20) Strawn, L. A.; Shen, T.; Shulga, N.; Goldfarb, D. S.; Wente, S. R., Minimal nuclear pore complexes define FG repeat domains essential for transport. *Nat. Cell Biol.* **2004,** 6, (3), 197-206.

(21) Pante, N.; Aebi, U., Sequential binding of import ligands to distinct nucleopore regions during their nuclear import. *Science* **1996,** 273, (5282), 1729-32.

(22) Peters, R., Fluorescence microphotolysis to measure nucleocytoplasmic transport and intracellular mobility. *Biochim. Biophys. Acta.* **1986,** 864, (3-4), 305-59.

(23) Keminer, O.; Peters, R., Permeability of single nuclear pores. *Biophys. J.* **1999,** 77, (1), 217-28.

(24) Paine, P. L.; Moore, L. C.; Horowitz, S. B., Nuclear envelope permeability. *Nature* **1975,** 254, (5496), 109-14.

(25) Moore, M. S.; Blobel, G., The GTP-binding protein Ran/TC4 is required for protein import into the nucleus. *Nature* **1993,** 365, (6447), 661-3.

(26) Melchior, F.; Paschal, B.; Evans, J.; Gerace, L., Inhibition of nuclear protein import by nonhydrolyzable analogues of GTP and identification of the small GTPase Ran/TC4 as an essential transport factor. *J. Cell Biol.* **1993,** 123, (6 Pt 2), 1649-59.

(27) Dingwall, C.; Laskey, R., The nuclear membrane. *Science* **1992,** 258, (5084), 942-7.

(28) Wen, W.; Meinkoth, J. L.; Tsien, R. Y.; Taylor, S. S., Identification of a signal for rapid export of proteins from the nucleus. *Cell* **1995,** 82, (3), 463-73.

(29) Mosammaparast, N.; Pemberton, L. F., Karyopherins: from nuclear-transport mediators to nuclear-function regulators. *Trends Cell Biol.* **2004,** 14, (10), 547-56.

(30) Stewart, M., Molecular mechanism of the nuclear protein import cycle. *Nat. Rev. Mol. Cell Biol.* **2007,** 8, (3), 195-208.

(31) Tran, E. J.; Wente, S. R., Dynamic nuclear pore complexes: life on the edge. *Cell* **2006,** 125, (6), 1041-53.

(32) Gorlich, D.; Henklein, P.; Laskey, R. A.; Hartmann, E., A 41 amino acid motif in importin-alpha confers binding to importin-beta and hence transit into the nucleus. *Embo. J.* **1996,** 15, (8), 1810-7.

(33) Herold, A.; Truant, R.; Wiegand, H.; Cullen, B. R., Determination of the functional domain organization of the importin alpha nuclear import factor. *J. Cell Biol.* **1998,** 143, (2), 309-18.

(34) Gorlich, D.; Kostka, S.; Kraft, R.; Dingwall, C.; Laskey, R. A.; Hartmann, E.; Prehn, S., Two different subunits of importin cooperate to recognize nuclear localization signals and bind them to the nuclear envelope. *Curr. Biol.* **1995,** 5, (4), 383-92.

(35) Poon, I. K.; Jans, D. A., Regulation of nuclear transport: central role in development and transformation? *Traffic* **2005,** 6, (3), 173-86.

(36) Yang, W.; Musser, S. M., Visualizing single molecules interacting with nuclear pore complexes by narrow-field epifluorescence microscopy. *Methods* **2006,** 39, (4), 316-28.

(37) Fried, H.; Kutay, U., Nucleocytoplasmic transport: taking an inventory. *Cell Mol. Life Sci.* **2003,** 60, (8), 1659-88.

(38) Fischer, U.; Huber, J.; Boelens, W. C.; Mattaj, I. W.; Luhrmann, R., The HIV-1 Rev activation domain is a nuclear export signal that accesses an export pathway used by specific cellular RNAs. *Cell* **1995,** 82, (3), 475-83.

(39) Ossareh-Nazari, B.; Bachelerie, F.; Dargemont, C., Evidence for a role of CRM1 in signal-mediated nuclear protein export. *Science* **1997,** 278, (5335), 141-4.

(40) Fornerod, M.; Ohno, M., Exportin-mediated nuclear export of proteins and ribonucleoproteins. *Results Probl. Cell Differ.* **2002,** 35, 67-91.

(41) Kutay, U.; Guttinger, S., Leucine-rich nuclear-export signals: born to be weak. *Trends Cell Biol.* **2005,** 15, (3), 121-4.

(42) Bayliss, R.; Littlewood, T.; Strawn, L. A.; Wente, S. R.; Stewart, M., GLFG and FxFG nucleoporins bind to overlapping sites on importin-beta. *J. Biol. Chem.* **2002,** 277, (52), 50597-606.

(43) Powers, M. A.; Forbes, D. J.; Dahlberg, J. E.; Lund, E., The vertebrate GLFG nucleoporin, Nup98, is an essential component of multiple RNA export pathways. *J. Cell Biol.* **1997,** 136, (2), 241-50.

(44) Macara, I. G., Transport into and out of the nucleus. *Microbiol. Mol. Biol. Rev.* **2001,** 65, (4), 570-94, table of contents.

(45) Rout, M. P.; Aitchison, J. D.; Magnasco, M. O.; Chait, B. T., Virtual gating and nuclear transport: the hole picture. *Trends Cell Biol.* **2003,** 13, (12), 622-8.

(46) Ben-Efraim, I.; Gerace, L., Gradient of increasing affinity of importin beta for nucleoporins along the pathway of nuclear import. *J. Cell Biol.* **2001,** 152, (2), 411-7.

(47) Pyhtila, B.; Rexach, M., A gradient of affinity for the karyopherin Kap95p along the yeast nuclear pore complex. *J. Biol. Chem.* **2003,** 278, (43), 42699-709.

(48) Ribbeck, K.; Gorlich, D., Kinetic analysis of translocation through nuclear pore complexes. *Embo. J.* **2001,** 20, (6), 1320-30.

(49) Burke, B., Cell biology. Nuclear pore complex models gel. *Science* **2006,** 314, (5800), 766-7.

(50) Eguchi, A.; Furusawa, H.; Yamamoto, A.; Akuta, T.; Hasegawa, M.; Okahata, Y.; Nakanishi, M., Optimization of nuclear localization signal for nuclear transport of DNA-encapsulating particles. *J. Control. Release* **2005,** 104, (3), 507-19.

(51) Frey, S.; Richter, R. P.; Gorlich, D., FG-rich repeats of nuclear pore proteins form a three-dimensional meshwork with hydrogel-like properties. *Science* **2006,** 314, (5800), 815-7.

(52) Nakanishi, M.; Akuta, T.; Nagoshi, E.; Eguchi, A.; Mizuguchi, H.; Senda, T., Nuclear targeting of DNA. *Eur. J. Pharm. Sci.* **2001,** 13, (1), 17-24.

(53) Qu, Q.; Sawa, H.; Suzuki, T.; Semba, S.; Henmi, C.; Okada, Y.; Tsuda, M.; Tanaka, S.; Atwood, W. J.; Nagashima, K., Nuclear entry mechanism of the human polyomavirus JC virus-like particle: role of importins and the nuclear pore complex. *J. Biol. Chem.* **2004,** 279, (26), 27735-42.

(54) Hinshaw, J. E.; Carragher, B. O.; Milligan, R. A., Architecture and design of the nuclear pore complex. *Cell* **1992,** 69, (7), 1133-41.

(55) Ohba, T.; Schirmer, E. C.; Nishimoto, T.; Gerace, L., Energy- and temperature-dependent transport of integral proteins to the inner nuclear membrane via the nuclear pore. *J. Cell Biol.* **2004,** 167, (6), 1051-62.

(56) Greber, U. F.; Gerace, L., Depletion of calcium from the lumen of endoplasmic reticulum reversibly inhibits passive diffusion and signal-mediated transport into the nucleus. *J. Cell Biol.* **1995,** 128, (1-2), 5-14.

(57) Lee, M. A.; Dunn, R. C.; Clapham, D. E.; Stehno-Bittel, L., Calcium regulation of nuclear pore permeability. *Cell Calcium* **1998,** 23, (2-3), 91-101.

(58) Enss, K.; Danker, T.; Schlune, A.; Buchholz, I.; Oberleithner, H., Passive transport of macromolecules through Xenopus laevis nuclear envelope. *J. Membr. Biol.* **2003,** 196, (3), 147-55.

(59) Stehno-Bittel, L.; Luckhoff, A.; Clapham, D. E., Calcium release from the nucleus by InsP3 receptor channels. *Neuron* **1995,** 14, (1), 163-7.

(60) Stahelin, M.; Bopp, M. A.; Tarrach, G.; Meixner, A. J.; Zschokke-Granacher, I., Temperature profile of fiber tips used in scanning near-field optical microscopy. *Appl. Phys. Lett.* **1996,** 68, (19), 2603-2605.

(61) Wei, X.; Henke, V. G.; Strubing, C.; Brown, E. B.; Clapham, D. E., Real-time imaging of nuclear permeation by EGFP in single intact cells. *Biophys. J.* **2003,** 84, (2 Pt 1), 1317-27.

(62) Mak, D. O.; Foskett, J. K., Single-channel inositol 1,4,5-trisphosphate receptor currents revealed by patch clamp of isolated Xenopus oocyte nuclei. *J. Biol. Chem.* **1994,** 269, (47), 29375-8.

(63) Erickson, E. S.; Mooren, O. L.; Moore-Nichols, D.; Dunn, R. C., Activation of ryanodine receptors in the nuclear envelope alters the conformation of the nuclear pore complex. *Biophys. Chem.* **2004,** 112, (1), 1-7.

(64) Jarnik, M.; Aebi, U., Toward a more complete 3-D structure of the nuclear pore complex. *J. Struct Biol.* **1991,** 107, (3), 291-308.

(65) Akey, C. W., Visualization of transport-related configurations of the nuclear pore transporter. *Biophys. J.* **1990,** 58, (2), 341-55.

(66) Perez-Terzic, C.; Pyle, J.; Jaconi, M.; Stehno-Bittel, L.; Clapham, D. E., Conformational states of the nuclear pore complex induced by depletion of nuclear Ca2+ stores. *Science* **1996,** 273, (5283), 1875-7.

(67) Stoffler, D.; Goldie, K. N.; Feja, B.; Aebi, U., Calcium-mediated structural changes of native nuclear pore complexes monitored by time-lapse atomic force microscopy. *J. Mol. Biol.* **1999,** 287, (4), 741-52.

(68) Stephen, A. G.; Raval-Fernandes, S.; Huynh, T.; Torres, M.; Kickhoefer, V. A.; Rome, L. H., Assembly of vault-like particles in insect cells expressing only the major vault protein. *J. Biol. Chem.* **2001,** 276, (26), 23217-20.

(69) Danker, T.; Oberleithner, H., Nuclear pore function viewed with atomic force microscopy. *Pflugers Arch.* **2000,** 439, (6), 671-81.

(70) Moore-Nichols, D.; Arnott, A.; Dunn, R. C., Regulation of nuclear pore complex conformation by IP(3) receptor activation. *Biophys. J.* **2002,** 83, (3), 1421-8.

(71) Wang, H.; Clapham, D. E., Conformational changes of the in situ nuclear pore complex. *Biophys. J.* **1999,** 77, (1), 241-7.

(72) Mooren, O. L.; Erickson, E. S.; Moore-Nichols, D.; Dunn, R. C., Nuclear side conformational changes in the nuclear pore complex following calcium release from the nuclear membrane. *Phys. Biol.* **2004,** 1, 125-134.

(73) Adkins, C. E.; Wissing, F.; Potter, B. V.; Taylor, C. W., Rapid activation and partial inactivation of inositol trisphosphate receptors by adenophostin A. *Biochem. J.* **2000,** 352 Pt 3, 929-33.

(74) Greber, U. F.; Gerace, L., Nuclear protein import is inhibited by an antibody to a lumenal epitope of a nuclear pore complex glycoprotein. *J. Cell Biol.* **1992,** 116, (1), 15-30.

(75) Chugani, D. C.; Rome, L. H.; Kedersha, N. L., Evidence that vault ribonucleoprotein particles localize to the nuclear pore complex. *J. Cell. Sci.* **1993,** 106 (Pt 1), 23-9.

(76) Dickenson, N. E.; Moore, D.; Suprenant, K. A.; Dunn, R. C., Vault ribonucleoprotein particles and the central mass of the nuclear pore complex. *Photochem. Photobiol.* **2007,** 83, (3), 686-691.

(77) van Zon, A.; Mossink, M. H.; Houtsmuller, A. B.; Schoester, M.; Scheffer, G. L.; Scheper, R. J.; Sonneveld, P.; Wiemer, E. A., Vault mobility depends in part on microtubules and vaults can be recruited to the nuclear envelope. *Exp. Cell Res.* **2006,** 312, (3), 245-55.

(78) Kedersha, N. L.; Rome, L. H., Isolation and characterization of a novel ribonucleoprotein particle: large structures contain a single species of small RNA. *J.Cell Biol.* **1986,** 103, (3), 699-709.

(79) Kickhoefer, V. A.; Siva, A. C.; Kedersha, N. L.; Inman, E. M.; Ruland, C.; Streuli, M.; Rome, L. H., The 193-kD vault protein, VPARP, is a novel poly(ADP-ribose) polymerase. *J. Cell Biol.* **1999,** 146, (5), 917-28.

(80) Suprenant, K. A., Vault ribonucleoprotein particles: sarcophagi, gondolas, or safety deposit boxes? *Biochemistry* **2002,** 41, (49), 14447-54.

(81) Rome, L.; Kedersha, N.; Chugani, D., Unlocking vaults: organelles in search of a function. *Trends Cell Biol.* **1991,** 1, (2-3), 47-50.

(82) Bouhamyia, L.; Chantot-Bastaraud, S.; Zaidi, S.; Roynard, P.; Prengel, C.; Bernaudin, J. F.; Fleury-Feith, J., Immunolocalization and cell expression of lung resistance-related protein (LRP) in normal and tumoral human respiratory cells. *J. Histochem. Cytochem.* **2007,** 55, (8), 773-782.

(83) Dingemans, A. M. C.; vanArkOtte, J.; vanderValk, P.; Apolinario, R. M.; Scheper, R. J.; Postmus, P. E.; Giaccone, G., Expression of the human major vault protein LRP in human lung cancer samples and normal lung tissues. *Ann. Oncol.* **1996,** 7, (6), 625-630.

(84) Kowalski, M. P.; Dubouix-Bourandy, A.; Bajmoczi, M.; Golan, D. E.; Zaidi, T.; Coutinho-Sledge, Y. S.; Gygi, M. P.; Gygi, S. P.; Wiemer, E. A. C.; Pier, G. B., Host resistance to lung infection mediated by major vault protein in epithelial cells. *Science* **2007,** 317, (5834), 130-132.

(85) Stewart, P. L.; Makabi, M.; Lang, J.; Dickey-Sims, C.; Robertson, A. J.; Coffman, J. A.; Suprenant, K. A., Sea urchin vault structure, composition, and differential localization during development. *BMC Dev. Biol.* **2005,** 5, (1), 3.

(86) Slesina, M.; Inman, E. M.; Moore, A. E.; Goldhaber, J. I.; Rome, L. H.; Volknandt, W., Movement of vault particles visualized by GFP-tagged major vault protein. *Cell Tissue Res.* **2006,** 324, (3), 403-10.

(87) Eichenmuller, B.; Kedersha, N.; Solovyeva, E.; Everley, P.; Lang, J.; Himes, R. H.; Suprenant, K. A., Vaults bind directly to microtubules via their caps and not their barrels. *Cell Motil. Cytoskeleton* **2003,** 56, (4), 225-36.

(88) Chandrasekharan, N.; Kelly, L. A., A dual fluorescence temperature sensor based on perylene/exciplex interconversion. *J. Am. Chem. Soc.* **2001,** 123, (40), 9898-9.

Chapter 2

Localizing Vault Ribonucleoproteins to the Nuclear Pore Complex

2.1 Introduction

Discovered in 1986, vault particles are large ribonucleoproteins that have proven difficult to assign specific functional roles.[1] The 13 MDa complexes consist of multiple copies of three proteins and a variable number of untranslated RNA strands.[2-4] Approximately 75% of the total mass of the particle comes from 96 copies of a 100 kDa protein referred to as the major vault protein (MVP). The remaining mass comes from fewer copies of the 193 kDa vault poly (ADP ribose) polymerase, VPARP, and the 290 kDa telomerase-associated protein, TEP1.[1, 5, 6] The number of RNA molecules integrated into the structure is species-dependent and their biological significance remains unclear.[3, 7] While functionally little is known about vault particles, they are highly conserved across a wide variety of eukaryotic organisms ranging from certain fungi to humans,[8] suggesting they fulfill important cellular roles.

Vault particles are currently the largest known eukaryotic ribonucleoprotein and have been structurally characterized through high-resolution cryoelectron microscopy. These studies reveal a signature barrel-like structure, as depicted in Figure 2.1, with overall dimensions of 750Å x 420Å x 420Å.[9] The interior of vaults are hollow with a volume of 5 x 10^7Å^3, large enough to encapsulate two complete ribosomes.[5, 10] The barrel-like structure along with the large interior void has led to speculation that vaults may play a role in cellular transport.[5, 11-13] This has recently

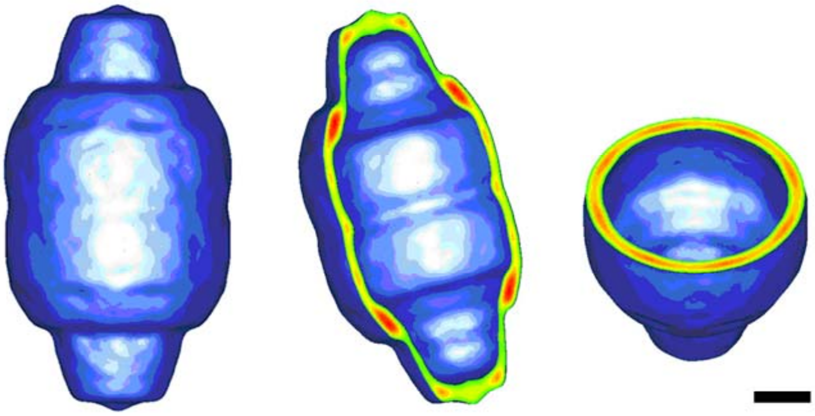

Figure 2.1 Three-dimensional transmission electron microscopy (TEM) reconstruction of sea urchin vaults with 33 Å resolution. The reconstruction shows the characteristic vault shape with an invaginated waist and a protruding cap on either end. The cropped views along the perpendicular and horizontal axis illustrate the symmetry and hollow nature seen in all vaults. The scale bar represents 10 nm. This figure was modified with permission from reference 37.

gained support from several studies.[14-16] For example, it has recently been shown that vaults can spontaneously assemble around specific cargo including luciferase and a GFP variant modified to express the 162-aa targeting sequence located at the C-terminus of the VPARP protein.[17] Furthermore, these cargo-containing vaults are successfully taken up by viable HeLa cells, providing a possible means for cellular inclusion of target molecules.[16] In another study, a GFP-MVP fusion protein was used to observe the distribution and movement of vault particles in living cells. Fluorescence recovery after photobleaching (FRAP) and video microscopy showed that individual vault particles are translocated through the cytoplasm at velocities of approximately 10μm/s, suggesting they are actively transported.[18]

Vault participation in cancer cell lines and multidrug resistance (MDR) has been under investigation since the discovery that the MVP subunit of vaults is found to be upregulated in many non-small cell lung cancer (NSCLC) cell lines.[19, 20] At the time of its discovery, the protein was identified and named lung resistance protein (LRP), but was later found to be identical to the previously described MVP.[21, 22] As primary lung cancers are currently the leading cause of deaths world-wide and NSCLC represents ~85% of this type of cancer, great effort has been made in understanding its particularly high resistance to chemotherapeutic treatment. MDR is a significant problem associated with the treatment of cancerous cell lines and its mechanism has been traced to a number of proteins such as P-glycoprotein (Pgp), multidrug resistance protein (MRP), and several members of the ATP binding cassette (ABC) superfamily which are all efflux pumps and actively remove drugs from the cell.[23, 24] Interestingly, a number of MDR cell lines have been shown not to overexpress these efflux proteins, but to instead have elevated levels of MVP, suggesting a role of vault proteins in MDR.[25] Although the direct mechanism by which vaults contribute to MDR is unclear, their large size and hollow nature, as well as their association to cytoskeletal elements such as tubulin and actin,[26-28] have fostered the belief that they may play a direct role in encapsulation and removal of therapeutic agents and/or other undesirable components from the cell.[29-31]

A recent series of experiments found that wild type respiratory epithelial cells infected by *P. aeruginosa* recruited significant amounts of MVP, as well as other vault components, to lipid rafts within the cell membrane.[32] The bacteria were then internalized by the cell as a first effort to confront the infection. Subsequent experiments determined that using small interfering RNA (SiRNA) reduced the cellular concentration of MVP by >90% and resulted in a reduction of the internalization of several strains of *P. aeruginosa* by 35-50%. The *in vivo* ramifications of this MVP reduction were explored by infecting wild type (WT) and MVP knockout ($MVP^{-/-}$) mice with *P. aeruginosa*. The lungs of the mice were examined and it was found that the $MVP^{-/-}$ mice internalized 55% less of the bacteria into their lung epithelial cells than WT, resulting in a 3.5-fold increase in the number of viable bacteria within the infected lungs themselves and a 3-fold increase in mortality in the MVP knockout mice.[32] This study indicates that vaults are likely not only involved in the cellular transport and removal of unwanted components, but also the selective internalization of infectious pathogens as an important first step in fighting infection.

The established links between intracellular transport and vaults have led to speculation that vaults and/or vault components are able traverse the nuclear envelope.[33] Expression of GFP-MVP molecules and immunofluorescence studies have largely identified vaults as cytoplasmic proteins,[18, 34] though discoveries of MVP associated with nuclear pores and within the nucleus suggests they, or at least their components, are capable of crossing the nuclear envelope and entering the nucleus.[15, 35, 36] During the embryonic development of sea urchin cells, for example, MVP distributes into the nucleus, suggesting an important nucleocytoplasmic transport role.[37] Furthermore, the isolation and sequence analysis of MVP has also identified the presence of both putative nuclear localization and nuclear export sequences necessary for the active transport of large molecules across the nuclear envelope.[37] Most recently, immunolabeled MVP has been found in the nucleus of mammalian U373 cells with the use of both immunofluorescent labeling and TEM, again suggesting that vaults actively cross the nuclear envelope.[15] As detailed in Chapter 1, the large nuclear pore complexes (NPCs) spanning the nuclear envelope represent the only direct route into and out of the nucleus, suggesting that vaults must utilize NPCs in order to access the nuclear compartment. This indirect evidence of interaction between vaults and pores, striking similarities in the morphology between vault particles and the central mass, and studies implicating vaults in transport have all led to the speculation that vaults may in fact not only interact with NPCs, but also represent the unidentified central mass often found to be present within the central channel of NPCs. Although there have been numerous studies suggesting that vaults may interact with NPCs and that they may be capable of crossing the nuclear envelope,[15, 33, 35, 36] direct evidence linking vaults and the central mass of nuclear pores has not previously been demonstrated.

Here, two antibodies raised against the major vault protein are characterized for use in a series of experiments to determine the relationship between vaults and NPCs. We first probe the relationship between vault proteins and NPCs using Förster resonance energy transfer (FRET) measurements between immunofluorescently labeled vaults and NPCs. Significant FRET interactions are observed which suggests that some population of vault particles reside in close proximity to NPCs in the nuclear envelope. Interestingly, the magnitude of the FRET interaction is dependent on the cisternal calcium levels. Since these levels also influence the location of the central mass within the pore, this provides an intriguing link between vaults and the yet to be identified central mass. Finally, electron microscopy (EM) measurements find significant colocalization between labeled vaults and NPCs. These results suggest that vault complexes closely interact with NPCs and may be involved in cyto-nuclear trafficking through the pore.

2.2 Förster Resonance Energy Transfer (FRET)

Förster resonance energy transfer (FRET) is a technique that takes advantage of the non-radiative transfer of energy from an excited donor fluorophore to a ground state acceptor molecule. The efficiency of this relies on several factors.[38, 39] An equation relating these factors can be written as:

$$R_O = [9.78x10^3 * K^2 * n^{-4} * QY_D * J(\lambda\,)]^{1/6}\ \text{Å} \qquad (2.1)$$

where R_O represents the distance between the fluorophores at which 50% energy transfer occurs. K^2 is a dipole orientation factor which describes the relative orientation of the emission dipole of the donor fluorophore and the absorption dipole of the acceptor fluorophore. Since K^2 is difficult to measure, it is often approximated to be 2/3 for a freely rotating FRET pair. QY_D is the fluorescence quantum yield of the donor in the absence of an acceptor, and $J(\lambda)$ represents the integral of the spectral overlap between the donor emission and the acceptor absorption. The energy transfer efficiency between the fluorophores can then be described as:

$$E = R_o^6/(R_o^6+r^6) \qquad (2.2)$$

Where again, R_o is the Förster distance constant for the particular dye pair in use (~1 nm – 10 nm) and r is the distance separating the donor and acceptor molecules. Upon excitation of the donor dye, energy transfer to the ground state acceptor results in its promotion to an excited electronic state. The excited acceptor is now able to return to ground state through a number of processes including fluorescence emission.

As described in Eq. 2.2, the energy transfer efficiency can be used to estimate the distance separating a FRET dye pair under various conditions. More importantly however, is that the energy transfer efficiency is dependent on this distance (r) to the inverse sixth power. Hence, small changes in r lead to measurable differences in

FRET efficiencies, making it a powerful tool for probing biological interactions and spatial changes in interactions on the nanometer scale.

Energy transfer efficiencies can be quantified a number of ways, but one of the most common is donor recovery post-acceptor photobleaching. Here, the fluorescence intensity of the donor fluorophore is quantified both before and after selectively photobleaching of a region of acceptor fluorophore. An increase in donor intensity in the region of the photobleached acceptor results, as the elimination of a non-radiative decay pathway leads to a higher probability of relaxation of the excited donor to ground state via the emission of a photon. This difference in donor fluorescence is quantified and normalized against the donor signal in the presence of active acceptor in order to precisely quantify the energy transfer efficiency between donor and acceptor dyes prior to photobleaching the acceptor.

By mapping the energy transfer efficiencies between donor and acceptor molecules as a function of varying conditions, this sensitive spectroscopic ruler allows for the monitoring of resulting changes not accessible by many other techniques. Because of the small dimensions of both NPCs and the central mass, as well as the small scale of relative changes in their relationship, FRET makes an ideal technique for studying the interaction between vaults and NPCs. It also provides a sensitive technique to quantify changes in interactions between NPCs and vaults as a function of conditions, such as cisternal calcium levels, which have previously been shown to have a significant impact on the apparent displacement of the plug within the pore.

2.3 Experimental

2.3.1 SDS-PAGE and Western Blot Analysis

All of the polyclonal antibodies explored for this study were prepared and provided by our collaborator, Kathy Suprenant.[40] Two antibodies raised against separate, highly conserved regions of the MVP were explored for use in this study. Briefly, the first antibody is isolated from rabbit serum and raised against the peptide sequence acetyl-DVQSVEPVDQRTRDALC-amide, which represents residues 649-664 of the MVP. The second antibody was also isolated from rabbit serum, but was raised against the peptide sequence acetyl-DQNSNVSRVEVGPKTYC-amide representing residues 29-45 in the MVP sequence. In order to ensure specific recognition of *Xenopus laevis* MVP by the antibodies, western blot analyses were performed.

Stage VI oocytes were harvested from mature *Xenopus laevis* (*Xenopus* express, Homosassa, FL) as detailed in the next section.[41] The oocytes were immediately placed in a freshly prepared, protease inhibitor containing, modified mock internal buffer consisting of 10 mM HEPES (Sigma Aldrich, St. Louis, MO), 1.4 mM $MgCl_2$, 140 mM KCl (Fisher Chemical, Fair Lawn, NJ), 10 μM Leupeptin, 10 μM Pepstatin A, and 100 μM Phenylmethanesulfonyl fluoride (PMSF) (Sigma-Aldrich, St. Louis, MO) and adjusted to pH 7.2 with $NaHCO_3$.

The cytoplasm from approximately one oocyte was transferred to a 0.5 mL eppendorf tube and centrifuged into a pellet. The supernatant was replaced with 15 μl of fresh lysis buffer containing 50 mM Tris-HCL, 1 mM EDTA, 1 mM β-mercaptoethanol (Sigma-Aldrich, St. Louis, MO), 1% triton X-100 (Sigma-Aldrich, St. Louis, MO), 0.1% sodium dodecyl sulfate (SDS), 10 μM Leupeptin, 10 μM Pepstatin A, and 100 μM PMSF. A purified rat vault protein sample was used as a positive control as the antibodies have previously been shown to recognize it.[40] The samples were diluted with a fresh protein dilution solution (PDS) containing 2% SDS, 100 mM dithiothreitol (DTT) (Bio-Rad, Hercules, CA), 60 mM Tris-HCl, 10% glycerol, 0.01% bromophenol blue (Sigma-Aldrich, St. Louis, MO), and 0.5% β-mercaptoethanol. The solution was adjusted to pH 6.8

All samples were placed in a 95˚C water bath for 5 minutes and 5 μL of each sample was loaded onto a 4% stacking, 7.5% resolving vertical polyacrylamide Tris-HCl gel (Bio-Rad, Hercules, CA). Lanes in the gel included cytoplasmic extract, purified rat vaults, and an unstained high molecular weight SDS-PAGE standard (Bio-Rad, Hercules, CA). The protein was transferred to an immune-blot polyvinylidene fluoride (PVDF) membrane (Bio-Rad, Hercules, CA), dried, and fixed with 7.5% acetic acid for 15 minutes on an orbital shaker. The membrane was stained with SYPRO Ruby (Molecular Probes, Carlsbad, CA) for 15 minutes and imaged on a Typhoon Trio imaging system. The membrane was then blocked for 1 hour in 5% dry skimmed milk, and floated on either a 1:3000 anti-DVQS:TTBS or anti-LDQN:TTBS solution for 2 hours, and further exposed for 1 hour in 1:3000 Alexa 633 goat anti-rabbit (Molecular Probes, Carlsbad, CA):TTBS solution. After drying, the membranes were imaged again on the Typhoon Trio imaging system in order to visualize antibody-binding specificity.

2.3.2 Isolation and Preparation of Xenopus laevis Nuclear Envelopes

Stage VI oocytes were harvested from mature *Xenopus laevis* (*Xenopus* express, Homosassa, FL) through a survival surgery where the *X. laevis* were anesthetized by exposure to 1g/L MS-222 (3-aminobenzoic acid ethyl ester) (Sigma Aldrich, St. Louis, MO). Once non-responsive, a 1 cm incision was made through the skin and underlying muscle layer of the *Xenopus* lateral to the central line of the abdomen. Several lobes of an ovary were removed through the incision and a single suture was used to close the incision. The oocytes were immediately placed in a freshly prepared, protease inhibitor containing modified mock internal buffer as described above. Nuclei were manually removed from the oocyte utilizing a dissecting microscope and fine-point forceps. The cytoplasmic debris was removed from the nuclei via repeated gentle pipetting through a glass Pasteur pipette. The dissection of the nuclei from the oocytes was accomplished on custom made Teflon-bottom dishes in an effort to prevent unwanted attachment of the nuclei. The cleaned nuclei were then transferred to separate Teflon-bottom dishes containing appropriate calcium altering conditions. Briefly, isolated and cleaned nuclei were incubated in the appropriate calcium altering buffers for 30 minutes. For the BAPTA-AM treated samples, the oocytes were incubated in a 10 μM solution of BAPTA-AM (Molecular Probes, Carlsbad, CA) in modified mock buffer for 1.5 hours prior to isolating the nuclei and exposing them to appropriate calcium altering buffers. The nuclei were chemically fixed in 5% paraformaldehyde dissolved in TBS for 20 minutes. The chemically fixed nuclei were then transferred to either copper 1000 mesh formvar coated TEM grids (Ted Pella, Redding, CA) or 25 mm x 25mm #1.5 coverglass (Fisher Scientific, Fair Lawn, NJ) where the nuclear envelopes were manually lysed with fire polished glass pipettes allowing for the removal of the nuclear contents. The nuclear envelopes were then laid flat, the surrounding solution was removed, and the nuclei were allowed to air dry. Once dry and adhered to the substrate, the nuclei were gently rinsed with ultrapure water (18 MΩ) and exposed to subsequent appropriate labeling steps for specific detection in TEM and energy transfer measurements.

2.3.3 Energy Transfer Measurements

For FRET measurements, *Xenopus* oocytes were harvested and the nuclei isolated as detailed in the previous section. The specific labeling of vaults was accomplished using the anti-DVQS and anti-LDQN antibodies while NPC Nups containing the conserved FxFG repeat sequence were labeled with the monoclonal antibody 414 (mab-414) (Covance, Princeton, NJ). The sample was then incubated in modified mock buffer containing the antibodies for 2 hours, rinsed, and incubated in the secondary antibody solutions for 1 hour. DVQS and LDQN labeled vaults were fluorescently labeled with Alexa 488 goat anti-rabbit IgG while mab-414 labeled FG repeats in the NPC were fluorescently labeled with Alexa 555 donkey anti-mouse IgG.

The FRET efficiencies were measured using the 488 nm and 568 nm excitation lines of a mixed gas Kr/Ar laser (Ion Laser Technology, Salt Lake City, UT) and a Bio-Rad MRC1000 scanning confocal fluorescence microscope (BioRad, Hercules, CA). Energy transfer efficiencies between the donor labeled vaults (Alexa 488) and acceptor labeled NPCs (Alexa 555) were quantified by measuring the difference in donor emission before and after acceptor photobleaching as previously described.[42] Normalizing these values with the post photobleaching donor level provides a measure of the relative increase in donor emission without interference from channel cross-talk. The donor enhancement corresponds directly with the energy transfer occurring prior to acceptor photobleaching as the donor fluorescence is no longer quenched by the presence of the acceptor molecule. For this dye pair, the R_0 distance at which energy transfer is 50% efficient is 7.0 nm.

2.3.4 Transmission Electron Microscopy Measurements

Nuclei were harvested and isolated as described above and negatively stained by exposure to 1% osmium tetroxide for one hour followed by floating the inverted grids on 2% uranyl acetate for ten minutes. The DVQS labeled vaults were exposed to 10 nm gold spheres conjugated to goat anti-rabbit antibodies (Molecular Probes, Carlsbad, CA) for an additional 2 hours. Transmission electron microscopy measurements were carried out using a JEOL 1200EX-II.

2.4 Results and Discussion

Chapter 1 introduced NPCs and the unidentified central mass often found within the pore channel. Previous studies have shown that the appearance and relative position of this central mass is specifically coupled to cisternal calcium stores within the nuclear envelope,[43-47] though the identity of the central mass remains unclear. Similarities in morphology to vault particles and their proposed transport functions provide the intriguing possibility that vaults are involved in cyto-nuclear transport through NPCs. To probe whether the central plug of NPCs are specifically vault complexes caught in transport, immunolabeling studies were carried out.

2.4.1 Verification of Vault Antibody Specificity in X. laevis

Anti-DVQS and anti-LDQN antibodies were raised against a highly conserved region of the MVP in order to recognize vaults from a wide variety of hosts.[40] The anti-MVP antibodies have previously been shown to recognize rat, human, and canine MVP,[40] but have not been tested for recognition of *Xenopus laevis* MVP. To confirm that these antibodies are also capable of recognizing MVP in *X. laevis*, western blot analyses against *Xenopus* oocyte extracts were performed. It is important to note that obtaining quality western blots of the proteins in whole *X. laevis* oocytes proved challenging due to the high lipid composition in the oocyte yolk which did not allow for proper separation of the proteins by SDS-PAGE. Centrifuging the oocyte extract solution and collecting the supernatant removed the majority of the lipids, while repeating the process twice more on the subsequent soluble samples yielded clean separation and the reduction of insoluble lipids.

Figure 2.2 shows the Western blot analysis using cytoplasmic extracts from *Xenopus laevis* oocytes. Figure 2.2 (lane *b*) represents the detection of MVP by the

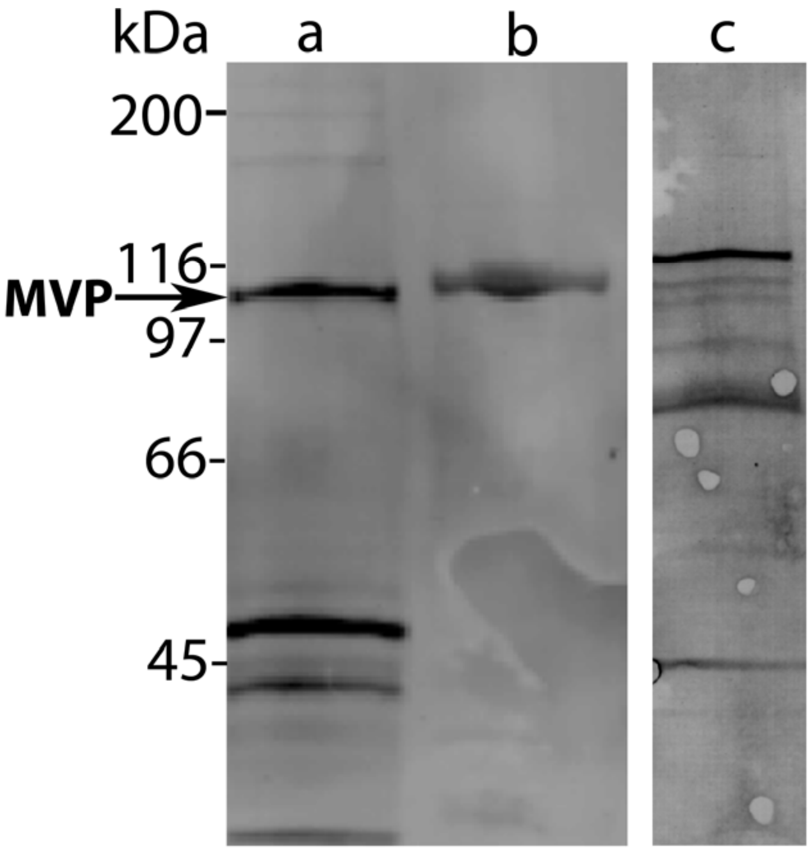

Figure 2.2 Western blot analysis showing specificity of the anti-DVQS and anti-LDQN antibodies toward *Xenopus laevis* MVP. Lane *b* represents the cytoplasmic extract from *Xenopus* oocytes probed with the anti-DVQS antibody, revealing a single band at ~100 kDa, the expected molecular weight of MVP. Lane *c* outlines the recognition of the anti-LDQN antibody for *Xenopus* vaults. The purified rat vaults in lane *a* act as a positive control and reveals the same band for MVP at 100 kDa. *The lighter bands in the control lane represent breakdown products of the MVP. * Lanes *a* and *b* were run on the same gel and probed by the anti-DVQS antibody, while lane *c* resulted from a separate gel and was reacted with the anti-LDQN antibody.

anti-DVQ5 antibody while Fig. 2.2 (lane *c*) is a similar western blot utilizing the anti-LDQN antibody against the major vault protein in *X. laevis* oocytes. A single band at ~100 kDa in the oocyte extract lane (lane *b*) aligns with the MVP protein band of the rat vault positive control (lane *a*) and is consistent with the known molecular weight of MVP from several species. A dark band in lane *c* located at approximately the same molecular weight indicated the recognition of MVP by the anti-LDQN antibody as well. The lower molecular weight proteins recognized by the anti-LDQN antibody most likely represent recognition of breakdown products of the MVP, although we cannot rule out non-specific interactions. These results confirm that the anti-DVQS and anti-LDQN antibodies recognize MVP from *Xenopus* although the anti-DVQS antibody appears to be more specific. As previous studies have shown that cellular MVP is associated with assembled vault complexes,[1, 48] the use of these antibodies, therefore, allows specific immunolabeling of vault particles in *Xenopus* oocytes.

2.4.2 Colocalization of Vaults with NPCs

The colocalization of vaults and NPCs was probed using high-resolution transmission electron microscopy (TEM). Using TEM, NPCs are visible in negatively stained nuclear membranes and vault particles were labeled with 10 nm gold spheres using the anti-DVQS antibody. Figure 2.3 shows representative results from the TEM studies. The NPCs appear as gray semi-circular features while the electron rich gold-labeled vaults appear as dark spots. Manual analysis of 506 labeled vaults from a series of TEM measurements finds that approximately 73% are

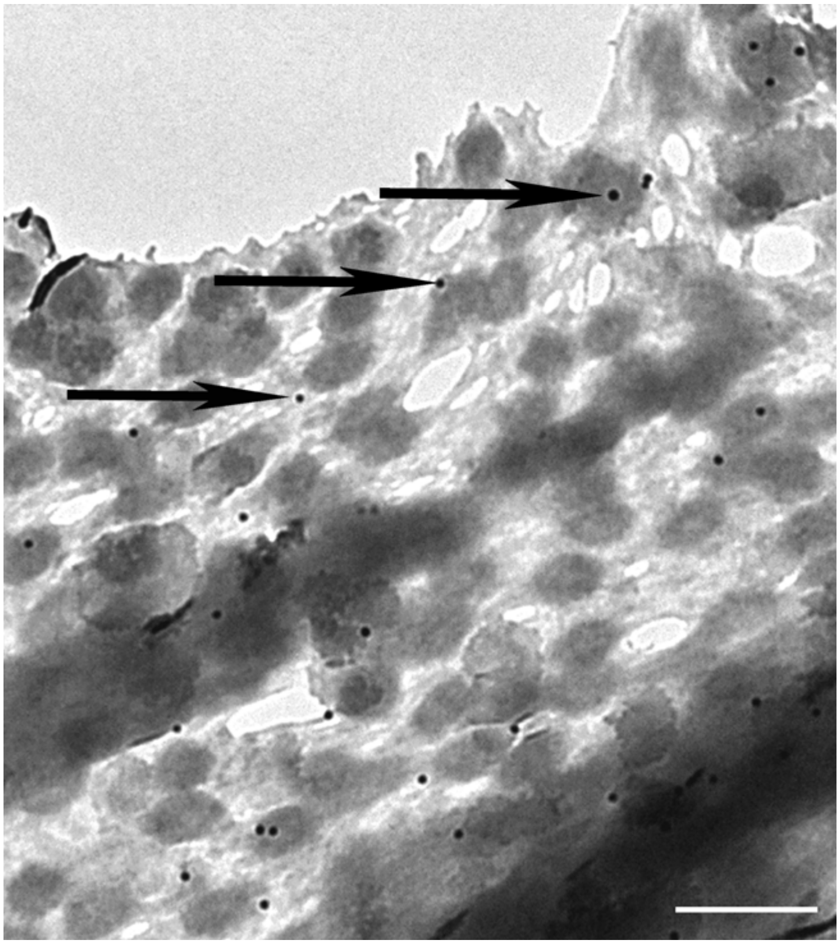

Figure 2.3 Representative TEM image of a negatively stained nuclear envelope in which vaults have been labeled with 10 nm gold spheres using the DVQS antibody. The labeled vaults appear as small dark spots while the NPCs are the larger, semi-circular gray features. The arrows indicate vaults that appear to reside in the pore region of a NPC (top arrow), on the periphery of a pore (middle arrow), and not associated with a pore (bottom arrow). Of the 506 MVP labels counted in the TEM images, approximately 373 or 73% were co-localized with NPCs. The scale bar is 200 nm.

associated with NPCs, while the remaining 27% were either not associated with a NPC or were questionably associated. In this case, a vault label was defined to be spatially associated with a nuclear pore if it was either found directly in the center of the pore indicating the possible inclusion of the vault into the central channel of the NPC or if it is peripherally associated in which case the vault may reside at the NPC in queue for subsequent transport. Analysis of the membranes indicated that nuclear pores account for approximately 50% of the surface area in the imaged membranes, thus a random distribution of labeled vaults would only be expected to lead to 50% colocalization. Controls in which membranes were treated with gold conjugated secondary antibodies only showed negligible non-specific labeling.

The TEM results suggest that vaults are localizing to NPCs, but in order to probe specific interactions on a nanometer scale, FRET measurements were conducted. FxFG Nups in the NPC were fluorescently labeled with mab-414-Alexa 555 and vaults were labeled with either anti-DVQS-Alexa 488 or anti-LDQN-Alexa 488. The Alexa 488/Alexa 555 dye pair has a R_o value of 7.0 nm. Figure 2.4 shows a representative series of fluorescence images taken on an isolated *X. laevis* nuclear envelope utilizing the anti-DVQS antibodies. The envelope has been flattened onto a coverslip for quantitative measurements. The dark regions represent the bare coverglass surrounding the membrane and the bright regions result from the specific binding of the fluorescently conjugated antibodies to the membrane. The top series of images show (A) the donor emission due to labeled vaults, (B) the acceptor emission from labeled NPCs, and (C) the FRET signal observed following donor excitation and monitoring of the acceptor emission. The strong FRET signal seen in Fig. 2.4C suggests there is a significant population of vaults closely associated with NPCs in the nuclear envelope. More specifically, equation 2.2 indicates that for an our dye pair with an R_o value of 7.0 nm and a measurable energy transfer efficiency, the vault and NPC labels must be located within ~10 nm of one another. The bottom series of fluorescence images in Fig. 2.4 shows the same area of the membrane following photobleaching of the NPC-bound acceptor dye. Photobleaching of the acceptor dye was accomplished by directly exciting the acceptor with high power (~20 mW) and repeatedly scanning within a small rectangular area. When photobleached, this results in a dark region in the acceptor channel fluorescence as shown in Fig. 2.4E.

Once the acceptor dye is photobleached, a corresponding dark region is also seen in the FRET image shown in Fig. 2.4F. With the acceptor dye now photobleached, fluorescence arising from energy transfer from excited donor to the acceptor is lost. Indicative of energy transfer interactions, however, a recovery in the vault labeled donor emission is seen in Fig. 2.4D. This is the direct result of the elimination of a non-radiative relaxation pathway, increasing the probability of donor relaxation through fluorescence. Because of this increased probability of radiative decay, the recovery in donor emission is proportional to the energy transfer efficiency prior to photobleaching. This enables determination of energy transfer efficiencies by quantifying the quenching of donor fluorescence in the presence of the FRET acceptor.[42]

Interestingly, though the vaults appeared to label brightly with the use of both

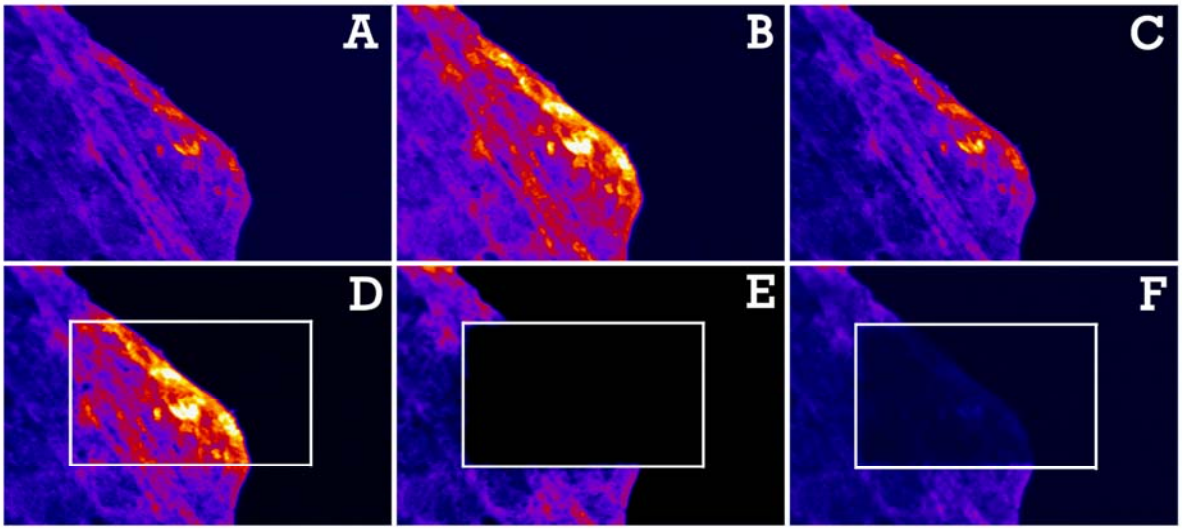

Figure 2.4 Förster resonance energy transfer (FRET) measurements of an isolated nuclear envelope. Vaults are fluorescently labeled with the donor dye Alexa 488 using the DVQS antibody and the NPCs are labeled with the acceptor dye Alexa 555 using the mab-414 antibody. (**A**) Emission from the donor dye shows the distribution of vaults while emission from the acceptor dye (**B**) reveals the NPC distribution. In (**C**), the FRET signal shows areas where donor labeled vaults and acceptor labeled NPCs are in close proximity. (**E**) To quantify the FRET efficiency, a region of the acceptor dye is photobleached. (**D**) Following photobleaching of the acceptor a large recovery in the donor emission is observed and the FRET signal (**F**) is strongly diminished. Analysis of these intensity levels is used to calculate the FRET efficiency.

antibodies, the FRET studies employing the anti-LDQN antibody as a vault label resulted in no significant energy transfer between donor and acceptor, suggesting that the dye pair is separated significantly further than their Förster distance. This difference likely arises as a result of the epitopes recognized by the individual antibodies. The anti-DVQS antibody was raised against a peptide sequence near the C-terminus of the MVP while the anti-LDQN antibody was raised against a sequence near the N-terminus of the MVP. A recent high-resolution model of the intact vault protein identifies the location of the MVP C-termini at the caps of the vault structure while the N-termini are located at the waist region.[49] Though both antibodies were found to recognize MVP and to effectively label the vaults within nuclear envelopes, the distance from the waist of a vault complex to the mAb 414 epitope on nuclear pores is likely too great for efficient energy transfer of a vault located within a pore. The location of the vault cap, on the other hand, places the fluorophores close enough for energy transfer to occur. Because of this, for the subsequent studies covered in this chapter, only the anti-DVQS antibody was utilized for the labeling of vault proteins

2.4.3 Calcium Dependent FRET Efficiencies

Having found significant colocalization of vaults to NPCs as confirmed by energy transfer efficiency measurements and direct observation with TEM, FRET efficiencies between labeled vaults and NPCs were then measured as a function of cisternal calcium levels. A calcium-dependent change in energy transfer efficiencies was expected as we have hypothesized that vaults comprise a population of the central mass within the NPC. Recall that specific manipulation of the cisternal calcium stores has been shown to lead to the collapse of the nuclear and cytoplasmic rings of the NPC towards each other, resulting in the apparent displacement of the central mass as observed with AFM.[43-47] The bar graph shown in Fig. 2.5 plots the FRET efficiencies measured as a function of treatments modifying the cisternal calcium levels. As seen in Fig. 2.5, significant increases in energy transfer are observed as the cisternal calcium levels are depleted through either the physiological stimulation of IP_3Rs or calcium chelation with BAPTA-AM. Specifically, FRET efficiencies of approximately 17% are measured for membranes incubated in buffer solutions containing between 200 nM and 200 μM Ca^{2+}. The highest FRET efficiencies were observed for membranes treated with the membrane permeable calcium chelator BAPTA-AM. This selective chelation of cisternal calcium through incubation in BAPTA-AM results in FRET efficiencies above 35%. Depletion of the cisternal calcium stores through the specific activation of IP_3 channels with Adenophostin A leads to a smaller increase in the FRET efficiency of 27%. Control measurements labeling with primary or secondary antibodies only led to no measurable energy transfer. These measurements show that the FRET efficiency between labeled vaults and NPCs are highly dependent on cisternal calcium levels, indicating that the interaction between vaults and NPCs is dependent on cisternal calcium concentrations.

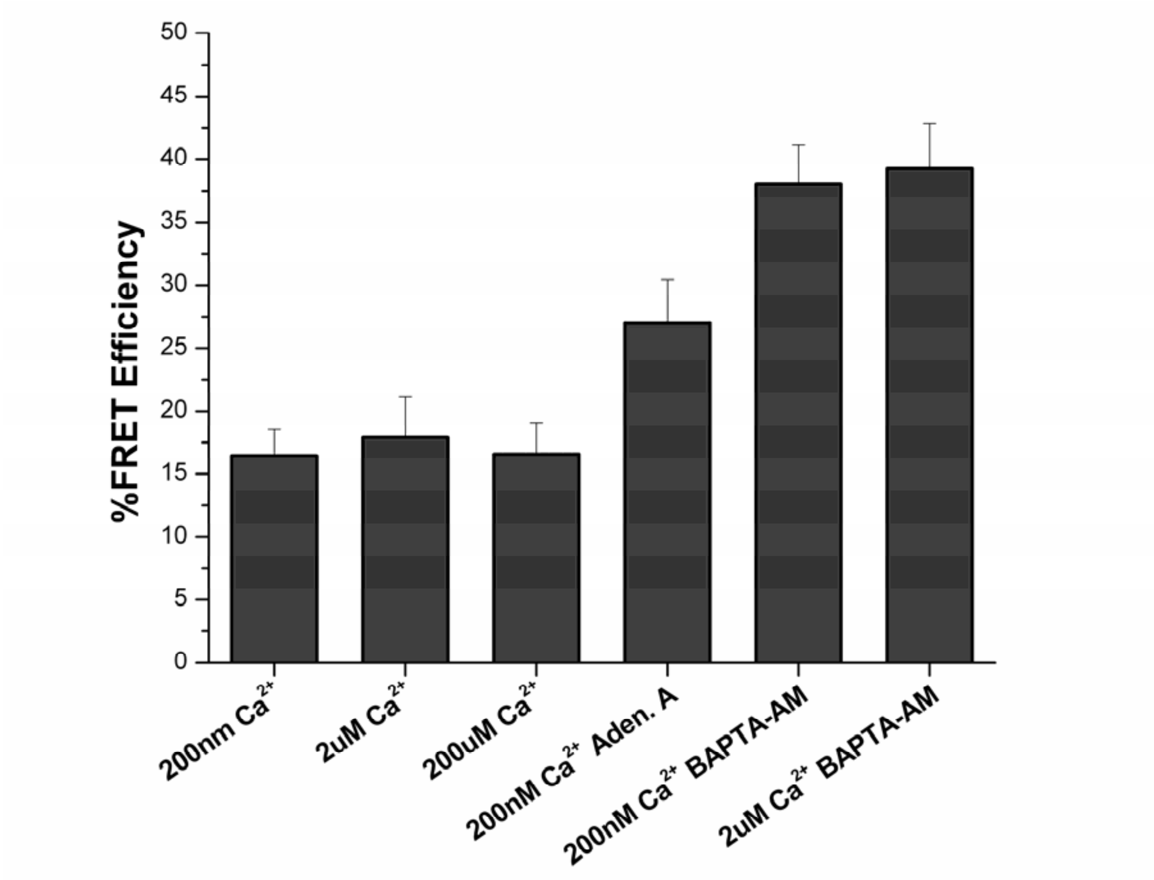

Figure 2.5 Average FRET efficiencies between fluorescently labeled vault and NPCs as a function of treatments to modify the cisternal calcium levels of the nuclear envelope. The average FRET efficiencies following manipulation of the cisternal Ca^{2+} are: 200 nM Ca^{2+}, FRET efficiency 16.5 +/- 2.1% (n=14); 2 μM Ca^{2+}, 17.9 +/- 3.2% (n=8); 200 μM Ca^{2+}, 16.7 +/- 2.5% (n=8); 200 nM Ca^{2+} + 10 nM adenophostin A, 27.0 +/- 3.4% (n=8); 200 nM Ca^{2+} + 10 μM BAPTA-AM, 38.1 +/- 3.1% (n=8); 2 μM Ca^{2+} + 10 μM BAPTA-AM, 39.3 +/- 2.3% (n=8).

2.4.4 Discussion

In Chapter 1, we described both the structure and functional roles of NPCs in depth and specifically discussed their conformation as a function of cisternal calcium levels. A systematic release of cisternal calcium resulted in a conformational change in NPCs in which the nuclear and cytoplasmic rings collapse towards one another, resulting in the apparent displacement of the central mass toward both the faces of the NPC.[43-47] The identity of the central mass, however, remains unclear.

Due to striking similarities in the size and shape of vault proteins to the central mass of NPCs, there have been suggestions in the literature that the NPC central mass may represent vaults transiting nuclear pores.[33, 35, 36, 50] Though the absolute functions of vaults remain unknown, they have been implicated in numerous transport processes such as multidrug resistance,[19, 20] toxic anion resistance,[29] and internalization of infectious pathogens as a first line of recognition and immunity.[32] This, along with their large, hollow structure, their inclusion of putative nuclear localization and nuclear export sequences,[37] and recent discoveries of MVP within the nuclei of cells strongly implicate them in cyto-nuclear trafficking and make them an intriguing candidate for the NPC central mass.[15]

Directly probing the interaction between vault particles and NPCs proves difficult due to the small scale over which these interactions occur. Recall that the calcium dependent conformational changes probed by AFM only found an ~6 nm difference in the location of the central mass to the rim of the NPC upon the depletion of calcium from the cisternal space.[44] Because of its sensitivity to nanometric changes in interactions and specific labeling of vaults and NPCs with immuno-techniques, Förster resonance energy transfer measurements were utilized to probe the relationship between vaults and NPCs in an effort to identify the central mass as vault proteins. The results from the FRET studies, such as those shown in Fig. 2.4, support this assignment and provide further insight into specific interactions occurring between vault particles and the NPC.

The strong FRET signals between anti-DVQS labeled vaults and NPCs shown in Fig. 2.4 suggest that vaults and NPCs are closely associated at the nuclear envelope. This is further supported by the TEM results shown in Fig. 2.3. The majority of the 506 vaults analyzed in the TEM images were associated with nuclear pores, either appearing directly in the center of the complex or associated with the rim. Over 70% of the vaults measured were spatially correlated with NPCs, supporting a model in which vaults interact or transport through the NPC. This is consistent with previous electron microscopy studies that have shown colocalization between vaults and NPCs in rat liver nuclei[51] and more recently in human astroglioma U373 cells.[15]

As described, both AFM and TEM measurements have found evidence that the location of the central mass in the NPC is directly linked with the nuclear envelope calcium stores. Specific stimulation of IP_3 receptors with Adenophostin A leads to a dose dependent conformational change in the NPCs resulting in the apparent displacement of the central mass towards both the cytoplasmic and nuclear compartments.[47, 52] As hypothesized, if some population of the central masses observed in NPCs represents vault particles caught in transport, FRET efficiencies between labeled vaults and NPCs should be affected by the calcium store levels. The FRET efficiencies plotted in Fig. 2.5 show that the specific spatial interaction between vaults and NPCs is in fact sensitive to cisternal calcium levels as is the central mass within NPCs, further suggesting a link between the central mass of NPCs and vaults.

As seen in Fig. 2.4, when nuclei are incubated in calcium containing buffers, a FRET efficiency between anti-DVQS labeled vaults and NPCs of approximately 17% is observed. However, as the cisternal calcium is removed through treatment with the membrane permeant chelator, BAPTA-AM, the FRET efficiency increases to approximately 40%. A similar trend is observed when the cisternal calcium stores are specifically released through stimulation of IP_3 receptors with Adenophostin A, although the magnitude of the effect is reduced.

Cisternal calcium removal through chelation or activation of IP_3 receptors have both previously been shown to lead to the apparent displacement of the central mass in the NPC.[45, 47, 52] Because of ambiguities regarding the precise location of the dyes on both the vault particle and the NPC, exact correlations with the AFM measurements are difficult. However, it is clear from these measurements that the proximity between vaults and NPCs is sensitive to specific manipulation of the cisternal calcium levels, as was shown for the central mass in previous AFM measurements.[43, 45, 47, 52]

2.5 Conclusions

Highly sensitive energy transfer measurements were utilized to determine that vaults and NPCs reside within nanometers of one another in isolated *X. laevis* nuclear membranes. High-resolution TEM measurements also confirm colocalization of vaults with nuclear pores. Measurements of energy transfer efficiencies between fluorescently labeled vaults and nuclear pores as a function of cisternal calcium levels show trends that agree with previous AFM studies of the relationship of the central mass within NPCs.

Together, the measurements reported here are consistent with the view that at least some population of the central masses observed in NPCs represent vault particles caught in transit. Recent studies have suggested that cargo as large as ~50 nm can pass through the NPC.[53-55] This suggests that vault particles are capable of being transported intact. However, since our measurements rely on the use of antibodies specific to the MVP component of the vault, we are unable to distinguish between intact vault particles or smaller sub-units in our measurements.

Though the cellular signals controlling the distribution of vaults remains unclear, previous studies have shown the inclusion of fluorescently labeled MVP within the nuclei of various cell lines, suggesting there are mechanisms for crossing the NPC.[15, 37] Studies, for example, have found evidence that the MVP can localize to the nuclei of human astroglioma U373 cells[15] and fluorescently labeled vaults migrate into the nuclei of developing sea urchin embryos.[37] The latter suggests that vault particles may act to transport species to the nucleus during development while the discovery of putative NLS and NES sequences within the primary structure of MVP provides yet another link to vaults and cyto-nuclear transport.[37]

Together with the FRET measurements shown here, these studies provide compelling evidence that the central mass represents vault particles transiting the NPC and that vaults are involved in cyto-nuclear trafficking. Elucidating the mechanism of transport and identifying the species being transported by vault particles should provide further insights into their role in cellular function.

2.6 References

(1) Kedersha, N. L.; Rome, L. H., Isolation and characterization of a novel ribonucleoprotein particle: large structures contain a single species of small RNA. *J Cell Biol* **1986,** 103, (3), 699-709.

(2) Kedersha, N. L.; Heuser, J. E.; Chugani, D. C.; Rome, L. H., Vaults. III. Vault ribonucleoprotein particles open into flower-like structures with octagonal symmetry. *J Cell Biol* **1991,** 112, (2), 225-35.

(3) Kickhoefer, V. A.; Searles, R. P.; Kedersha, N. L.; Garber, M. E.; Johnson, D. L.; Rome, L. H., Vault ribonucleoprotein particles from rat and bullfrog contain a related small RNA that is transcribed by RNA polymerase III. *J Biol Chem* **1993,** 268, (11), 7868-73.

(4) Kedersha, N. L.; Rome, L. H., Isolation and characterization of a novel ribonucleoprotein particle: large structures contain a single species of small RNA. *J.Cell Biol.* **1986,** 103, (3), 699-709.

(5) Suprenant, K. A., Vault ribonucleoprotein particles: sarcophagi, gondolas, or safety deposit boxes? *Biochemistry* **2002,** 41, (49), 14447-54.

(6) Kickhoefer, V. A.; Siva, A. C.; Kedersha, N. L.; Inman, E. M.; Ruland, C.; Streuli, M.; Rome, L. H., The 193-kD vault protein, VPARP, is a novel poly(ADP-ribose) polymerase. *J Cell Biol* **1999,** 146, (5), 917-28.

(7) van Zon, A.; Mossink, M. H.; Schoester, M.; Scheffer, G. L.; Scheper, R. J.; Sonneveld, P.; Wiemer, E. A., Multiple human vault RNAs. Expression and association with the vault complex. *J. Biol. Chem.* **2001,** 276, (40), 37715-21.

(8) Kedersha, N. L.; Miquel, M. C.; Bittner, D.; Rome, L. H., Vaults. II. Ribonucleoprotein structures are highly conserved among higher and lower eukaryotes. *J Cell Biol* **1990,** 110, (4), 895-901.

(9) Mikyas, Y.; Makabi, M.; Raval-Fernandes, S.; Harrington, L.; Kickhoefer, V. A.; Rome, L. H.; Stewart, P. L., Cryoelectron microscopy imaging of recombinant and tissue derived vaults: Localization of the MVP N termini and VPARP. *J. Mol. Biol.* **2004,** 344, (1), 91-105.

(10) Kong, L. B.; Siva, A. C.; Rome, L. H.; Stewart, P. L., Structure of the vault, a ubiquitous celular component. *Structure Fold Des.* **1999,** 7, (4), 371-9.

(11) Rome, L.; Kedersha, N.; Chugani, D., Unlocking vaults: organelles in search of a function. *Trends Cell Biol.* **1991,** 1, (2-3), 47-50.

(12) Hamill, D. R.; Suprenant, K. A., Characterization of the sea urchin major vault protein: a possible role for vault ribonucleoprotein particles in nucleocytoplasmic transport. *Dev Biol* **1997,** 190, (1), 117-28.

(13) Abbondanza, C.; Rossi, V.; Roscigno, A.; Gallo, L.; Belsito, A.; Piluso, G.; Medici, N.; Nigro, V.; Molinari, A. M.; Moncharmont, B.; Puca, G. A., Interaction of vault particles with estrogen receptor in the MCF-7 breast cancer cell. *J Cell Biol* **1998,** 141, (6), 1301-10.

(14) Stephen, A. G.; Raval-Fernandes, S.; Huynh, T.; Torres, M.; Kickhoefer, V. A.; Rome, L. H., Assembly of vault-like particles in insect cells expressing only the major vault protein. *J. Biol. Chem.* **2001,** 276, (26), 23217-20.

(15) Slesina, M.; Inman, E. M.; Rome, L. H.; Volknandt, W., Nuclear localization of the major vault protein in U373 cells. *Cell Tissue Res.* **2005,** 321, (1), 97-104.

(16) Kickhoefer, V. A.; Garcia, Y.; Mikyas, Y.; Johansson, E.; Zhou, J. C.; Raval-Fernandes, S.; Minoofar, P.; Zink, J. I.; Dunn, B.; Stewart, P. L.; Rome, L. H., Engineering of vault nanocapsules with enzymatic and fluorescent properties. *Proc Natl Acad Sci U S A* **2005,** 102, (12), 4348-52.

(17) Kickhoefer, V. A.; Garcia, Y.; Mikyas, Y.; Johansson, E.; Zhou, J. C.; Raval-Fernandes, S.; Minoofar, P.; Zink, J. I.; Dunn, B.; Stewart, P. L.; Rome, L. H., Engineering of vault nanocapsules with enzymatic and fluorescent properties. *Proc. Natl. Acad. Sci. U S A* **2005,** 102, (12), 4348-52.

(18) Slesina, M.; Inman, E. M.; Moore, A. E.; Goldhaber, J. I.; Rome, L. H.; Volknandt, W., Movement of vault particles visualized by GFP-tagged major vault protein. *Cell Tissue Res.* **2006,** 324, (3), 403-10.

(19) Dingemans, A. M. C.; vanArkOtte, J.; vanderValk, P.; Apolinario, R. M.; Scheper, R. J.; Postmus, P. E.; Giaccone, G., Expression of the human major vault protein LRP in human lung cancer samples and normal lung tissues. *Ann. Oncol.* **1996,** 7, (6), 625-630.

(20) Bouhamyia, L.; Chantot-Bastaraud, S.; Zaidi, S.; Roynard, P.; Prengel, C.; Bernaudin, J. F.; Fleury-Feith, J., Immunolocalization and cell expression of lung resistance-related protein (LRP) in normal and tumoral human respiratory cells. *J. Histochem. Cytochem.* **2007,** 55, (8), 773-782.

(21) Scheffer, G. L.; Wijngaard, P. L. J.; Flens, M. J.; Izquierdo, M. A.; Slovak, M. L.; Pinedo, H. M.; Meijer, C. J. L. M.; Clevers, H. C.; Scheper, R. J., The Drug Resistance-Related Protein Lrp Is the Human Major Vault Protein. *Nat. Med.* **1995,** 1, (6), 578-582.

(22) Scheper, R. J.; Broxterman, H. J.; Scheffer, G. L.; Kaaijk, P.; Dalton, W. S.; Vanheijningen, T. H. M.; Vankalken, C. K.; Slovak, M. L.; Devries, E. G. E.; Vandervalk, P.; Meijer, C. J. L. M.; Pinedo, H. M., Overexpression of a M(R) 110,000 Vesicular Protein in Non-P-Glycoprotein-Mediated Multidrug Resistance. *Cancer Res.* **1993,** 53, (7), 1475-1479.

(23) LechaptZalcman, E.; Hurbain, I.; Lacave, R.; Commo, F.; Urban, T.; Antoine, M.; Milleron, B.; Bernaudin, J. F., MDR1-Pgp 170 expression in human bronchus. *Eur. Respir. J.* **1997,** 10, (8), 1837-1843.

(24) Wioland, M. A.; Fleury-Feith, J.; Corlieu, P.; Commo, F.; Monceaux, G.; Lacau-St-Guily, J.; Bernaudin, J. F., CFTR, MDR1, and MRP1 immunolocalization in normal human nasal respiratory mucosa. *J. Histochem. Cytochem.* **2000,** 48, (9), 1215-1222.

(25) Kickhoefer, V. A.; Rajavel, K. S.; Scheffer, G. L.; Dalton, W. S.; Scheper, R. J.; Rome, L. H., Vaults are up-regulated in multidrug-resistant cancer cell lines. *J. Biol. Chem.* **1998,** 273, (15), 8971-4.

(26) Eichenmuller, B.; Kedersha, N.; Solovyeva, E.; Everley, P.; Lang, J.; Himes, R. H.; Suprenant, K. A., Vaults bind directly to microtubules via their caps and not their barrels. *Cell Motil. Cytoskeleton* **2003,** 56, (4), 225-36.

(27) Kedersha, N. L.; Rome, L. H., Vaults - Large Cytoplasmic Rnps That Associate with Cytoskeletal Elements. *Mol. Biol. Rep.* **1990,** 14, (2-3), 121-122.

(28) Herrmann, C.; Golkaramnay, E.; Inman, E.; Rome, L.; Volknandt, W., Recombinant major vault protein is targeted to neuritic tips of PC12 cells. *J. Cell Biol.* **1999,** 144, (6), 1163-72.

(29) Suprenant, K. A.; Bloom, N.; Fang, J. W.; Lushington, G., The major vault protein is related to the toxic anion resistance protein (TelA) family. *J. Exp. Biol.* **2007,** 210, (6), 946-955.

(30) Mossink, M. H.; van Zon, A.; Scheper, R. J.; Sonneveld, P.; Wiemer, E. A. C., Vaults: a ribonucleoprotein particle involved in drug resistance? *Oncogene* **2003,** 22, (47), 7458-7467.

(31) Kitazono, M.; Sumizawa, T.; Takebayashi, Y.; Chen, Z. S.; Furukawa, T.; Nagayama, S.; Tani, A.; Takao, S.; Aikou, T.; Akiyama, S., Multidrug resistance and the lung resistance-related protein in human colon carcinoma SW-620 cells. *J. Natl. Cancer I.* **1999,** 91, (19), 1647-1653.

(32) Kowalski, M. P.; Dubouix-Bourandy, A.; Bajmoczi, M.; Golan, D. E.; Zaidi, T.; Coutinho-Sledge, Y. S.; Gygi, M. P.; Gygi, S. P.; Wiemer, E. A. C.; Pier, G. B., Host resistance to lung infection mediated by major vault protein in epithelial cells. *Science* **2007,** 317, (5834), 130-132.

(33) van Zon, A.; Mossink, M. H.; Houtsmuller, A. B.; Schoester, M.; Scheffer, G. L.; Scheper, R. J.; Sonneveld, P.; Wiemer, E. A., Vault mobility depends in part on microtubules and vaults can be recruited to the nuclear envelope. *Exp. Cell Res.* **2006,** 312, (3), 245-55.

(34) Kickhoefer, V. A.; Vasu, S. K.; Rome, L. H., Vaults are the answer, what is the question? *Trends Cell Biol.* **1996,** 6, (5), 174-178.

(35) Chugani, D. C.; Rome, L. H.; Kedersha, N. L., Evidence that vault ribonucleoprotein particles localize to the nuclear pore complex. *J. Cell. Sci.* **1993,** 106 (Pt 1), 23-9.

(36) Dickenson, N. E.; Moore, D.; Suprenant, K. A.; Dunn, R. C., Vault ribonucleoprotein particles and the central mass of the nuclear pore complex. *Photochem. Photobiol.* **2007,** 83, (3), 686-691.

(37) Stewart, P. L.; Makabi, M.; Lang, J.; Dickey-Sims, C.; Robertson, A. J.; Coffman, J. A.; Suprenant, K. A., Sea urchin vault structure, composition, and differential localization during development. *BMC Dev. Biol.* **2005,** 5, (1), 3.

(38) Jares-Erijman, E. A.; Jovin, T. M., FRET imaging. *Nat. Biotechnol.* **2003,** 21, (11), 1387-1395.

(39) Selvin, P. R., The renaissance of fluorescence resonance energy transfer. *Nat. Struct. Biol.* **2000,** 7, (9), 730-734.

(40) Eichenmuller, B.; Kedersha, N.; Solovyeva, E.; Everley, P.; Lang, J.; Himes, R. H.; Suprenant, K. A., Vaults bind directly to microtubules via their caps and not their barrels. *Cell Motil Cytoskeleton* **2003,** 56, (4), 225-36.

(41) Marcussekura, C. J.; Hitchcock, M. J. M., Preparation of Oocytes for Microinjection of Rna and DNA. *Method. Enzymol.* **1987,** 152, 284-288.

(42) Kenworthy, A. K.; Petranova, N.; Edidin, M., High-resolution FRET microscopy of cholera toxin B-subunit and GPI-anchored proteins in cell plasma membranes. *Mol Biol Cell* **2000,** 11, (5), 1645-55.

(43) Erickson, E. S.; Mooren, O. L.; Moore-Nichols, D.; Dunn, R. C., Activation of ryanodine receptors in the nuclear envelope alters the conformation of the nuclear pore complex. *Biophys. Chem.* **2004,** 112, (1), 1-7.

(44) Moore-Nichols, D.; Arnott, A.; Dunn, R. C., Regulation of nuclear pore complex conformation by IP(3) receptor activation. *Biophys. J.* **2002,** 83, (3), 1421-8.

(45) Perez-Terzic, C.; Pyle, J.; Jaconi, M.; Stehno-Bittel, L.; Clapham, D. E., Conformational states of the nuclear pore complex induced by depletion of nuclear Ca2+ stores. *Science* **1996,** 273, (5283), 1875-7.

(46) Wang, H.; Clapham, D. E., Conformational changes of the in situ nuclear pore complex. *Biophys. J.* **1999,** 77, (1), 241-7.

(47) Mooren, O. L.; Erickson, E. S.; Moore-Nichols, D.; Dunn, R. C., Nuclear side conformational changes in the nuclear pore complex following calcium release from the nuclear membrane. *Phys. Biol.* **2004,** 1, 125-134.

(48) Kickhoefer, V. A.; Rajavel, K. S.; Scheffer, G. L.; Dalton, W. S.; Scheper, R. J.; Rome, L. H., Vaults are up-regulated in multidrug-resistant cancer cell lines. *J Biol Chem* **1998,** 273, (15), 8971-4.

(49) Anderson, D. H.; Kickhoefer, V. A.; Sievers, S. A.; Rome, L. H.; Eisenberg, D., Draft crystal structure of the vault shell at 9-A resolution. *PLoS Biol.* **2007,** 5, (11), e318.

(50) Kedersha, N. L.; Heuser, J. E.; Chugani, D. C.; Rome, L. H., Vaults. III. Vault ribonucleoprotein particles open into flower-like structures with octagonal symmetry. *J. Cell Biol.* **1991,** 112, (2), 225-35.

(51) Chugani, D. C.; Rome, L. H.; Kedersha, N. L., Evidence that vault ribonucleoprotein particles localize to the nuclear pore complex. *J Cell Sci* **1993,** 106 (Pt 1), 23-9.

(52) Moore-Nichols, D.; Arnott, A.; Dunn, R. C., Regulation of nuclear pore complex conformation by IP(3) receptor activation. *Biophys J* **2002,** 83, (3), 1421-8.

(53) Eguchi, A.; Furusawa, H.; Yamamoto, A.; Akuta, T.; Hasegawa, M.; Okahata, Y.; Nakanishi, M., Optimization of nuclear localization signal for nuclear transport of DNA-encapsulating particles. *J. Control. Release* **2005,** 104, (3), 507-19.

(54) Nakanishi, M.; Akuta, T.; Nagoshi, E.; Eguchi, A.; Mizuguchi, H.; Senda, T., Nuclear targeting of DNA. *Eur. J. Pharm. Sci.* **2001,** 13, (1), 17-24.

(55) Qu, Q.; Sawa, H.; Suzuki, T.; Semba, S.; Henmi, C.; Okada, Y.; Tsuda, M.; Tanaka, S.; Atwood, W. J.; Nagashima, K., Nuclear entry mechanism of the

human polyomavirus JC virus-like particle: role of importins and the nuclear pore complex. *J. Biol. Chem.* **2004,** 279, (26), 27735-42.

Chapter 3

Extending Near-Field Scanning Optical Microscopy to Biological Samples

3.1 Introduction

The ability to view and study biological structures directly on the spatial dimension that they exist has proven invaluable for understanding structure/function relationships. Historically, optical microscopy has proven particularly informative and throughout the years has steadily enhanced our understanding of tissue and finally cellular structure. Optical microscopy provides a relatively inexpensive, versatile platform for studying biological samples with a wide array of complementary contrast mechanisms. For example, optical techniques can provide high time resolution, polarization and spectroscopic capabilities, high specificity, and single-molecule fluorescence detection limits. Moreover, these can all be applied to living systems under biologically relevant conditions in a non-invasive manner.

One limitation of conventional optical microscopy, however, revolves around the maximal spatial resolution. When using lenses to focus light, the maximal spatial resolution is limited by the diffraction of light and is generally restricted to half the excitation wavelength. When working in the visible part of the spectrum, therefore, spatial resolution with aberration free optics is restricted to approximately 250 to 300 nm for conventional microscopy. Since many biologically interesting structures exist on smaller scales, other microscopy approaches have been developed.

Transmission electron microscopy (TEM) and scanning electron microscopy (SEM) have proven very powerful for understanding biological structures beyond the reach of optical techniques. These methods can resolve structures down to the nanometer scale and have been exploited to understand tissue architecture, membrane organization, and macromolecular structure to name a few. While these techniques offer vastly improved spatial resolution over optical microscopy, they do demand extensive sample preparation and require that the samples be in vacuum. These requirements can limit the applications and precludes the study of viable biological samples. With the development of scanning probe microscopy (SPM) techniques such as atomic force microscopy (AFM), however, nanometric spatial resolution on viable biological tissues is now routine.

As outlined in Chapter 1, AFM uses a small stylus to interrogate sample surfaces and can be implemented on unfixed biological samples under buffered conditions. These methods have nanometric spatial resolution, require very little sample preparation, and are, in general, minimally perturbative to the sample. However, since these measurements do rely mostly on topography, they lack the specificity inherent in immunofluorescence or studies utilizing fluorescent proteins.

Optical microscopy, electron microscopy, and to a lesser extent scanning probe microscopy have proven powerful tools for probing biological structure and function. Near-field scanning optical microscopy (NSOM) is a technique that can complement these more established methods. In general, the goal behind the development of NSOM was to create a technique that combined the favorable aspects of the more established microscopies mentioned earlier. NSOM is a light based microscopy that retains the specificity, spectral and polarization capabilities, and high time resolution inherent in optical microscopy. NSOM, however, circumvents the diffraction barrier that limits the spatial resolution in lens based optical microscopy and thus provides a spatial resolution nearing that of electron microscopy and scanning probe techniques.

This chapter will review the basic concepts of NSOM, focusing on aperture based methods. Following a brief overview of the technical aspects, several applications to biological samples will be discussed with a specific focus on work and experimental details from our lab. These examples will help illustrate the capabilities of NSOM and also highlight some of the difficulties involved in probing biological systems with NSOM as these difficulties have largely limited NSOM applications to fixed biological samples.

3.2 Principles of NSOM

In conventional light microscopy, where a lens is used to focus light, spatial resolution is limited by diffraction from the limiting aperture in the optical path, which is usually determined by the diameter of the focusing element. Light passing through the focusing element interferes around the focal point generating a diffraction pattern, the two-dimensional section of which in the focal plane leads to the well-known Airy disk pattern. The pattern was first described in detail by Ernst Abbe who defined the size of the Airy disk as the distance from the highest intensity point located within the disk to the first node of the pattern.[1] The size of the central spot in the Airy disk pattern, assuming collimated, coherent light is directed through an aberration-free microscope objective, is given by:

$$\text{spot size} = 0.77\ \lambda_{\text{vac}}/n \sin\theta \tag{3.1}$$

where λ_{vac} is the vacuum wavelength, n is the refractive index of the medium that the light travels through, and θ is the half angle through which the light is focused by the objective. The collection of terms in the denominator of Eq. (3.1) determines the minimal spot size and is collectively known as the numerical aperture (NA) of the objective.[2]

While spot size can be directly quantified, resolution is a more subjective quantity and is usually discussed in terms of the Rayleigh criterion which states that two features are resolvable if they are separated by a distance greater than or equal to that given by equation 3.1. With good signal-to-noise, finer separations can be resolved while imperfections in the optics, poor signal-to-noise, or sample limitations tend to reduce the resolving power. Given these tradeoffs, the resolving power using conventional optics is approximately equal to $\lambda/2$. When working in the visible region of the spectrum, therefore, spatial resolution is limited to approximately 250 nm - 300 nm.[3, 4]

In the early 1900s, Edward H. Synge published a series of papers in which he proposed a method to surpass the optical diffraction limit posed by the physical limitations of conventional optical lenses by removing the resolution-limiting optics all together.[5, 6] In order to increase resolution, Synge proposed introducing an aperture in an opaque screen, smaller than the wavelength of light used, be brought into very close proximity to the sample. By shining light through the aperture, this configuration would force the light to interact with the sample before it diffracted away, resulting in wavelength-independent resolution on the order of the diameter of the aperture. A schematic representing this approach is shown in Figure 3.1**.** Due to limitations in technology, however, Synge's idea would take nearly half a century to be implemented. Synge's principle was first demonstrated in 1972 by Ash and Nicholls using microwaves and by oscillating the sample below a small aperture in a thin diaphragm.[7] Accomplishing this same type of experiment utilizing light in the visible region would prove to be very difficult due to the need to fabricate apertures much smaller than those used in the aforementioned experiment. Building on Synge's proposal and with an improvement in methods enabling the fabrication of very small apertures, it was soon demonstrated that making a microscope with resolution of 50 nm was possible.[8] Subsequent studies[9-11] continued to improve on the design and illustrated the principles that enable NSOM to be performed today, while recent advances have made NSOM a more robust and feasible technique capable of examining a wide range of samples with resolution much greater than λ/2. However, applications in the biological sciences, where arguably NSOM could have the largest impact, have been slow and primarily limited to membranes and fixed cells.

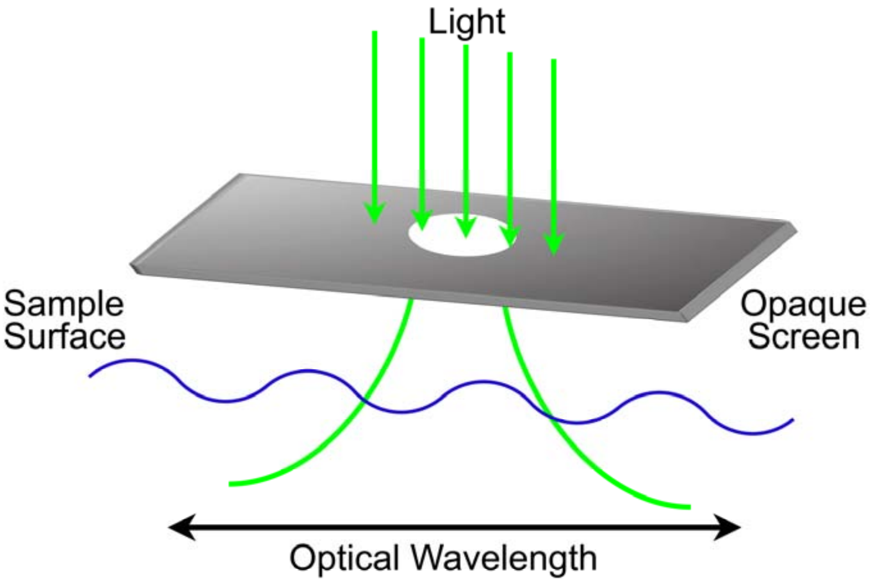

Figure 3.1 Schematic representation of light passing through the sub-wavelength diameter aperture of an opaque screen.

3.3 Biological Applications of NSOM

3.3.1 Membranes

NSOM is generally used for studying surfaces and has been widely employed for studying biological films and membranes.[12, 13] These studies have taken advantage of the simultaneously collected fluorescence and topography information of NSOM for characterizing the state of membrane systems. Small domains and structures in biological membranes have long been of interest and the high resolution of NSOM provides a tool with specific advantages that now allow membranes to be studied directly.

The complex composition and structure of biological membranes has led to the development of methods for studying model membranes under more controlled conditions. The use of Langmuir-Blodgett films allows for the creation of monolayer or multilayer films where temperature, composition and phase can be precisely controlled. Langmuir-Blodgett films have, therefore, been widely adopted to study lipid phases and component distribution in models of natural membranes.[14, 15]

The phase and component distribution in model membranes have been studied extensively with fluorescence microscopy. Many studies have shown that the inclusion of fluorescent lipid analogs, such as diIC_{18}, into the lipid films will preferentially partition into the less ordered regions of the film.[16-18] For lipid monolayers transferred onto substrates in the liquid expanded (LE)/liquid condensed (LC) phase coexistence region of the pressure isotherm, therefore, the condensed regions appear dark and the expanded regions appear bright in the fluorescence image. For example, Fig. 3.2A shows a fluorescence image of a DPPC lipid monolayer doped with 0.25 mol% of diIC$_{18}$, transferred onto a mica surface in the LE/LC phase coexistence region. In the image, semi-circular dark LC domains are surrounded by bright LE regions that contain the fluorescent lipid analog.[19]

The phase structure in lipid monolayers can be studied with higher spatial resolution using scanning probe techniques such as AFM in which the small 0.5 nm - 0.8 nm height differences between the LE and LC phases in DPPC can be measured to map the phase partitioning with nanometric spatial resolution. Figure 3.2B shows an AFM image of a DPPC monolayer transferred under the same conditions as that shown in Fig. 3.2A. Semi-circular domains of higher topography mark the LC regions of the film. Interestingly, the lower topography LE regions reveal a microstructure that was not resolved in the lower-resolution fluorescence image shown in Fig. 3.2A.

Utilizing NSOM on these samples offers the advantage of measuring both high-resolution fluorescence and topography simultaneously, which are particularly informative for studies of model membranes. Figure 3.2 also includes the NSOM fluorescence (3.2C) and topography (3.2D) images of a DPPC monolayer doped with 0.25 mol% diIC$_{18}$ and transferred under the same conditions as the films shown in Figs. 3.2A and 3.2B. The higher spatial resolution in the fluorescence image reveals the microstructures in the LE regions not observed with far-field fluorescence measurements. Furthermore, these nanometric structures can be directly correlated

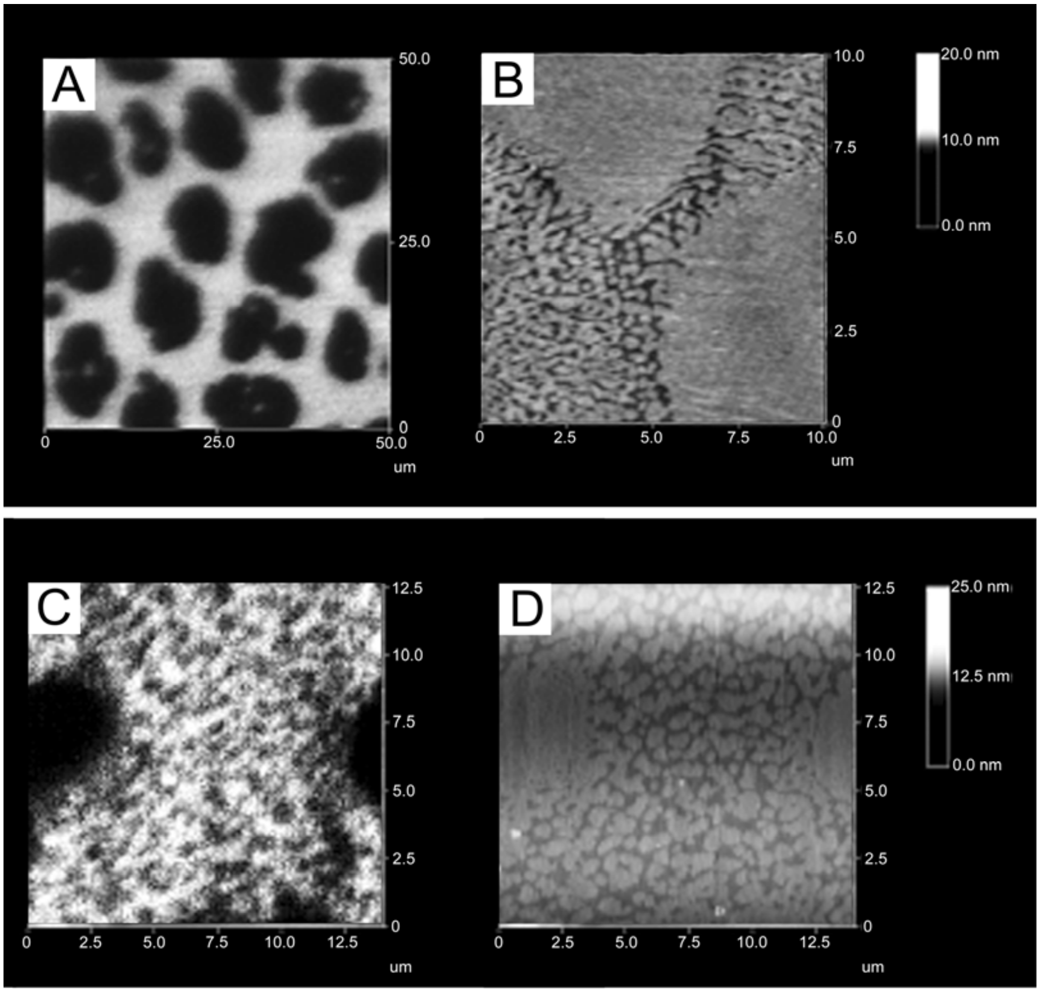

Figure 3.2 Confocal fluorescence (A) and AFM (B) images of a DPPC monolayer deposited at 9 mN/m onto cleaved mica using the Langmuir-Blodgett technique. At this surface pressure, the liquid condensed (LC) and liquid expanded (LE) phases of the monolayer coexist. (A) In the fluorescence image, bright regions incorporate a fluorescent lipid analog and mark the LE domains. The dark domains are the LC phase. In AFM measurements (B), the LC domains appear higher than the surrounding LE/LC microdomains. Note that the appearance of microdomains within the expanded region of the AFM image that are not resolved in the confocal image. (C) High-resolution NSOM fluorescence image of the same DPPC monolayer depicted in (A). The bright domains reveal the LE phase regions incorporating the dye while the dark areas represent LC domains. (D) NSOM topography image collected simultaneously with the fluorescence shown in (C). The small LE/LC domains observed in the AFM image are visible in both the NSOM fluorescence and topography measurements. This figure was modified with permission from reference 19.

with areas of lower topography seen in the NSOM topography image, confirming they arise from LE domains.[19]

In biological membranes, asymmetry is maintained across the bilayer and is critical for proper cellular function. Lipid and protein composition is different across the two leaflets of the plasma membrane of cells and loss of this asymmetry is a sign of apoptosis.[20] Probing this asymmetry directly is difficult since the membrane thickness is only ~6 nm. Förster resonance energy transfer (FRET), however, is a fluorescence technique that is sensitive to distances on this length scale and has been used extensively to probe membrane organization.[21, 22]

As discussed in Chapter 2, FRET takes advantage of energy transfer between a donor and acceptor dye that are in close proximity to each other. Non-radiative energy transfer between dyes with the proper spectral properties is very sensitive to changes in distance between the two dyes, making FRET a powerful tool for monitoring small displacements in biological systems.[23, 24] Several groups have combined the distance dependence of FRET with NSOM in order to create a new technique that has both high lateral and axial resolution, which should be capable of characterizing membrane asymmetry.[25-27]

The first application of this technique utilized a tapered fiber optic lacking the metal coating used in NSOM probes to confine the light within the tip. The end of the probe was instead coated using the LB technique with a DPPC monolayer doped with a rhodamine-labeled lipid.[27] The sample used in these studies consisted of a multilayer film comprised of a fluorescein-doped DPPC monolayer, three layers of arachidic acid that did not contain dye, and finally another layer of dye doped DPPC. A schematic of the experimental arrangement is shown in Fig. 3.3. For these studies, the fluorescein acted as the FRET donor dye and the rhodamine attached to the NSOM probe acted as the FRET acceptor.

Figure 3.3 shows the NSOM fluorescence images of the multilayer film following excitation of the donor at 458 nm. The two images shown represent the fluorescence from the donor (Fig. 3.3A) and acceptor (Fig. 3.3B). Comparing the two images illustrates the sectioning capabilities of combining FRET with NSOM. The features in the donor emission shown in Fig. 3.3A reveal the domains in both the top and bottom layers of the film that contain the donor dye, although it is not possible from this image to assign which layer the emission originated. The acceptor emission shown in Fig. 3.3B, however, arises from energy transfer from the excited donor in the sample to the tip-bound acceptor. As such, energy transfer efficiency from the top layer of the film is much higher than that from the bottom layer. In Fig. 3.3B, some domains appear much weaker indicating they reside in the bottom layer while other domains become brighter as they reside in the top layer, closer to the NSOM probe. The resolution of these domains also sharpens, as expected, since only dyes in closest approach contribute to the energy transfer signal, affording a lateral resolution of ~140 nm and z-sectioning capabilities of less than 8 nm. These studies not only serve to demonstrate the capabilities the NSOM/FRET technique, but also the adaptability of NSOM for use in a variety of configurations.

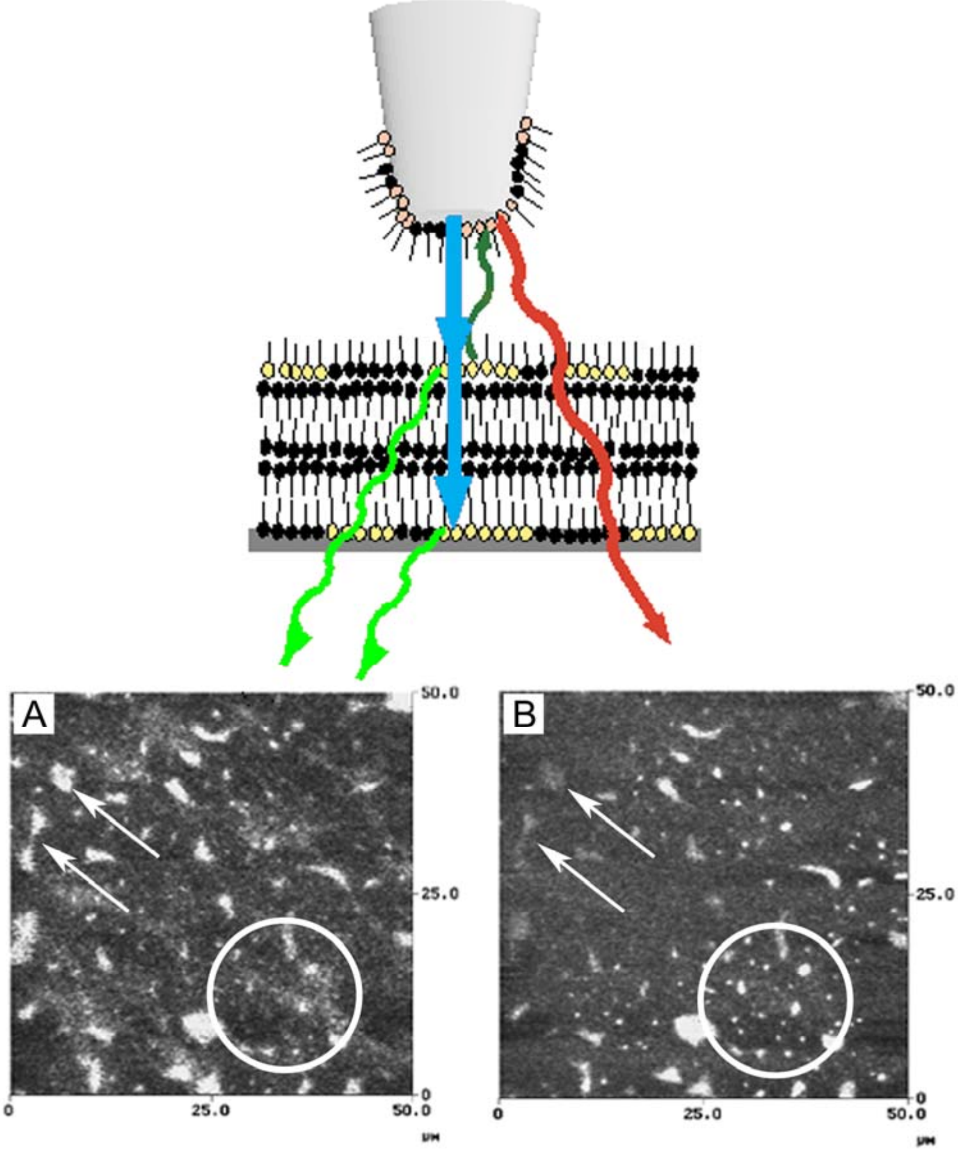

Figure 3.3 Schematic (top) of the experimental setup used in demonstrating the FRET/NSOM method. The fiber optic probe is coated with a monolayer containing a FRET acceptor fluorophore. The sampled consisted of a multilayer film where only the top and bottom layers contained the donor dye. **(A)** This image shows the fluorescence from the donor dye in the sample. **(B)** Acceptor emission that arises from energy transfer from the excited donor dye in the sample to the tip-bound acceptor. Comparison of the two images taken in the same area show that some features in the FRET/NSOM image lose intensity indicating they arise from domains in the bottom layer while others becoming brighter and more resolved indicating they are from the top layer. The figure was modified with permission from reference 27.

3.3.2 Cells

The demonstrated success of NSOM in imaging model membranes initiated an interest in its implementation on more complex biological systems although the extension to intact biological samples such as viable cells has proven challenging. Specifically, working with fragile samples under buffered conditions presents several challenges for NSOM which have been very difficult to overcome. Fixed biological tissues, however, are amenable with NSOM measurements both dry and under buffered conditions, opening vast new areas of research. For studies of fixed cells, the simultaneous collection of both high-resolution fluorescence and force information have proven particularly useful and informative.

3.3.2a Advantages of NSOM for use on Cellular Samples

The simultaneous collection of high-resolution force and fluorescence data offered by NSOM has opened many doors in the study of tissue and cellular samples as the distribution/interaction of biological components is often beyond the resolution of traditional optical techniques. Specifically, as NSOM has proven useful for the study of model membranes, it is also particularly well suited for the study of molecules and structures located at or near the plasma membrane of cells. Figure 3.4 shows the NSOM topography (A) and fluorescence (B) images of a fixed human arterial smooth muscle (HASM) cell in which the F-actin has been fluorescently labeled with phalloidin conjugated to the fluorescent Alexa Fluor 568 dye. A strong correlation is observed between the F-actin fibers identified in both the fluorescence

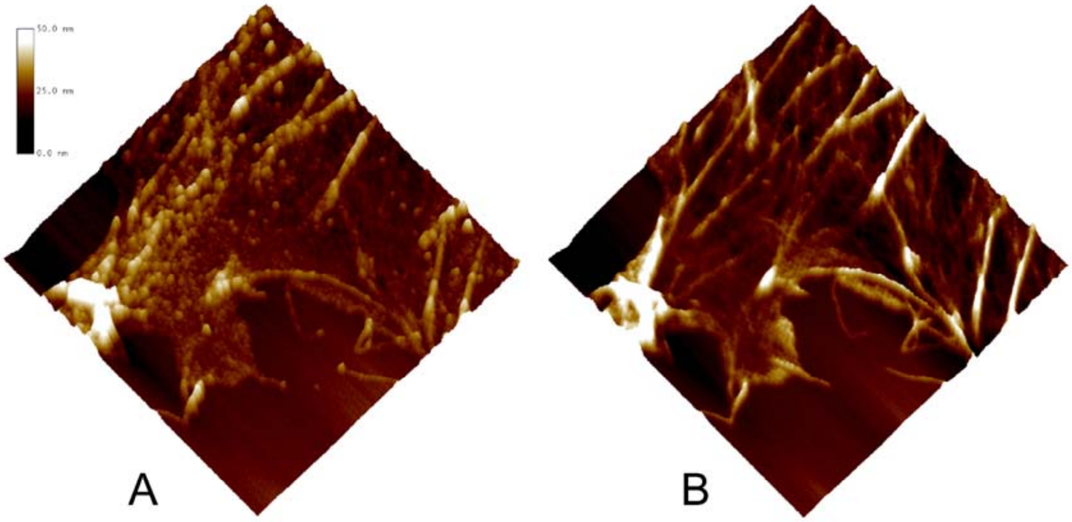

Figure 3.4 20 μm x 20 μm NSOM fluorescence (A) and topography (B) images of a human arterial smooth muscle (HASM) cell in which the F-actin has been labeled with a fluorescent phalloidin conjugate.

and force channels. The smallest fibers observed in the fluorescence channel have a FWHM of ~100 nm, representing a significant increase in resolution over traditional optical techniques. In addition, many of the fibers observed in the fluorescence image are not resolvable in the force channel and thus would not be seen with techniques such as AFM, illustrating the capabilities of NSOM for the imaging of molecules and interactions at or near cell membranes.

Another inherent advantage of NSOM for use on cellular samples involves autofluorescence within a sample. Autofluorescence is defined as the fluorescence of molecules other than the fluorophore of interest. Cells exhibit an especially significant degree of autofluorescence as they contain many natural chromophores including aromatic amino acids and co-enzymes such NADH and members of the flavin family. The intensity of cellular autofluorescence is known to be highly wavelength dependent, becoming less significant at increasing wavelengths.[28] This is illustrated in Fig. 3.5, which shows a sequence of images (Figs. 3.5A-F) depicting the autofluorescence from a human arterial smooth muscle (HASM) cell as a function of excitation wavelength. The cell has been chemically fixed with a 10 minute exposure to 4% paraformaldehyde in phosphate buffered saline (PBS) prior to rinsing and imaging. The power of each excitation laser line was maintained at 5 mW, as measured exiting the objective, in order to ensure consistent excitation intensities. The fluorescence was then collected through appropriate emission filters and captured onto a cooled CCD camera. Controls ensured that the results were not biased due to photobleaching during previous captures.

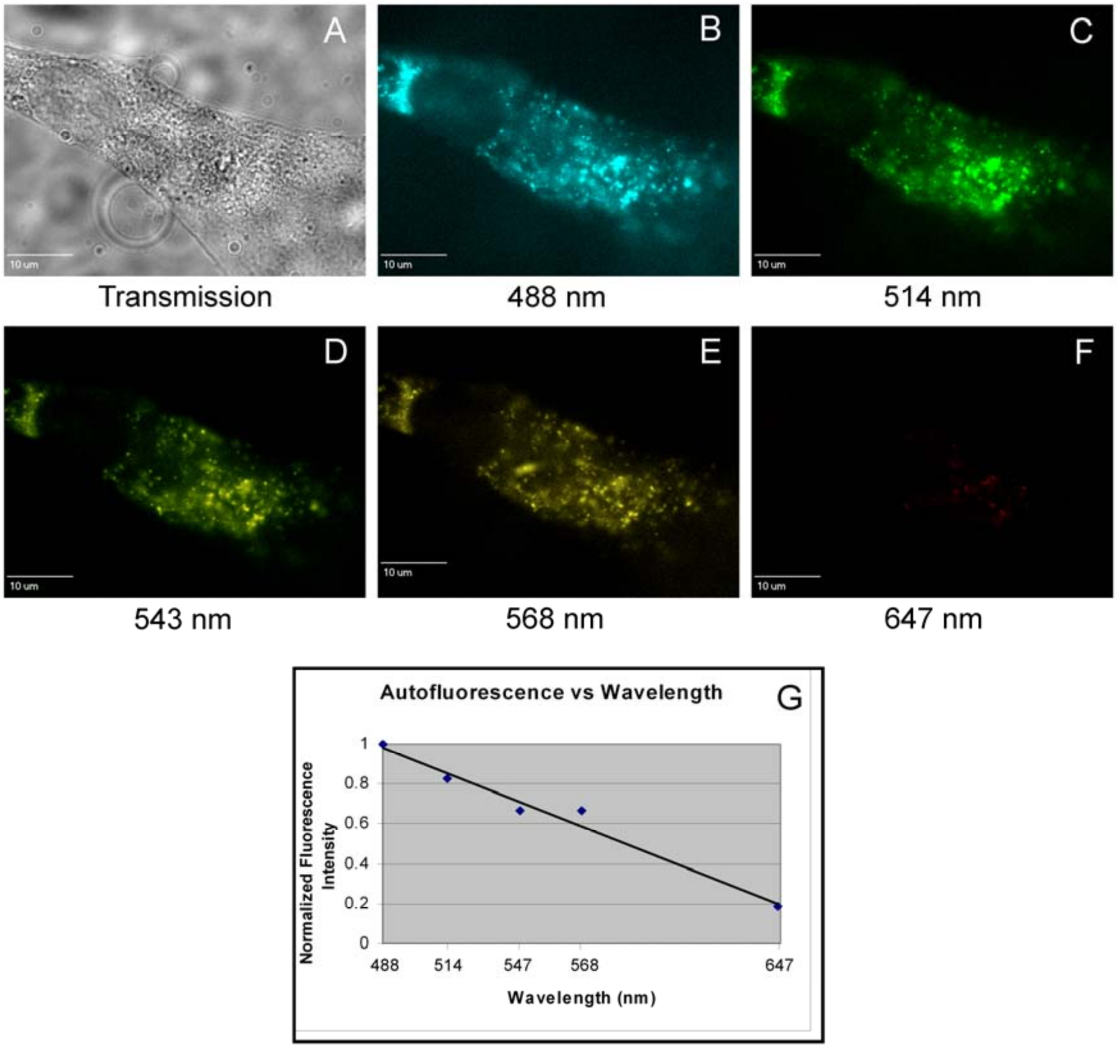

Figure 3.5 Far-field images of intrinsic autofluorescence of a chemically fixed HASM cell probed by different excitation wavelengths. The overall shape and condition of the cell is visible in the transmission image (A). The autofluorescence from the cell was collected following irradiation with 5 mW 488 nm (B), 514 nm (C), 543 nm (D), 568 nm (E), and 647 nm (F) excitation light. The decrease in autofluorescence intensity is evident as the excitation wavelength is increased. The autofluorescence at each wavelength was normalized to the intensity of the autofluorescence seen following 488 nm excitation. The normalized intensities are plotted (G) illustrating the wavelength-dependent nature of cellular autofluorescence.

As seen in Fig. 3.5, the intensity of the autofluorescence within the HASM cell significantly decreases as the excitation wavelength is increased. The total fluorescence intensities at each wavelength are also plotted (Fig. 3.5E), indicating a decrease in autofluorescence with an increase in excitation wavelength. These have been normalized to the highest autofluorescence intensity, which resulted from cells excited at 488 nm. As seen, utilizing 647 nm excitation reduces the autofluorescence background nearly an order of magnitude below that measured following 488 nm excitation. Recall, however, that Equation 3.1 shows that the maximal resolution of a lens-based optical technique is one half of the excitation wavelength. Thus, by using longer wavelength excitation light to avoid autofluorescence, the optical resolution suffers accordingly.

The resolution of NSOM, on the other hand, is independent of wavelength and only depends on the aperture diameter and its distance from the sample. Because of this, the use of long wavelength excitation radiation can be utilized to avoid autofluorescence while maintaining the high spatial resolution necessary for probing the distribution and interactions of biological components of interest.

This capability is demonstrated in Fig. 3.6 where Fig. 3.6A shows a far-field fluorescence image of a fixed and dried HASM cell in which the F-actin has been labeled with Alexa Fluor 647-conjugated phalloidin. The use of 647 nm excitation has essentially eliminated the background resulting from autofluorescence, although the resolution suffers as the FWHM of the smallest features in the image are approximately 350 nm. Figure 3.6B shows a 30 μm x 30 μm NSOM fluorescence image of the region of the same cell outlined by the box in 3.6A. Again, the use of 647 nm excitation was used in this measurement. A punctate distribution of the actin labeling emerges with a wavelength independent resolution of approximately 75 nm. Figure 3.6C depicts the simultaneously collected topography of the cell surface which can be used to confirm the location of many of the actin fibers located just beneath the plasma membrane.

As discussed, the benefits of the simultaneous high-resolution force and fluorescence data collected by NSOM have made it a favorable technique for studies on cellular samples. Additionally, the small excitation volumes and the wavelength independent resolution demonstrated by NSOM allow for superior specificity and detection limits for the location and distribution of cellular components at the upper cell membrane, which has proven difficult to achieve with other optical techniques.

3.4 NSOM in Practice

The spatial resolution attained in NSOM is highly dependent on two key factors; the size and quality of the aperture through which the excitation light passes and the distance between the aperture and the sample. The common methods and techniques utilized for successfully implementing NSOM will be discussed, with a focus on the methods used in our lab.

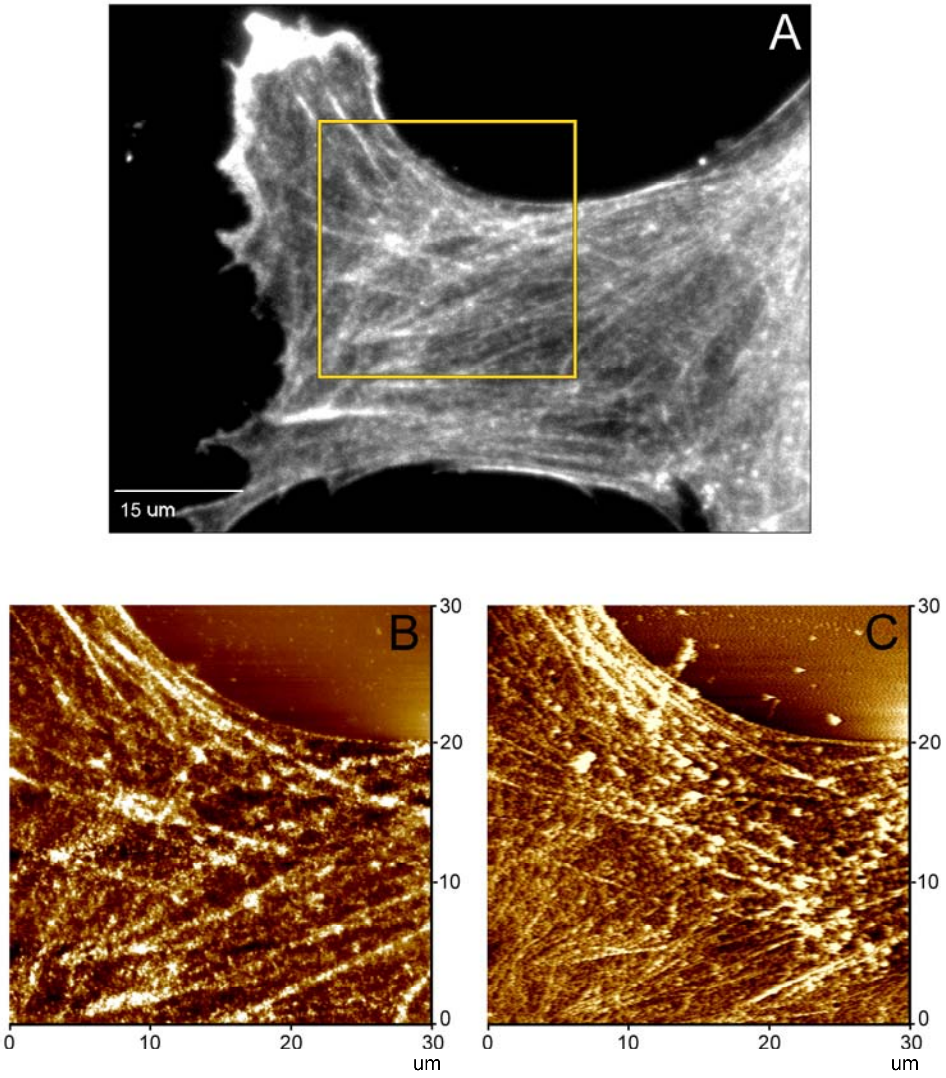

Figure 3.6 A HASM cell in which F-actin has been labeled with a phalloidin-Alexa Fluor 647 conjugate and excited with 647 nm radiation. The far-field image (A) demonstrates the utility of utilizing a long wavelength excitation source to reduce autofluorescence and increase signal-to-noise. The resolution in the image suffers as a result of the long wavelength excitation source and exhibits a FWHM of the smallest feature size of ~350 nm. (B) NSOM fluorescence image of the 30 μm x 30 μm region of the cell outlined in (A) in which the punctate labeling pattern of the F-actin becomes apparent, demonstrating the wavelength-independent resolution of NSOM. The FWHM of the smallest feature size is ~75 nm. (C) The simultaneously collected NSOM topography of the cell surface which can be used to confirm the location of many of the actin fibers located just beneath the plasma membrane (B).

3.4.1 Fabrication of NSOM Probes

Though many methods of aperture formation have been explored, the most common have revolved around the use of tapered waveguides. Currently, the most established technique involves the formation of a taper in a single mode fiber optic resulting in its termination at a fine point. The most common method of probe fabrication requires heating and pulling a single mode optical fiber, resulting in a taper terminating at a small point that eventually forms the NSOM aperture.[29] A second method of forming NSOM probes uses chemical etching techniques to create the taper in the fiber. This method uses hydrofluoric acid (HF) as the etchant and usually employs some type of organic protection layer. The probe is dipped into the HF and the meniscus formed by the HF/organic layer at the fiber determines the overall shape and cone angle of the tip.[30, 31] While the pulling method generally provides a smoother taper in the probe, etching methods can create much smaller aspect ratio tapers which have advantages for light throughput.[30, 32]

To confine the light within the tapered region, the sides of the probe are coated with a reflective metal. For the visible region of the spectrum, aluminum is the most reflective option, with a skin depth of ~13 nm at a wavelength of 500 nm. Generally, 50 nm – 100 nm of aluminum are coated around the tapers of the probes using evaporative techniques. Figure 3.7 shows magnified views of a typical fiber optic NSOM probe that has been coated with aluminum. In the electron microscopy image shown in Fig. 3.7A, the granules from the aluminum coating are visible as is the aperture at the very end of the probe where the light emerges. The aperture is

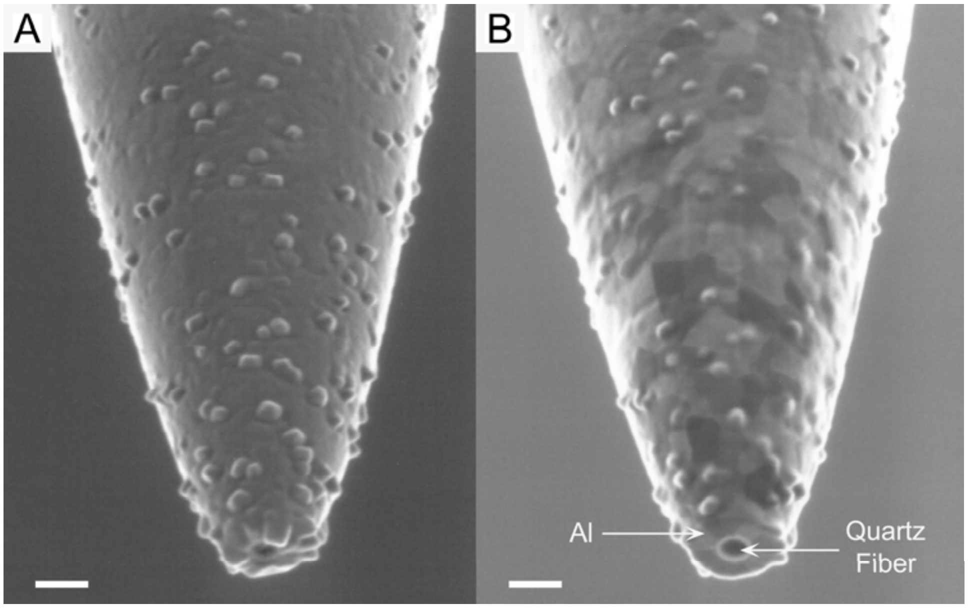

Figure 3.7 (A) Scanning electron micrograph of a tapered, single-mode fiber optic near-field probe coated with aluminum to confine light. (B) The same probe after the end has been milled with the use of a focused ion beam (FIB) instrument. Scale bars are 150 nm.

more apparent in Fig. 3.7B which shows the same probe after milling with a focused ion beam (FIB) instrument.

3.4.1a Probe Fabrication in Our Lab

Our lab primarily relies on NSOM probes produced by the heating and pulling method. Specifically, a Sutter Instruments model P-200 micropipette puller is used to heat single mode fiber optic with a CO_2 laser followed by mechanically pulling to draw the fiber down to a taper and eventual aperture. Careful control of the heating and pulling parameters allows for the formation of NSOM probes exhibiting a wide variety of taper geometries. For example, while the manufacture and use of NSOM probes exhibiting a “dolphin nose” shape, as shown in Fig 3.8A, provide for higher light throughput efficiencies, the formation of progressively longer tapers (Fig. 3.8B and 3.8C) results in the formation of smaller apertures.[3, 33, 34] A detailed discussion concerning light propagation and confinement within NSOM probes and the effects on throughput efficiencies will be discussed in Chapter 4.

Once the taper in the fiber optic has been formed, a homebuilt vacuum deposition chamber is used to evaporatively coat aluminum onto the taper of the probe. This confines the excitation light within the taper region and forms an aperture at the apex of the probe. Specifically, the tips are held in a mechanical spinner above the aluminum sample. A 1.0 mm diameter, 5 cm piece of pure aluminum wire (99.9999% pure) is formed into a ball and placed in a thermal “boat” constructed from a 1.0 cm x 5.0 cm x 0.0035 cm piece of tantalum metal. The

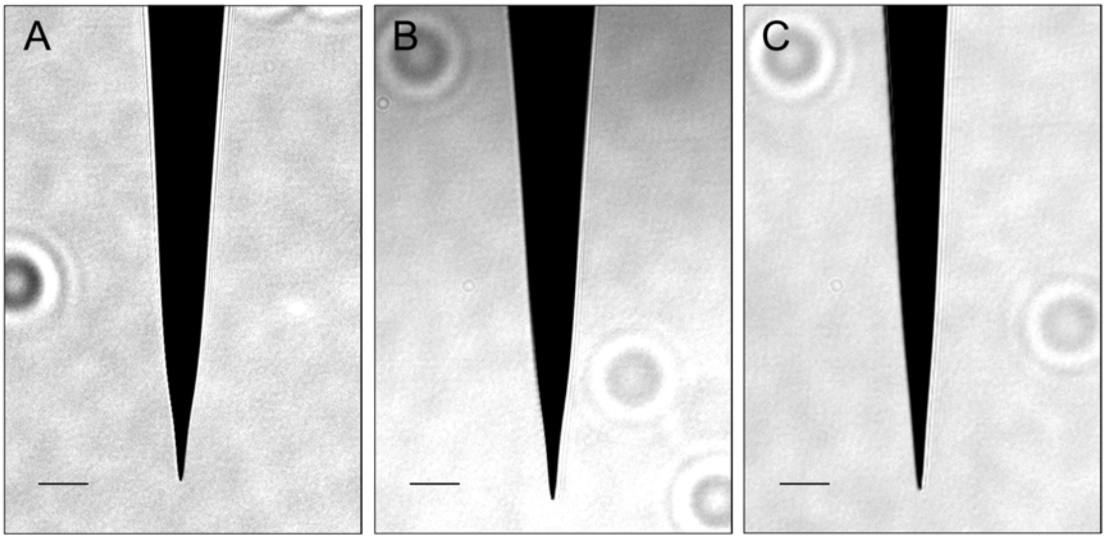

NSOM Probe	Heat	Velocity	Delay	Pull
A	310	20	126	75
B	315	35	126	75
C	315	41	126	81

Figure 3.8 Contrast images of NSOM probes fabricated by the heating and pulling method and coated with ~100 nm of aluminum. Careful control of the parameters used allows for the manufacture of probes with numerous taper geometries. The extreme "dolphin nose" taper in (A) represents the most efficient NSOM probe design while the progressively longer and straighter tapers (B) and (C) exhibit lower throughput efficiencies, but smaller apertures and higher resolution, respectively. Scale bars are 50 µm. A list of the pulling parameters for each probe design is outlined in the table.

tantalum boat consists of a small well to hold the aluminum and is placed across two electrodes within the vacuum chamber. Once a pressure $\leq 7.5 \times 10^{-5}$ torr is reached, a mechanical spinner is used to rotate the tapered fibers along their axis at a rate of ~5Hz at an angle of 35° from parallel.

Resistive heating of the tantalum boat rapidly melts then evaporates the aluminum. A shutter located between the aluminum sample and the rotating fibers are opened and the rate and overall thickness of the aluminum coating deposited is monitored using a gold coated quartz crystal located above the rotating probes. It has been found that a thickness of approximately 6.5 kÅ - 7.5 kÅ as measured by the deposition monitor corresponds to a thickness of ~50 nm – 100 nm on the probes themselves and is able to efficiently confine excitation light within the taper. Furthermore, depositing the aluminum as rapidly as possible (~800 Å/sec – 1000 Å/sec) results in the highest quality coatings as it reduces the formation of Al_2O_3 in the coating. Specifically, this leads to smoother, more reflective coatings with less defects.[35] The probes are then individually evaluated by coupling laser light into the distal end of the probe and visualizing the emission pattern from the aperture at the apex with a 100X 0.95 NA air objective.

3.4.2 Implementing Feedback

Once the NSOM probe is formed, high-resolution NSOM measurements rely on the ability to position and maintain the probe within nanometers of the sample surface. A number of methods have been developed which include approaches based on shear-force feedback[36-38], tapping-mode,[39, 40] and tuning fork feedback.[41] All of these methods generally rely on oscillating the tip and monitoring changes in amplitude as it interacts with the surface. A feedback loop is implemented which moves the probe relative to the sample surface to keep the amplitude of the tip oscillation constant. All these methods enable nanometric control over the tip-sample gap and generate a force mapping of the sample topography, much like AFM. NSOM, therefore, provides simultaneous optical and topographical information about sample properties.[42]

3.4.2a Shear-Force Feedback for Controlling Probe-Sample Distances

Though several methods exist for maintaining the nanometric probe-sample distance necessary for successful NSOM measurements, experiments reported here used the shear-force feedback technique in order to locate the sample surface with the probe. Figure 3.9 shows a schematic illustrating the design of a NSOM head and the method by which it generates a feedback signal. The probe is fastened to a piezoelectric bimorph which dithers the NSOM tip at its resonance frequency. Light from an infrared (IR) diode laser is directed towards the shaft of the probe and the shadow is measured on a split photodiode detector. The probe oscillation signals from the photodiodes are sent to the differential input of lock-in amplifier referenced to the AC signal driving the bimorph oscillation. The resulting DC output signal corresponds to the amplitude of the probe oscillation. The bimorph holding the tip is fastened to a z-piezoelectric tube, used to move the tip towards the sample surface.

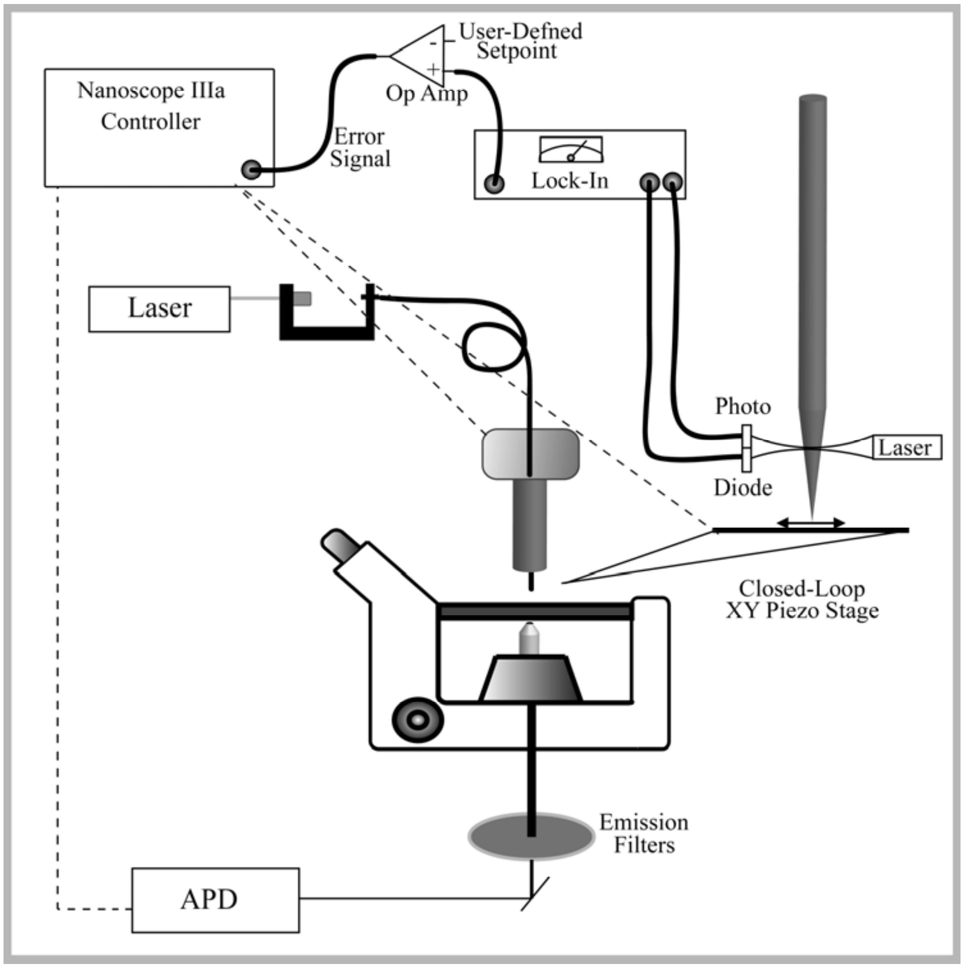

Figure 3.9 Schematic diagram of a NSOM setup utilizing shear-force feedback to maintain distance control between the probe and the sample.

As the tip approaches the sample surface, frictional forces dampen the amplitude of the probe oscillation and result in a decrease in the DC signal from the lock-in. An active feedback system is implemented by utilizing a differential amplifier to subtract a user-defined setpoint from the DC signal from the lock-in, creating an error signal. The z-piezo moves the tip vertically to maintain the error signal, thus maintaining the probe at a constant force above the sample. This feedback system maintains the tip-sample gap as the sample is scanned beneath the probe with an XY piezoelectric stage, resulting in a topographical force image similar to that attained by AFM.

3.4.3 Fluorescence Collection

The simultaneously collected high-resolution fluorescence is achieved by coupling excitation light into the distal end of the fiber optic NSOM probe, allowing it to exit the nanometric aperture at the apex. As illustrated in Fig. 3.1, because active feedback holds the probe aperture nanometers from the sample surface, the exiting excitation light interacts with the surface with dimensions similar to that of the probe aperture. Fluorescence from dye molecules located within the excitation volume of the probe is collected through an objective centered beneath the probe aperture and focused through appropriate emission filters onto an avalanche photodiode (APD) detector. The digital signal from the APD is then sent to the controller which simultaneously maps the fluorescence signal with the topography from the force image as the sample is scanned beneath the probe with a closed-loop XY piezo stage.

Combining the use of high quality NSOM probes with a sensitive feedback mechanism allows for the high spatial resolution and low detection limits attainable by NSOM. These capabilities are specifically demonstrated in Fig. 3.10 which shows a NSOM fluorescence image of the dye molecule diIC$_{18}$ (1,1'-dioctadecyl-3,3,3',3'-tetramethylindocarbocyanine perchlorate) doped into a DPPC (L-α-dipalmitoyl-phosphatidycholine) lipid monolayer. Each bright spot in this image represents the fluorescence from a single dye molecule in the lipid monolayer which illustrates the single-molecule detection limits of NSOM. Since the dye molecule is much smaller than the NSOM aperture, the size of each fluorescence feature in Fig. 3.10 reveals the size of the NSOM aperture used to image the sample. The full-width-half-maximum (FWHM) of the features in Fig. 3.10 is approximately 25 nm, which is roughly an order of magnitude better than the diffraction limit, and illustrates the high spatial resolution possible with NSOM.

3.5 Summary

As outlined in this chapter, progress in using NSOM to probe biological samples has been slowed by the technical difficulties involved, but now seems poised to take its place among other complementary techniques. The high-resolution fluorescence and force information seems particularly well-suited for biological applications where both contrast mechanisms can add unique insights. This combined with the single-molecule detection limits and spectroscopic capabilities offers a powerful set of tools for the biological sciences, although concerns such as light-induced probe heating continue to keep the use of NSOM on biological samples from being routine.

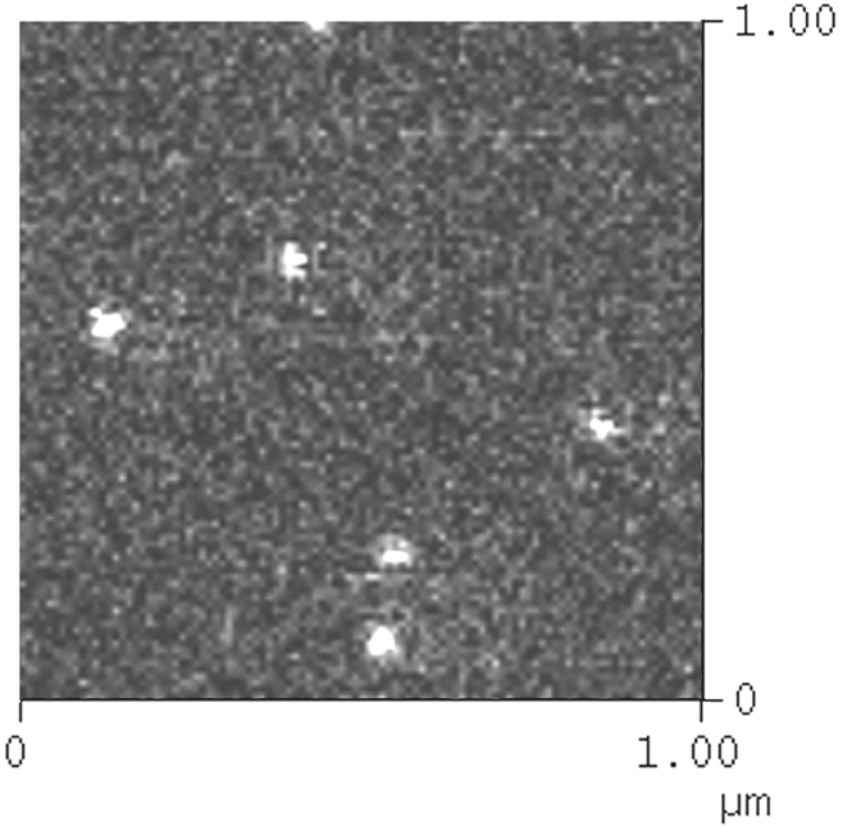

Figure 3.10 A 1.0 µm x 1.0 µm NSOM fluorescence image of single diI molecules entrapped within a thin PMMA matrix. The full-width-half-maximum of the intensity features is ~25 nm, which reflects the size of the NSOM aperture used in the imaging.

3.6 References

(1) Abbe, E., Beitrage zur Theorie des Mikroskops und der Mikroskopischen wahrnehmung. *Arch. Mikrosk. Anat.* **1873,** 9, 413-468

(2) Born, M.; Wolf, E., *Principles of Optics*. 7th (expanded) ed ed.; Cambridge University Press: Cambridge, U.K., 1997.

(3) Novotny, L.; Hecht, B., *Principles of Nano-Optics*. 1st ed ed.; Cambridge University Press: New York, 2006; p 539.

(4) Pohl, D. W., Optics at the nanometre scale. *Philosophical Transactions of the Royal Society of London Series a-Mathematical Physical and Engineering Sciences* **2004,** 362, (1817), 701-717.

(5) Synge, E. H., A suggested method for extending microscopic resolution into the ultra-microscopic region. *Philos. Mag.* **1928,** 6, 356-362.

(6) Synge, E. H., A microscopic method. *Philos. Mag.* **1931,** 11, (68), 65-80.

(7) Ash, E. A.; Nicholls, G., Super-Resolution Aperture Scanning Microscope. *Nature* **1972,** 237, (5357), 510-&.

(8) Lewis, A.; Isaacson, M.; Harootunian, A.; Muray, A., Development of a 500 A spatial resolution light microscope. *Ultramicroscopy* **1984,** 13, 227-232.

(9) Durig, U.; Pohl, D. W.; Rohner, F., Near-Field Optical-Scanning Microscopy. *J. Appl. Phys.* **1986,** 59, (10), 3318-3327.

(10) Pohl, D. W.; Denk, W.; Lanz, M., Optical stethoscopy: Image recording with resolution λ/20. *Appl. Phys. Lett.* **1984,** 44, (7), 651-653.

(11) Betzig, E.; Lewis, A.; Harootunian, A.; Isaacson, M.; Kratschmer, E., Near-field scanning optical microscopy (NSOM). Development and biophysical application. *Biophys. J.* **1986,** 49, (1), 269-79, 375.

(12) Dunn, R. C., Near-Field Scanning Optical Microscopy. *Chem. Rev.* **1999,** 99, (10), 2891-2928.

(13) Edidin, M., Near-field scanning optical microscopy, a siren call to biology. *Traffic* **2001,** 2, (11), 797-803.

(14) Mcconnell, H. M., Structures and Transitions in Lipid Monolayers at the Air-Water-Interface. *Annu. Rev. Phys. Chem.* **1991,** 42, 171-195.

(15) Mohwald, H., Phospholipid and Phospholipid-Protein Monolayers at the Air/Water Interface. *Annu. Rev. Phys. Chem.* **1990,** 41, 441-476.

(16) Shiku, H.; Dunn, R. C., Direct Observation of DPPC Phase Domain Motion on Mica Surfaces under Conditions of High Relative Humidity. *J. Phys. Chem. B* **1998,** 102, (19), 3791-3797.

(17) Shiku, H.; Dunn, R. C., Domain formation in thin lipid films probed with near-field scanning optical microscopy. *J. Microsc.* **1999,** 194, (2/3), 455-460.

(18) Vickery, S. A.; Dunn, R. C., Direct Observation of Structural Evolution in Palmitic Acid Monolayers following Langmuir-Blodgett Deposition. *Langmuir* **2001,** 17, (26), 8204-8209.

(19) Hollars, C. W.; Dunn, R. C., Submicron structure in L-a-Dipalmitoylphosphatidylcholine monolayers and bilayers probed with confocal, atomic force, and near-field microscopy. *Biophys. J.* **1998,** 75, (1), 342-353.

(20) Schlegel, R. A.; Williamson, P., Phosphatidylserine, a death knell. *Cell Death Differ.* **2001,** 8, (6), 551-63.

(21) Silvius, J. R.; Nabi, I. R., Fluorescence-quenching and resonance energy transfer studies of lipid microdomains in model and biological membranes. *Mol. Membr. Biol.* **2006,** 23, (1), 5-16.

(22) Rao, M.; Mayor, S., Use of Forster's resonance energy transfer microscopy to study lipid rafts. *Biochim. Biophys. Acta.* **2005,** 1746, (3), 221-33.

(23) Jares-Erijman, E. A.; Jovin, T. M., FRET imaging. *Nat. Biotechnol.* **2003,** 21, (11), 1387-1395.

(24) Selvin, P. R., The renaissance of fluorescence resonance energy transfer. *Nat. Struct. Biol.* **2000,** 7, (9), 730-734.

(25) Sekatskii, S. K., Fluorescence resonance energy transfer scanning near-field optical microscopy. *Philosophical Transactions of the Royal Society of London Series a-Mathematical Physical and Engineering Sciences* **2004,** 362, (1817), 901-919.

(26) Shubeita, G. T.; Sekatskii, S. K.; Dietler, G.; Letokhov, V. S., Local fluorescent probes for the fluorescence resonance energy transfer scanning near-field optical microscopy. *Appl. Phys. Lett.* **2002,** 80, (15), 2625-2627.

(27) Vickery, S. A.; Dunn, R. C., Scanning near-field fluorescence resonance energy transfer microscopy. *Biophys. J.* **1999,** 76, (4), 1812-1818.

(28) Troy, T.; Jekic-McMullen, D.; Sambucetti, L.; Rice, B., Quantitative comparison of the sensitivity of detection of fluorescent and bioluminescent reporters in animal models. *Mol. Imaging.* **2004,** 3, (1), 9-23.

(29) Betzig, E.; Trautman, J. K.; Harris, T. D.; Weiner, J. S.; Kostelak, R. L., Breaking the Diffraction Barrier - Optical Microscopy on a Nanometric Scale. *Science* **1991,** 251, (5000), 1468-1470.

(30) Hoffmann, P.; Dutoit, B.; Salathe, R.-P., Comparison of mechanically drawn and protection layer chemically etched optical fiber tips. *Ultramicroscopy* **1995,** 61, (1-4), 165-170.

(31) Turner, D. R. U.S. Patent No. 4,469,554, 1984.

(32) Moar, P.; Ladouceur, F.; Cahill, L., Numerical analysis of the transmission efficiency of heat-drawn and chemically etched scanning near-field optical microscopes. *Appl. Optics* **2000,** 39, (12), 1966-1972.

(33) Lazarev, A.; Fang, N.; Luo, Q.; Zhang, X., Formation of fine near-field scanning optical microscopy tips. Part I. By static and dynamic chemical etching. *Rev. Sci. Instrum.* **2003,** 74, (8), 3679-3683.

(34) Valaskovic, G. A.; Holton, M.; Morrison, G. H., Parameter Control, Characterization, and Optimization in the Fabrication of Optical-Fiber near-Field Probes. *Appl. Optics* **1995,** 34, (7), 1215-1228.

(35) Hollars, C. W.; Dunn, R. C., Evaluation of thermal evaporation conditions used in coating aluminum on near-field fiber-optic probes. *Rev. Sci. Instrum.* **1998,** 69, (4), 1747-1752.

(36) Betzig, E.; Finn, P. L.; Weiner, J. S., Combined shear force and near-field scanning optical microscopy. *Appl. Phys. Lett.* **1992,** 60, (20), 2484-6.

(37) Shalom, S.; Lieberman, K.; Lewis, A.; Cohen, S. R., A Micropipette Force Probe Suitable for near-Field Scanning Optical Microscopy. *Rev. Sci. Instrum.* **1992,** 63, (9), 4061-4065.

(38) Toledocrow, R.; Yang, P. C.; Chen, Y.; Vaeziravani, M., Near-Field Differential Scanning Optical Microscope with Atomic Force Regulation. *Appl. Phys. Lett.* **1992,** 60, (24), 2957-2959.

(39) Talley, C. E.; Cooksey, G. A.; Dunn, R. C., High resolution fluorescence imaging with cantilevered near-field fiber optic probes. *Appl. Phys. Lett.* **1996,** 69, (25), 3809-3811.

(40) Muramatsu, H.; Chiba, N.; Homma, K.; Nakajima, K.; Ataka, T.; Ohta, S.; Kusumi, A.; Fujihira, M., Near-Field Optical Microscopy in Liquids. *Appl. Phys. Lett.* **1995,** 66, (24), 3245-3247.

(41) Naber, A.; Maas, H. J.; Razavi, K.; Fischer, U. C., Dynamic force distance control suited to various probes for scanning near-field optical microscopy. *Rev. Sci. Instrum.* **1999,** 70, (10), 3955-3961.

(42) Paesler, M. A.; Moyer, P. J., *Near-field optics : theory, instrumentation, and applications*. 1st ed ed.; J. Wiley: New York, 1996; p xii, 355 p.

Chapter 4

Characterization of Power-Induced Heating and Damage in Fiber Optic Probes for Near-Field Scanning Optical Microscopy

4.1 Introduction

As described in detail in the previous chapter, near-field scanning optical microscopy (NSOM) is a scanning probe technique that allows for the simultaneous collection of high-resolution fluorescence and topographic data.[1-3] These inherent advantages make NSOM an attractive tool for the study of location, distribution, and interaction of components within biological systems such as the study of vault proteins and nuclear pore complexes. However, its implementation for use on biological samples has been slow due to a number of concerns and technical challenges. Chapter 3 outlines improvements and modifications to many aspects of NSOM which were necessary for its extension to use on fragile biological samples. This chapter will outline studies addressing one such concern in which NSOM sample heating is quantified directly using a thermochromic polymer.

Critical to the success of aperture based (NSOM) is the probe itself, which generally consists of an aluminum-coated, tapered, single mode optical fiber that allows the delivery of light down to the nanometric dimension.[4] In an effort to improve imaging characteristics, much work has been devoted to understanding the propagation of light through NSOM probes.[5-8] As light travels down the taper region of an NSOM probe towards the aperture, the diameter of the fiber surpasses successive mode field diameters. This reduction of supported propagating modes results in the loss of light from the fiber core into the surrounding metal coating of the probe. This loss leads to heating of the probe near the aperture[9-12] and eventually to catastrophic probe failure at elevated light input powers.[3, 13, 14] Due to the small dimensions and fragile nature of the NSOM probes themselves, characterization of both probe heating and failure have been problematic.[3, 12, 15] However, understanding both of these processes is critical for improving NSOM capabilities and utilizing this technique on heat-sensitive biological samples such as nuclear membranes.

As detailed in Chapter 3, the taper in fiber optic NSOM probes is generally introduced using either the heating and pulling[4] or the chemical etching approaches.[16, 17] For simplicity, NSOM probes manufactured by the heating and pulling method and the chemical etching method will be referred to as pulled and etched probes, respectively. Both methods produce tapers in the fibers that terminate at small tips that, once coated around the sides with a metal, produce small light apertures suitable for NSOM measurements.[4, 5, 18] The main difference in tips fabricated with the two approaches is in the cone angle of the probe.[16] The chemical etching technique can produce much steeper tapers (larger cone angles) that results in highly efficient NSOM probes compared to those fabricated with the heating and pulling method.[16, 19] This is illustrated in Figure 4.1.

Figure 4.1A shows a phase contrast image of a pulled probe while the probe in 4.1B was produced by the chemical etching method. Both probes were coated around the taper with ~100 nm of aluminum, forming nanometric apertures from which light

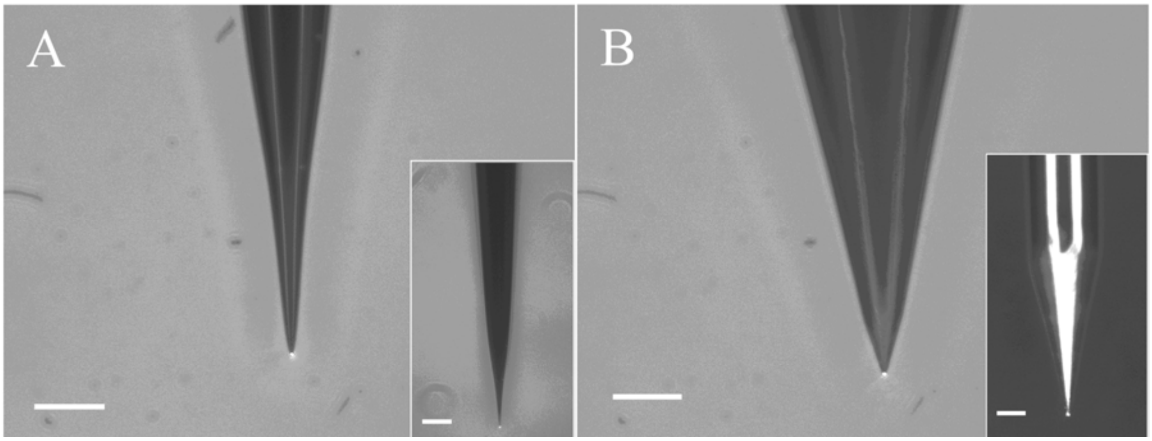

Figure 4.1 Magnified views of fiber optic NSOM probes fabricated with the (A) heating and pulling and (B) chemical etching methods. Each probe has a well-defined aperture indicated by the single spot of light emerging from the end of the tip. NSOM probes fabricated with the etching technique (B) have much larger cone angles which increases the efficiency of light delivery. Scale bars are 30 μm. The insets show expanded views where the scale bars are 50 μm.

is emitting, as seen in Fig. 4.1. Though the two methods both produce similarly sized and shaped apertures, numerous theoretical and experimental studies have found that the etched probes have significantly higher throughput efficiencies than pulled probes.[16, 20] Propagation of radiation through NSOM probes will be detailed in the next section, but a brief discussion is warranted for understanding differences in efficiencies as a function of probe geometry.

In an NSOM probe, the excitation radiation propagates toward the aperture as it is confined within the fiber by the reflective metal coating. Because of the conical taper required to produce nanometric apertures in the probes, the propagating radiation eventually reaches sequential mode cutoff diameters until ultimately no modes are supported.[5-8] At this point, the dielectric fiber no longer has the physical dimensions necessary to support propagation, resulting in the transition to a rapidly decaying evanescent wave. While calculations describing the attenuation of the evanescent field as it travels from the region of the mode cutoff to the aperture vary, the decay is known to be highly exponential.[3, 6, 21] Because of the larger cone angle in etched probes, the diameter of the dielectric fiber waveguide remains above the mode cutoff diameter closer to the probe aperture, resulting in the increased optical transmission in etched probes as compared to pulled.

The higher throughput of etched probes leads to a number of advantages such as decreased acquisition times for spectroscopic analysis including fluorescence and Raman measurements as well as making high density, nanometric read-write technology feasible.[5, 22] The increased efficiency of etched probes may also lead to differences in the heating characteristics and failure mechanism as compared to pulled NSOM probes, leading to further advantages for use on biological samples.[23] Comparisons of each will be explored and addressed in this chapter.

4.2 Concerns of NSOM Probe Heating

Concerns surrounding the compatibility of NSOM with biological samples sparked a number of investigations into the extent of NSOM probe and sample heating.[9, 11-13, 24-26] These concerns result directly from work done to understand radiation transmission in NSOM probes in which numerous computational studies have been undertaken in an effort to accurately describe light propagation through an NSOM probe.[5-8] In order to understand the characteristics of light as it passes through the taper region, Novotny and co-workers have utilized the multiple multipole method (MMP) which is capable of accurately modeling the fiber geometry, the surrounding metal thickness, and the effects of a surface near the probe aperture on the fields.[6, 27, 28] This work has shown that as the light passes through the taper region of the probe, it will encounter one mode cutoff after another as a result of the decreasing probe diameter. The last supported mode (HE_{11}) will eventually reach its cutoff at a fiber diameter of ~250 nm, after which the light becomes a purely evanescent field.[5] In this case, the transmission efficiency of the evanescent field becomes dependent on the distance from the aperture and decays exponentially.[3, 6, 21] The MMP studies were also able to determine that this attenuation is accounted for by primarily two factors. Firstly, beyond the cutoff diameter approximately 30% of the light is reflected back up the probe, resulting in a standing wave within the taper region itself. Secondly, approximately two thirds of the photons penetrate the metal coating and are dissipated as heat, leaving only a fraction of the radiation to exit the probe aperture.[7] The energy associated with this significant absorption of light is believed to result in a localized heating of the aluminum shell near the aperture of the NSOM probe. Because the diameter of the fiber at which the radiation within the probe becomes purely evanescent has been calculated to be ~250 nm, the small dimensions and fragile nature of the probes has made quantifying the degree of probe heating in this region difficult. Likely due to this difficulty, studies attempting to determine NSOM probe heating have revealed an array of results ranging from no increase in temperature to temperatures as high as 470 °C as the input power was increased.[10-12, 26, 29-31]

As mentioned in Chapter 3, light-induced heating of NSOM probes has raised concern as to its compatibility with fragile biological samples. The first experimental works indicating that light absorption by the metal coating results in a heating of the NSOM probe were accomplished independently by La Rosa *et al.*[11] and Kavaldjiev *et al.*[9] La Rosa utilized a technique in which infrared (IR) laser light was coupled into an NSOM probe and the resulting emission from the probe aperture was continuously monitored. The efficiency with which the IR light passed through the probe was directly calibrated to its temperature, allowing for the determination of probe temperature as a function of the input power of a second laser source (visible). From this, the authors were able to measure probe temperatures reaching ~390 °C prior to thermal damage and failure of the coating.

During this time, Kavaldjiev and co-workers were also investigating NSOM probe temperatures as a function of laser input powers. Their studies utilized a pump-probe technique to exploit the temperature-dependent reflectivity of metals. By monitoring the reflection of a 633 nm laser focused on the taper of the probe, they were able to correlate reflection intensity to probe temperature and determine that the probes were reaching temperatures of approximately 290 °C.[9]

Following these studies, Stähelin *et al.* measured probe temperatures by attaching a custom thermocouple along the taper region of the probe, tens of microns from the aperture.[12] This experiment found the highest recorded temperatures yet for an NSOM probe at 470 °C prior to probe failure. Since the temperature was recorded along the probe taper, however, it remained unclear how much heating the sample actually experienced under the aperture of the NSOM probe. Recent studies in our group using thermochromic samples provides a direct view of sample heating during NSOM measurements.[24]

Our group recently reported results using the "two-color" emission from a thermochromic polymer consisting of perylene and N-allyl-N-methylaniline (NA) to characterize sample heating under pulled NSOM probes.[24] The details of the polymer will be discussed in subsequent sections, but briefly the polymer can be electronically excited by irradiation with 405 nm laser light. The resulting emission has characteristic dual color maxima at ~475 nm and ~510 nm.[32] The intensity ratio of the two peaks is highly sensitive to the temperature of the polymer. By placing the NSOM probes directly over a thin film of the polymer and monitoring both the emission spectrum from the polymer and the probe output power, sample temperature as a function of output power was quantified. These measurements found that as output power from the NSOM probe increases, sample heating quickly rises and levels off at a maximum temperature of ~65 °C. As output power was further increased to 200 nW, no change was observed in the sample heating. The leveling off in sample heating was ascribed to differential expansion of the aluminum coating past the quartz core as the probe was heated. This effectively increases the distance between the probe aperture and the sample surface, resulting in less heat transfer from the probe to the sample.[10, 24] This differential expansion is believed to not only be responsible for the observed leveling off of the sample heating, but also for the destruction of NSOM probes at high input powers, which will be discussed in detail in following sections.

The larger cone angle and higher throughput efficiencies of etched NSOM probes over pulled tips has led to speculation that light-induced heating may be even lower in these highly efficient probes.[23] In an ongoing effort to find ways to make NSOM more amenable with biological samples, the light-induced heating of etched probes was specifically addressed utilizing the same perylene and NA polymer as in the previous study. Surprisingly, we found that the sample heating as a function of output power is strikingly similar to that experienced by pulled probes, despite their significantly higher throughput efficiencies.[13, 24] Thus, indicating that both types of

NSOM probes impart minimal sample heating and are therefore compatible with biological samples.

4.3 NSOM Probe Failure

The quality of any aperture-based NSOM probe is marked by a number of factors, but primarily by the size and quality of aperture formed by the metal coating. The loss of this sub-wavelength diameter aperture for any reason results in NSOM probe failure. Experimentally, this failure can occur for several reasons such as the probe crashing into the sample surface, physical damages to the aluminum coating resulting from lateral forces exerted on the probe during scanning, and light-induced probe failure resulting from coupling too much light into the probe. In all cases, failure is accompanied by a dramatic increase in optical transmission from the probe as the failure is known to be a result of damage to the metal coating near the apex. Light induced probe failure, in particular, has been of interest as increasing NSOM probe power thresholds would lead to higher power densities at the aperture and better signal-to-noise in fluorescence measurements. The exact mechanism of light-induced probe failure was largely unclear, although it had been attributed to either fracturing of the metal coating due to shear stresses or a melting of the metal coating itself.[3] We undertook a series of experiments in an effort to identify the precise mechanism of light-induced probe failure in tips produced both by the heating and pulling and the chemical etching methods.

To investigate tip failure in both etched and pulled probes, both probe types were monitored as a function of input power until they eventually failed. High-resolution imaging indicates that in both cases, failure results in a compromised metal coating near the apex, though the mechanisms of failure appear quite different. The pulled probes failed through a mechanism involving stress fractures in the metal coating caused by the differential thermal expansion of the dielectric fiber and surrounding metal coating. The etched probes, however, appear to fail as a result of melting of the aluminum shell. Explanations for these distinctly different mechanisms and their implications will be explored and discussed further.

4.4 Experimental

4.4.1 NSOM Instrument Configuration

Our NSOM instrument is built around an inverted Zeiss microscope (Axiovert 135TV) which has been fitted with a custom machined cast iron base made to accept the backplane from a Digital Instruments Bioscope AFM. A Nanoscope IIIa controller and a homebuilt NSOM head are utilized in conjunction with Digital Instruments Nanoscope software to monitor feedback and maintain the desired tip-sample gap. For these studies, all measurements were taken using straight tip geometry and shear-force feedback. Once the probe is held at the sample surface, excitation laser light is coupled into the distal end of the single mode fiber optic probe and exits the nanometric aperture held near the sample surface. The fluorescence radiating from the sample is collected by a 40X 1.30 NA oil objective, filtered with appropriate emission filters, and focused into a spectrograph (SpecrtaPro 300i, Acton Research Corporation) coupled to a CCD camera (DU420-BV, Andor Technology). An illustration of the specific instrumental design is outlined in Figure 4.2.

4.4.2 Methods of Manufacturing NSOM Probes

Etched NSOM probes were manufactured by the Turner method in which stripped and cleaved single mode fiber optic (460-HP, Nufern) is placed into a Teflon vial containing a 49% solution of hydrofluoric acid (HF).[16, 33] The acid is covered with a thin organic layer in order to protect the rest of the fiber from the HF vapors as well as to control the taper angle of the probe. The HF forms a meniscus at the fiber with a height proportional to the fiber diameter. As the fiber is etched away, its diameter decreases, causing the height of the meniscus to decrease as well. This results in an essentially self-terminating process that forms extremely reproducible tapers terminating at a fine apex. Because the geometry of the resulting etched fiber is dependent upon the meniscus profile, changing the organic layer results in the production of probes with different cone angles. In fact, studies characterizing the effect of the organic layer on the resulting taper angle found that cone angles from 8° to 41° could be achieved based on the choice of organic layer.[16] For all of the etched probes produced in these studies, silicon oil was employed as the organic protectant layer. Using a homebuilt vacuum deposition chamber, the probes are then coated with ~200 nm of aluminum around the taper in order to confine light and guide it to the aperture. Pulled NSOM probes were produced by mechanically heating

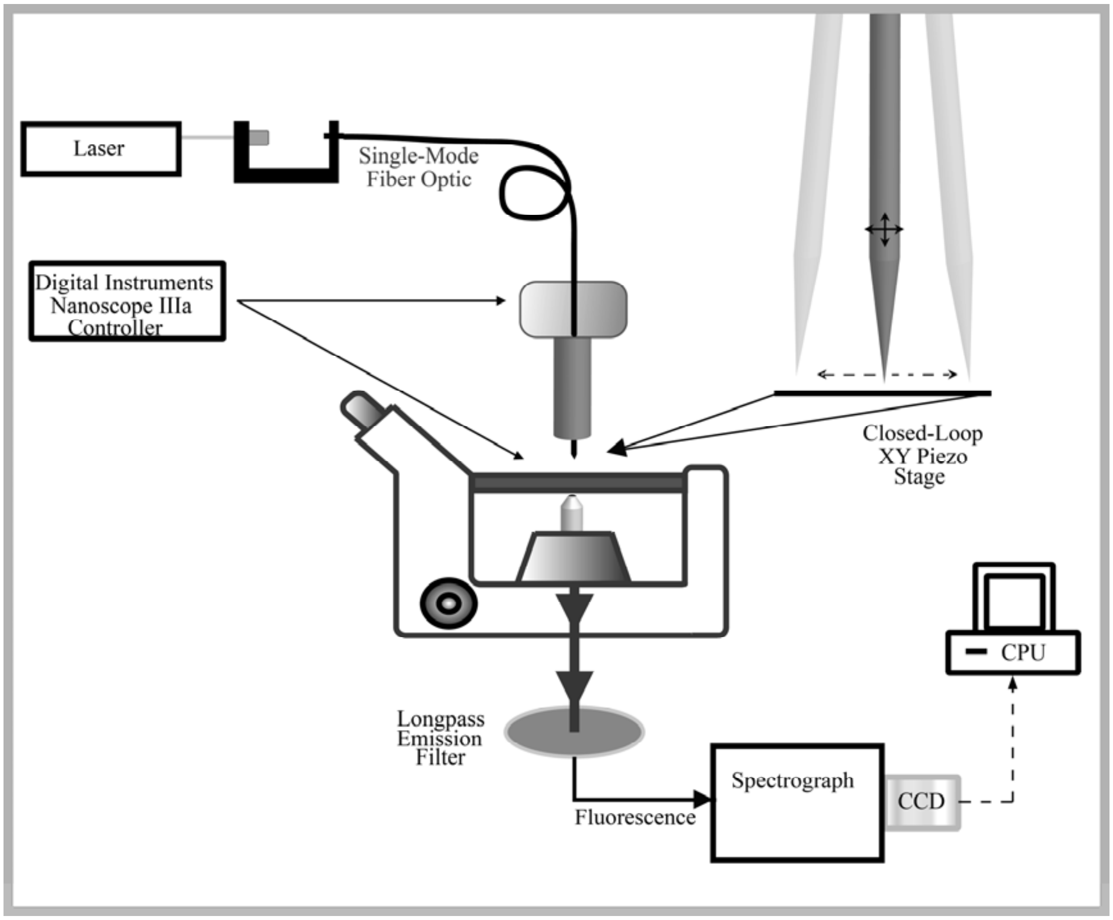

Figure 4.2 Schematic of the near-field scanning optical microscope utilized for probe heating studies. By collecting the fluorescence emission of a thermochromic polymer through a spectrograph and onto a CCD, NSOM sample heating was characterized as a function of output power from the probe.

and pulling a single mode fiber optic with a Sutter P-2000 micropipette puller. The taper of the pulled fibers was then coated with ~50-100 nm of aluminum in a similar fashion to the etched probes.

4.4.3 Composition and Characterization of a Thermochromic perylene-NA Polymer

The temperature sensitive perylene/N-allyl-N-methylanaline (NA) polymer was synthesized as previously described.[32] Briefly, a perylene chromophore and non-emissive N-allyl-N-methylanaline were encapsulated into a polystyrene matrix. The perylene alone has a relatively strong absorbance at the 405 nm excitation wavelength used and emits with a characteristic peak at ~475 nm. As the temperature of the polymer is decreased, the formation of a perylene/NA exiplex is stabilized, resulting in the growth of a red shifted emission peak at ~510 nm as seen in resulting from emission from the exiplex as outlined in Fig. 4.3. Alternatively, heating of the polymer results in a decrease in the ~510 nm exiplex emission peak. Heat transfer from NSOM probes to the sample was directly measured by coating a thin film of the perylene-NA polymer onto a glass coverslip, allowing for direct imaging by NSOM.

The emission characteristics of each batch of perylene/NA polymer are slightly different as a result of variances in concentrations of the polymer components, requiring calibration of each batch. The calibration of emission peak ratios and polymer temperature was carried out using a fluorimeter (Photon Technology International, Birmingham, NJ) while the polymer temperature was varied between 25°C and 85°C with a built-in water circulator.

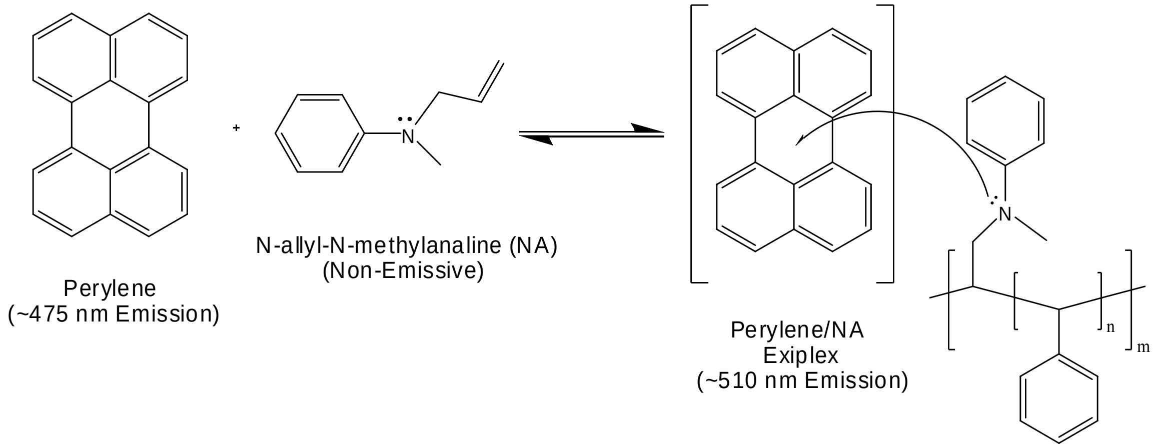

Figure 4.3 Chemical structures and maximum emission wavelengths for perylene, N-allyl-N-methylanaline, and the stabilized exiplex. The ratio of the emission peaks from perylene and the exiplex was calibrated to sample temperature in order to directly determine sample heating from NSOM.

4.4.4 Visualization of NSOM Probes following Light-Induced Damage

To visualize the mechanism of tip failure, both pulled and etched aluminum coated NSOM probes were imaged with high resolution in a focused ion beam (FIB) instrument (Micrion 9000) outfitted with a custom feed-through flange that allowed for introduction of the probes into the instrument while maintaining the necessary vacuum for operation of the FIB. Figure 4.4 shows the front (4.4A) and back (4.4B) views of the instrument with the distal ends of several NSOM probes exterior to the vacuum chamber (4.4C). These ends are then spliced to another fiber into which laser light is coupled, allowing for the simultaneous introduction of laser light into the probes and visualization of probe integrity with the FIB. High-resolution images of the NSOM probes were collected as a function of laser power (488 nm line, Coherent ENTCII-621 argon ion laser) coupled into the probe. Images of the tips were taken as the power coupled into the fiber was gradually increased until they ultimately underwent light-induced failure. In an effort to obtain even higher resolution images, some of the probes were monitored pre- and post-failure in a LEO 1550 scanning electron microscope (Carl Ziess, Inc., Thornwood, NY).

4.5 Results and Discussion

4.5.1 NSOM Probe Heating as a Function of Light Power

Figure 4.1 compares phase contrast images of NSOM probes fabricated (A) using the heating and pulling method and (B) the chemical etching technique. The sides of the taper have been coated with ~100 nm and ~200 nm of aluminum,

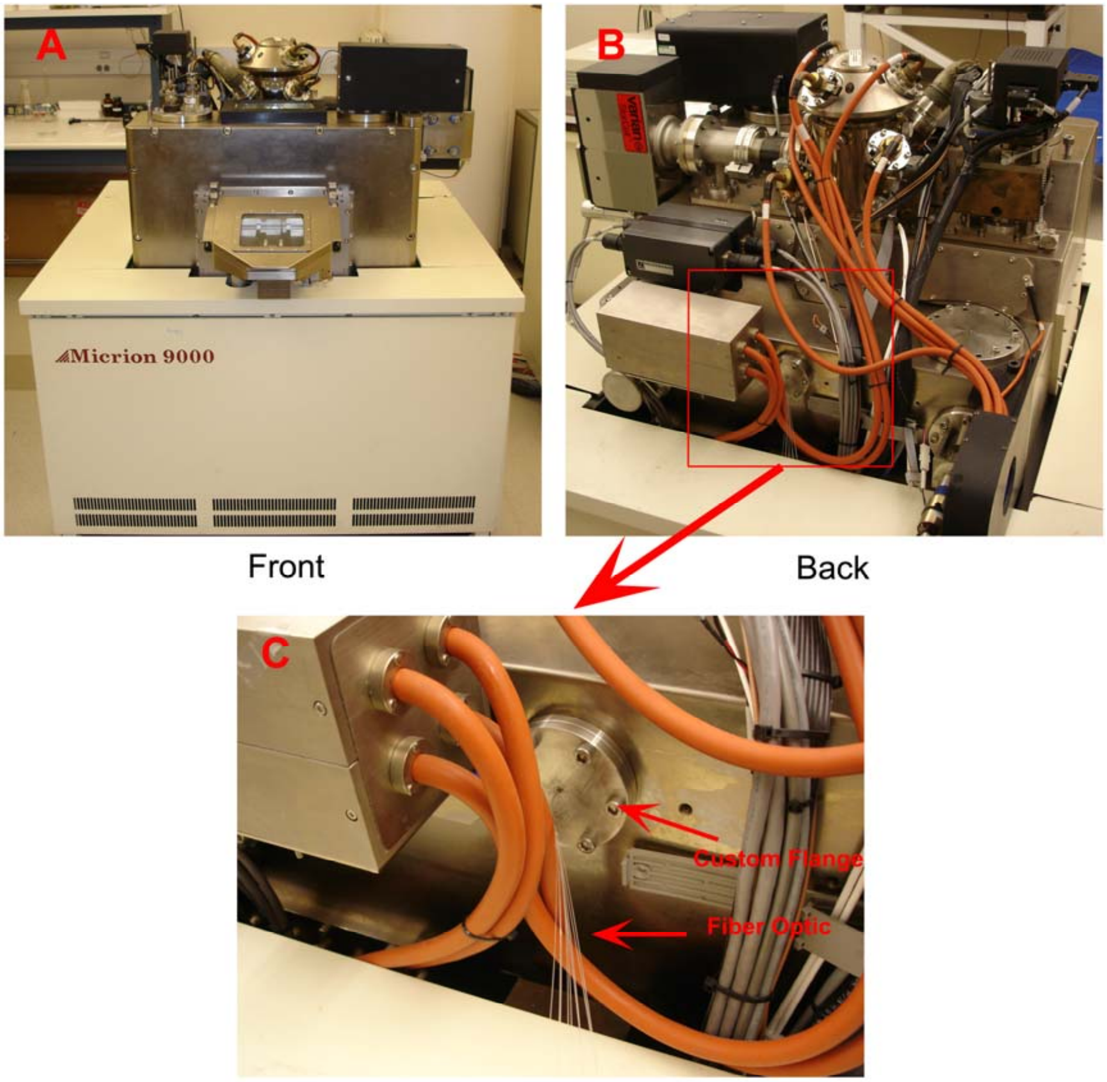

Figure 4.4 Focused ion beam (FIB) instrument utilized to monitor NSOM probe failure as a function of input power. Front (A) and Back (B) views of the FIB. (C) A close-up of the custom flange through which fibers are introduced into the vacuum chamber. This allows for the FIB to remain under vacuum and monitor the probes while laser light was coupled into the fibers exterior to the chamber.

respectively, to confine the light until exiting the aperture as a well-defined single spot of light as seen in Fig. 4.1. Figure 4.1 shows the much larger cone angle in the taper region of the etched probe (Fig. 4.1B) probe as compared to the pulled probe (4.1A). Specifically, the cone angle for the pulled probe in Fig. 4.1A is 6°, compared with 15° for the etched tip shown in Fig. 4.1B. The overall shapes of the probes are clearly seen in the insets of Fig. 4.1. While the entire taper region of the etched tip, starting from the 125 μm width the fiber optic, is visible, typical taper regions in pulled probes extend over a much greater distance of ~500 μm - 800 μm.

Recall that this large cone angle exhibited in etched probes situates the mode field cutoff diameter much closer to the aperture than in pulled probes. This has been directly linked to their high transmission efficiencies and has led to the speculation that sample heating from etched probes may be lower than for pulled probes which was measured previously.[3, 5, 20]

As done previously for pulled probes, a thermochromic polymer was used to characterize the sample heating experienced directly from etched NSOM probes.[24, 28] Figure 4.5 shows the temperature-dependent emission spectra of the perylene-NA polymer normalized to the 475 nm peak. Ratiometric measurements of the emission intensities from the 475 nm and 510 nm peaks provides an intrinsic measure of sample heating that is independent of excitation power.[24] This provides an ideal sample for quantifying sample heating as a function of output power from NSOM probes.

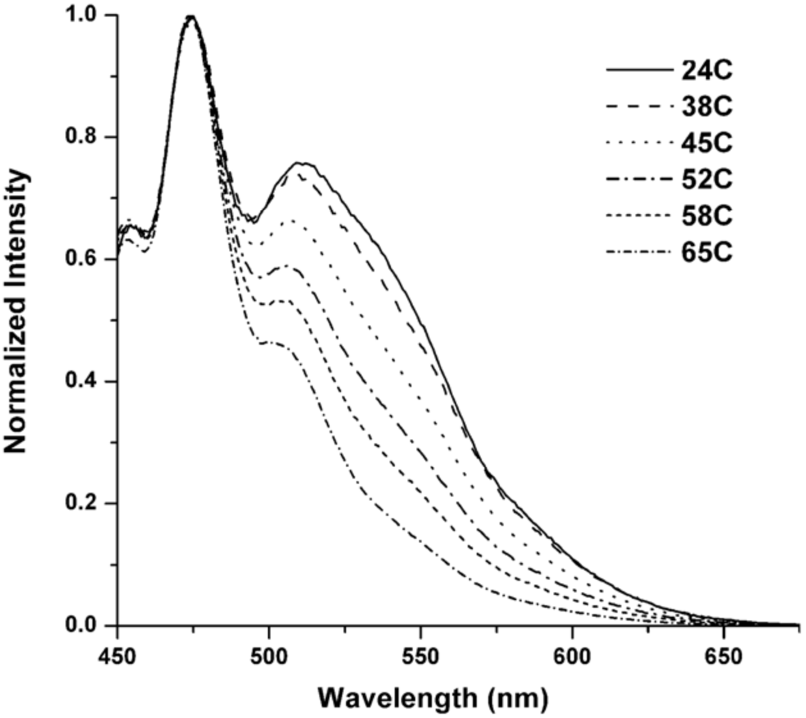

Figure 4.5 Bulk temperature dependent spectra of the thermochromic perylene and N-allyl-N-methylaniline polymer sample, normalized to the peak at 475 nm**.** The ratio of the emission peaks at 475 nm and 510 nm can be calibrated to report temperature independent of absolute excitation power.

Figure 4.6A shows a plot of sample temperature versus probe output power for several etched NSOM probes. The shear-force feedback method was used to hold the probes several nanometers from the polymer coated coverslip surface as the 405 nm excitation light was coupled into the probes. As the output power from the probe reaches 50 to 75 nW, the sample heating levels off at ~55 °C to 60 ^{o}C and remains constant with further power increases. The sample heating profile shown in Fig. 4.6A for etched NSOM probes is qualitatively similar to that measured previously with pulled probes in which a similar rise in sample temperature was observed with a maximal sample heating of ~55 ^{o}C to 65 ^{o}C at output powers of ~50 nW, illustrated in Fig. 4.6B.[24]

The longer taper of pulled probes leads to loss of light farther from the aperture when compared to the smaller aspect ratio etched probes. While this additional loss likely increases heating along the taper of the probe, our results show that this does not significantly increase the sample heating directly under the NSOM aperture. This result shows that while etched NSOM probes are vastly more efficient at delivering light, they apparently do not reduce sample heating when compared with pulled NSOMprobes.[24] However, both probe types impart only modest sample heating which suggests that NSOM utilizing either probe design should be compatible with thermally sensitive samples.

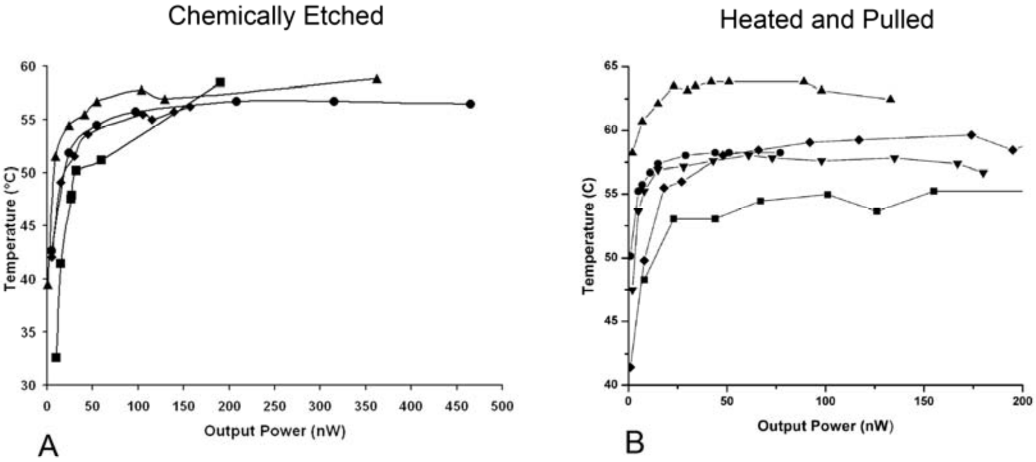

Figure 4.6 Plots of sample temperature versus output power for several chemically etched (A) and heated and pulled (B) NSOM probes. In both cases, the sample temperature quickly rises as a function of output power before leveling off at a sample temperature of ~50 °C – 60 °C. This figure was modified with permission from reference 24.

4.5.2 Thermal Expansion of Aluminum Coating

In the previous study, it was suggested that the leveling off of sample heating with increasing power arises from a mismatch in the heat-induced expansion of the aluminum coating and the fiber core.[24] Specifically, differences in the linear expansion coefficients for aluminum (α=22.2 x 10^{-6} K^{-1}) and quartz (α=0.59 x 10^{-6} K^{-1}) result in a differential expansion of the metal coating past the dielectric core of the NSOM probe as power is increased. These differences lead to the effective increase in distance between the fiber apex and the surface, thus reducing heating of the sample.[10] This differential expansion of the aluminum coating past the dielectric core likely also plays a role in light-induced probe failure as the stresses induced by the process overcome those maintaining the integrity of the aluminum coating.

4.5.3 Characterization of Light-Induced damage to NSOM Probes

In subsequent studies, the phenomenon of light-induced NSOM probe failure was investigated as increasing power is coupled into both pulled and etched NSOM probes. Fiber optic NSOM probes generally fail at high input powers resulting from the sudden loss of the aluminum coating near the aperture. This has been attributed to either mechanical failure due to shear stresses arising from the different thermal expansion coefficients of the dielectric core and metal shell or melting of the aluminum coating itself.[3, 14]

In order to characterize probe failure at elevated output powers, NSOM probes were observed at high resolution while increasing the power to the point of failure.

NSOM probes were introduced into the vacuum chamber of a focused ion beam (FIB) instrument through a custom flange that allowed fiber optic probes to be inserted while maintaining vacuum. This enabled the real time observation of tip failure at elevated powers.

Figure 4.7 shows a series of images of the same NSOM probe, fabricated using the heating and pulling method, taken as the input power was increased. Figures 4.7A – C were taken in real-time as laser power into the probe was slowly increased. Although not apparent in the images because the e^- detectors in the FIB are not sensitive to photons, light is visible exiting the aperture of the probe as the measurements are taken. Specifically, the series shows the same NSOM probe where no damage is observed (Fig. 4.7A), where damage to the aluminum coating initially appears (Fig. 4.7B), and finally following complete failure of the probe (Fig. 4.7C). While in Fig. 4.7A the input powers of ~1 mW have no apparent effect on the probe structure, increasing the input laser power to ~3 mW initiates the formation of a stress fracture seen in the aluminum coating (Fig.4.7B). The complete removal of the aluminum from the region below the fracture (Fig. 4.7C) was observed immediately after the collection of the previous image, indicating that once failure is initiated, it proceeds rapidly without a need for further increase in laser power. Again, although the emission from the probes is not visible in the images, the removal of the aluminum coating from the taper of the probe leads to the loss of the aperture and a dramatic increase in light throughput, signaling tip failure. The mechanism of this observed failure is attributed to shear stresses resulting from the differential

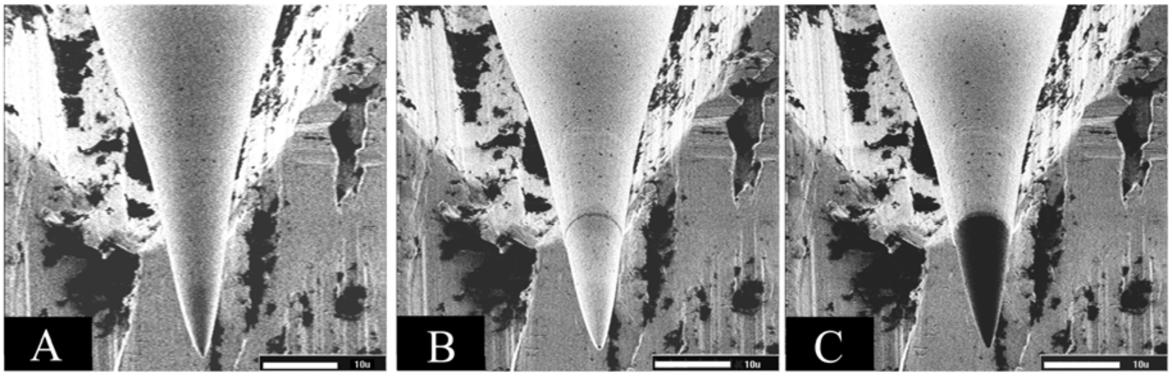

Figure 4.7 Series of high-resolution images of a pulled NSOM probe as power into the probe is increased. (A) At low powers, the probe appears normal and the aluminum coating is intact. (B) As the NSOM probe temperature increases at elevated output powers, a small stress fracture in the aluminum coating forms approximately 35 μm from the aperture of the tip. (C) Above the damage threshold, the aluminum coating below the fracture is lost, exposing the non-conductive dielectric which appears dark. The scale bar is 10 μm.

expansion of the aluminum past the quartz core as indicated by the observed stress fracture in Fig. 4.7B. Details of the failure mechanism are discussed in the next section.

For NSOM probes fabricated using chemical etching, the mechanism of probe failure is less clear, but appears to involve melting of the aluminum coating rather than the differential expansion as seen for pulled probes. Figures 4.8A and 4.8B show an etched NSOM probe before and after failure, respectively. Unlike the image shown in Fig. 4.7B, we have not found any clear evidence for a stress fracture preceding the ultimate failure of etched NSOM probes. The probe failure is rapid once the damage threshold is reached and the resulting removal of the metal coating is less uniform, as seen in a close-up view of the damaged region of the probe (Fig. 4.8C). Moreover, small islands that apparently reflect globular aluminum remain on the probe, suggesting a failure mechanism in which the aluminum coating melts at elevated light input powers.

A summary of the high-resolution studies of probe failure for both types of NSOM probes are compared in Fig. 4.9. As seen in Fig. 4.9, the taper diameter at which probe failure initiates is similar for both etched and pulled NSOM probes and occurs at a fiber diameter of approximately 6 µm. Although it is not clear exactly why the diameter at which failure initiates is consistently ~6 µm, theoretical work by Novotny and co-workers describing the inclusion of high intensity standing radiation waves within NSOM probes may be key in its understanding. In Fig. 4.9, the average distance from the point of failure to the tip apex for pulled probes is 35.2 ± 17.3 µm

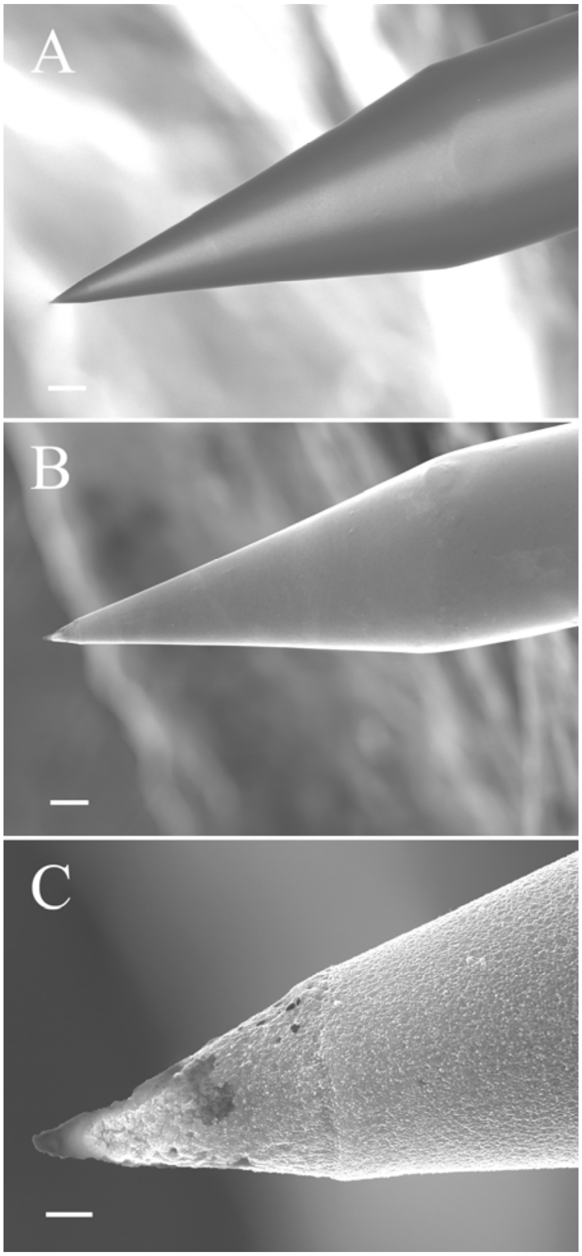

Figure 4.8 Series of high-resolution images of an etched NSOM probe prior to and following light-induced failure. Panels (A) and (B) show the etched NSOM probe before and after failure, respectively (scale bars are 20 μm). (C) Shows a magnified view of the NSOM probe following failure (scale bar is 2 μm).

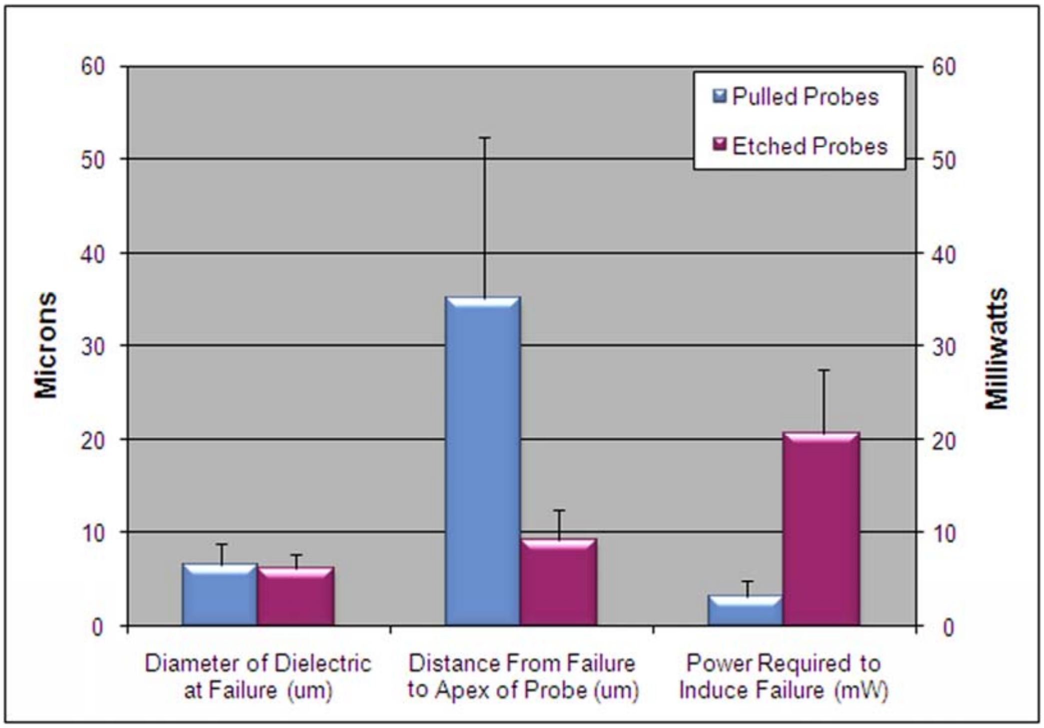

Figure 4.9 Comparison of the performance parameters for NSOM probes fabricated with the heating and pulling and etching methods. The average diameter of the fiber probe at which damage initiated was 6.63 ± 2.32 µm for pulled probes and 6.18 ± 1.53 µm for etched. The distance from the aperture to the initiation of failure was 35.2 ± 17.3 µm for pulled and 9.2 ± 3.4 µm for etched. The input power required for failure of the probes was 3.4 ± 1.7 mW for pulled tips and 20.7 ± 6.9 mW for etched. The data was obtained by combining the results from 12 pulled and 15 etched probes.

while it is only 9.2 ± 3.4 μm for the etched probes. Because the diameter at which failure initiates is essentially constant for both probe types, the lengths over which failure occurs are directly related to the probe cone angle. This explains the significantly longer distances from the initiation of failure to the apex of pulled versus etched probes.

There is also a large difference in the power required to cause tip failure in etched versus pulled probes which reflects the difference in taper angle (Fig. 4.8). For probes fabricated in our laboratory, the input power required to induce probe failure for pulled tips is 3.4 ± 1.7 mW while the power required to cause failure in etched probes was found to be approximately six times greater at 20.7 ± 6.9 mW. These input powers represent the actual power into the tip as coupling losses have been accounted for and tested after each measurement. As will be discussed later, it is believed that this observed increase in the optical destruction threshold of etched probes compared to pulled is directly related to the geometry of the tapers and the distances between the cutoff diameter and the apex of the probes.

Varying the half-cone angle of the NSOM probe taper from 6° for the pulled probes to 15° for the etched probe can theoretically increase throughput by 4 to 5 orders of magnitude.[3, 7] While etched probes are more efficient and have higher damage thresholds, our results show that their sample heating characteristics are nearly identical to pulled NSOM probes. Results from high-resolution studies suggest that the failure mechanisms are different for the two probe geometries. For pulled NSOM probes, the thermal expansion of the aluminum coating at elevated temperatures leads to shear stresses that damage the metal shell. The shorter length over which heating occurs in etched NSOM probes allows for the input of higher laser powers which eventually lead to thermal damage of the metal coating.

4.5.4 Proposed Mechanisms Explaining Differences in Probe Failure between Etched and Pulled Probes

The unique ability to visualize light-induced NSOM probe failure as a function of power coupled light has allowed for the first direct comparison of probe failure methods of pulled and etched NSOM probes. In the case of pulled NSOM probes, the stress fracture observed in Fig. 4.7B suggests that damage to the coating arises as a result of shear stresses at elevated heating. The linear expansion of a material is described by:

$$\Delta L = \alpha L_o \Delta T \tag{4.1}$$

where ΔL represents the change in length of the material, α is the linear expansion coefficient for a given material, L_o is the original length of the material, and ΔT is the absolute change in temperature. The large difference in the linear expansion coefficients for aluminum and quartz, α=22.2 x 10^{-6} K^{-1} and α=0.59 x 10^{-6} K^{-1}, respectively, leads to a mismatch in expansion during heating. As the temperature of the probe increases, the aluminum coating expands to a greater extent than the dielectric core. As eluded to previously, the failure of pulled NSOM probes is rather clear, resulting from the differential expansion of the aluminum shell past the quartz core. This expansion causes stresses in the aluminum coating itself, which are eventually relieved by the formation of a stress fracture around the circumference of the probe as seen in Fig. 4.7B. As the adhesive forces between the aluminum and quartz are not strong enough to maintain the severed piece of the aluminum shell to the probe, the aluminum distal to the fracture is sloughed off, resulting in the exposure of bare fiber and the complete loss of a useable aperture.

For etched probes, however, the failure mechanism is not as clear. Numerous chemically etched and aluminum coated NSOM probes were visualized pre- and post-probe failure and none indicated the appearance of a clean stress fracture as demonstrated in the pulled NSOM probes, but instead resulted in probes such as those represented in Fig. 4.8. The high-resolution FIB and EM images of failed pulled and etched tips, respectively, make the results of probe failure rather clear though the mechanism is somewhat more elusive. Careful comparison of the highly magnified views of damaged pulled and etched NSOM probes in Figures 4.10A and 4.10B, respectively, may help to discern the unique mechanisms. Figures 4.10 and 4.10D represent highly magnified views of the failure regions outlined with boxes in Figs. 4.10A and 4.10B. Figure 4.10C shows the intricate network of stress fractures formed in order to relieve the shear stresses created in the pulled probes, while the lack of visible stress fractures and the presence of small islands of apparently melted aluminum on the taper of the etched probe in Fig. 4.10D suggest a mechanism involving temperatures greater than the 660 °C, the melting point of aluminum.

There are several possible theories explaining this difference. First, the expansion of the aluminum shell past the dielectric quartz core has been shown in

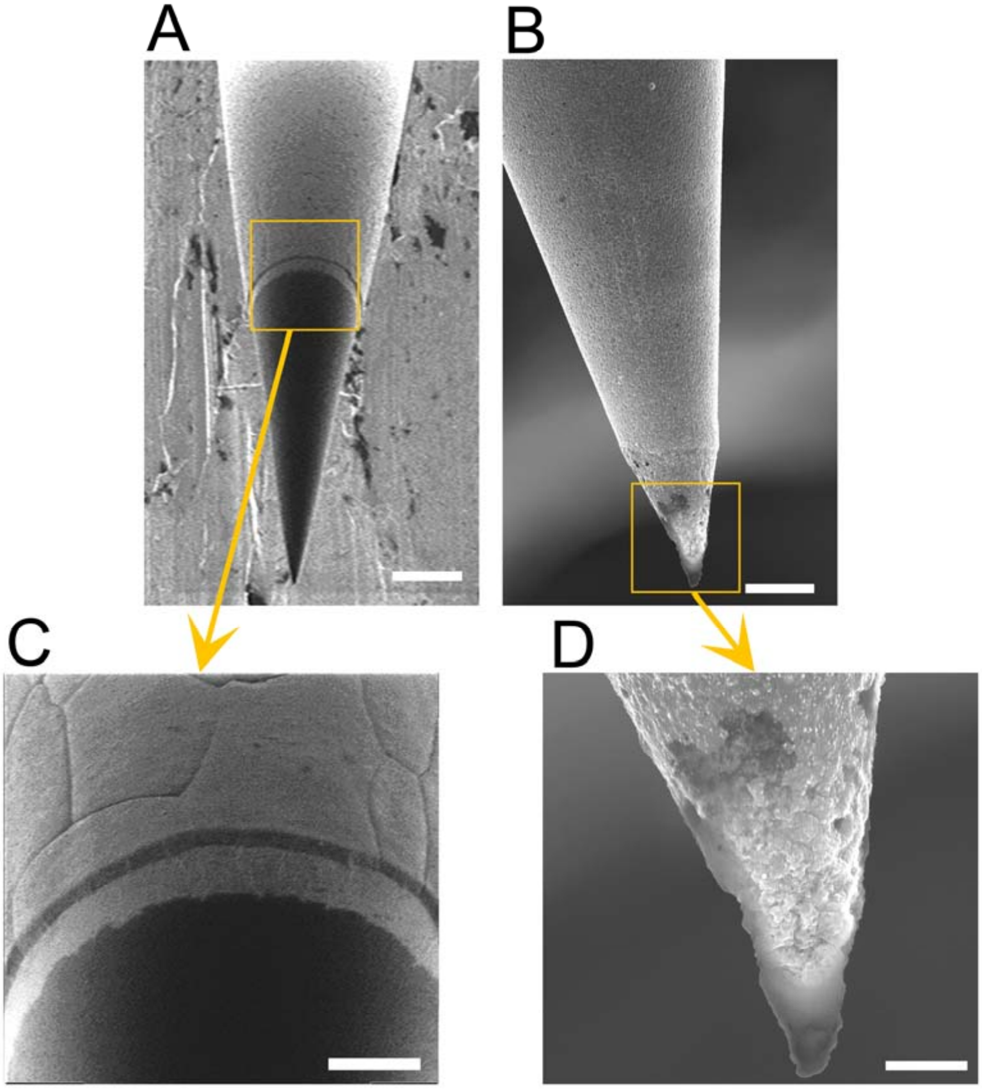

Figure 4.10 High-resolution FIB and SEM images of NSOM probes produced by heating and pulling (A) and chemical etching (B) after light-induced probe failure. The scale bars are 10 µm. The highly magnified images of the damaged aluminum coating is made more clear in (C) and (D) allowing for speculation of as to the mechanisms of failure. The scale bars are 3 µm. The presence of stress fractures in the pulled probes (A and C) indicates that failure results from the differential expansion of the aluminum shell past the quartz core as the probe is heated, while the globular islands of aluminum present on the damaged etched probes suggests that the aluminum shell may be melting.

previous studies and is believed to be responsible for the leveling off of the sample heating in the temperature versus output power curves illustrated in Figs. 4.6A and 4.6B. Equation 4.1 is used to describe the thermal expansion of a cylinder as a function of temperature, length, and material. We can estimate the relative expansion of the aluminum shell past the fiber core for both pulled and etched probes by analyzing our failure data and putting it into Eq. 4.1. Having shown that the failure of both etched and pulled probes occurs at a diameter of ~6 μm, it is assumed that this diameter represents the region in which the greatest extent of probe heating occurs, resulting in the initiation of probe failure at this point. Because of the differences in probe geometries, the average distance from this failure region to the apex is nearly four times greater for pulled probes than for etched. Now, assuming all variables in Eq. 4.1 to be the same in the case of etched versus pulled probes, with the exception of L_o, the overall expansion of the aluminum coating in pulled probes is therefore estimated to be four times greater than in the case of etched probes. Along with the greater efficiencies of etched probes, the decrease in the overall expansion and stress in the aluminum coating likely leads to the higher destruction thresholds outlined in Fig. 4.9.

Because the perylene/NA polymer utilized is only sensitive to temperatures up to ~85 °C and the 405 nm diode laser utilized in the sample heating studies lacked the output power necessary to induce probe failure, sample heating studies did not include the extreme input powers encountered just prior to probe destruction. It seems likely though that because the etched probes are able to withstand greater input powers than their pulled counterparts, etched probe temperatures may greatly exceed those in pulled probes at points just prior to their failure. Specifically, recall that temperatures as high as 470 °C have been measured 70 μm from the apex of pulled probes.[12] Given this, it is feasible to imagine temperatures along the taper reaching the 660 °C melting point of bulk aluminum with the even greater input powers allowed by etched probe designs.

A second factor likely playing a role in the mechanistic differences seen in pulled and etched probe failure arises from differences in the surfaces of the resulting quartz tapers. HF etched probes fabricated with the Turner method are extremely rough in comparison to pulled probes.[34] Surface chemistry differences, along with increased surface area, may strengthen the metal coating attachment to the fiber core of etched probes. Furthermore, the roughness of the fiber surface in etched probes requires them to be coated with greater than twice the thickness of aluminum as compared to pulled probes in order to successfully confine the excitation light.

4.6 Conclusions

Sample heating as a function of output power from NSOM probes fabricated using the chemical etching method has been characterized using a thermochromic polymer sample. At low powers, sample heating rises sharply before plateauing at approximately 55°C - 60 °C with output powers above ~50 nW - 100 nW. Interestingly, this behavior is nearly identical to heating trends measured for NSOM probes fabricating using the heating and pulling method.[24] These results indicate that only modest sample heating occurs in NSOM measurements using either pulled or etched probes. As power is increased further, probes will fail due to the loss of the metal forming the tip aperture. High-resolution measurements of NSOM probes fabricated using both approaches suggests failure occurs through different mechanisms for each. For pulled NSOM probes, differential expansion of the dielectric and metal shell at elevated powers leads to stress fractures in the metal coatings and the eventual loss of the metal around the taper of the probe. For etched probes, however, clear stress fractures are not observed and the morphology of the damaged coating suggests that melting of the aluminum may be the source of failure.

4.7 References

(1) Dunn, R. C., Near-Field Scanning Optical Microscopy. *Chem. Rev.* **1999,** 99, (10), 2891-2928.

(2) Edidin, M., Near-field scanning optical microscopy, a siren call to biology. *Traffic* **2001,** 2, (11), 797-803.

(3) Novotny, L.; Hecht, B., *Principles of Nano-Optics*. Cambridge University Press: New York, 2006; p 539.

(4) Betzig, E.; Trautman, J. K.; Harris, T. D.; Weiner, J. S.; Kostelak, R. L., Breaking the Diffraction Barrier - Optical Microscopy on a Nanometric Scale. *Science* **1991,** 251, (5000), 1468-1470.

(5) Hecht, B.; Sick, B.; Wild, U. P.; Deckert, V.; Zenobi, R.; Martin, O. J. F.; Pohl, D. W., Scanning near-field optical microscopy with aperture probes: Fundamentals and applications. *J. Chem. Phys.* **2000,** 112, (18), 7761-7774.

(6) Novotny, L.; Hafner, C., Light propagation in a cylindrical waveguide with a complex, metallic, dielectric function. *Phys. Rev. E. Stat. Phys. Plasmas Fluids Relat. Interdiscip. Topics* **1994,** 50, (5), 4094-4106.

(7) Novotny, L.; Pohl, D. W.; Hecht, B., Light confinement in scanning near-field optical microscopy. *Ultramicroscopy* **1995,** 61, (1-4), 1-9.

(8) Novotny, L.; Pohl, D. W.; Hecht, B., Scanning Near-Field Optical Probe with Ultrasmall Spot Size. *Optics Lett.* **1995,** 20, (9), 970-972.

(9) Kavaldjiev, D. I.; Toledo-Crow, R.; Vaez-Iravani, M., On the heating of the fiber tip in a near-field scanning optical microscope. *Appl. Phys. Lett.* **1995,** 67, (19), 2771-2773.

(10) Lienau, C.; Richter, A.; Elsaesser, T., Light-induced expansion of fiber tips in near-field scanning optical microscopy. *Appl. Phys. Lett.* **1996,** 69, (3), 325-327.

(11) Rosa, A. H. L.; Yakobson, B. I.; Hallen, H. D., Origins and effects of thermal processes on near-field optical probes. *Appl. Phys. Lett.* **1995,** 67, (18), 2597-2599.

(12) Stahelin, M.; Bopp, M. A.; Tarrach, G.; Meixner, A. J.; Zschokke-Granacher, I., Temperature profile of fiber tips used in scanning near-field optical microscopy. *Appl. Phys. Lett.* **1996,** 68, (19), 2603-2605.

(13) Dickenson, N. E.; Erickson, E. S.; Mooren, O. L.; Dunn, R. C., Characterization of power induced heating and damage in fiber optic probes for near-field scanning optical microscopy. *Rev. Sci. Instrum.* **2007,** 78, (5).

(14) Stockle, R. M.; Schaller, N.; Deckert, V.; Fokas, C.; Zenobi, R., Brighter near-field optical probes by means of improving the optical destruction threshold. *J. Microsc.* **1999,** 194, (Pt 2-3), 378-82.

(15) Yakobson, B. I.; LaRosa, A.; Hallen, H. D.; Paesler, M. A., Thermal/optical effects in NSOM probes. *Ultramicroscopy* **1995,** 61, (1-4), 179-185.

(16) Hoffmann, P.; Dutoit, B.; Salathe, R.-P., Comparison of mechanically drawn and protection layer chemically etched optical fiber tips. *Ultramicroscopy* **1995,** 61, (1-4), 165-170.

(17) Zeisel, D.; Dutoit, B.; Deckert, V.; Roth, T.; Zenobi, R., Optical Spectroscopy and Laser Desorption on a Nanometer Scale. *Anal. Chem.* **1997,** 69, (4), 749-754.

(18) Lazarev, A.; Fang, N.; Luo, Q.; Zhang, X., Formation of fine near-field scanning optical microscopy tips. Part I. By static and dynamic chemical etching. *Rev. Sci. Instrum.* **2003,** 74, (8), 3679-3683.

(19) Burgos, P.; Lu, Z.; Ianoul, A.; Hnatovsky, C.; Viriot, M. L.; Johnston, L. J.; Taylor, R. S., Near-field scanning optical microscopy probes: a comparison of pulled and double-etched bent NSOM probes for fluorescence imaging of biological samples. *J. Microsc.* **2003,** 211, (1), 37-47.

(20) Moar, P.; Ladouceur, F.; Cahill, L., Numerical analysis of the transmission efficiency of heat-drawn and chemically etched scanning near-field optical microscopes. *Appl. Optics* **2000,** 39, (12), 1966-1972.

(21) Betzig, R. E., Nondestructive Optical Imaging of Surfaces with 500 Angstrom Resolution Ph.D. Thesis, Cornell University, Ithica, New York, August 1988.

(22) Pohl, D. W., Some thoughts about scanning probe microscopy, micromechanics, and storage. *IBM J. Res. Dev.* **1995,** 39, (6), 701-711.

(23) Kurpas, V.; Libenson, M.; Martsinovsky, G., Laser heating of near-field tips. *Ultramicroscopy* **1995,** 61, (1-4), 187-190.

(24) Erickson, E. S.; Dunn, R. C., Sample heating in near-field scanning optical microscopy. *Appl. Phys. Lett.* **2005,** 87, (20), 201102.

(25) Thiery, L.; Marini, N., Thermal behaviour modelling of tapered optical fibres for scanning near-field microscopy. *Ultramicroscopy* **2003,** 94, (1), 49-69.

(26) Thiery, L.; Marini, N.; Prenel, J.-P.; Spajer, M.; Bainier, C.; Courjon, D., Temperature profile measurements of near-field optical microscopy fiber tips by means of sub-micronic thermocouple. *Int. J. Therm. Sci.* **2000,** 39, (4), 519-525.

(27) Heinzelmann, H.; Huser, T.; Lacoste, T.; Guntherodt, H. J.; Pohl, D. W.; Hecht, B.; Novotny, L.; Martin, O. J. F.; Hafner, C. V.; Baggenstos, H.; Wild, U. P.; Renn, A., Scanning Near-Field Optical Microscopy in Basel, Ruschlikon, and Zurich. *Opt. Eng.* **1995,** 34, (8), 2441-2454.

(28) Novotny, L.; Pohl, D. W.; Regli, P., Light-Propagation through Nanometer-Sized Structures-The 2-Dimensional-Aperture Scanning Near-Field Optical Microscope. *Journal of the Optical Society of America a-Optics Image Science and Vision* **1994,** 11, (6), 1768-1779.

(29) Gucciardi, P. G.; Colocci, M.; Labardi, M.; Allegrini, M., Thermal-expansion effects in near-field optical microscopy fiber probes induced by laser light absorption. *Appl. Phys. Lett.* **1999,** 75, (21), 3408-3410.

(30) Latini, G.; Downes, A.; Fenwick, O.; Ambrosio, A.; Allegrini, M.; Daniel, C.; Silva, C.; Gucciardi, P. G.; Patane, S.; Daik, R.; Feast, W. J.; Cacialli, F., Optical probing of sample heating in scanning near-field experiments with apertured probes. *Appl. Phys. Lett.* **2005,** 86, (1), 011102-3.

(31) Latini, G.; Downes, A.; Fenwick, O.; Ambrosio, A.; Allegrini, M.; Gucciardi, P. G.; Patane, S.; Daniel, C.; Silva, C.; Daik, R.; Feast, W. J.; Cacialli, F., Investigation of heating effects in near-field experiments with luminescent organic semiconductors. *Synth. Metals* **2004,** 147, (1-3), 165-169.

(32) Chandrasekharan, N.; Kelly, L. A., A dual fluorescence temperature sensor based on perylene/exciplex interconversion. *J. Am. Chem. Soc.* **2001,** 123, (40), 9898-9.

(33) Turner, D. R. U.S. Patent No. 4,469,554, 1984.

(34) Stockle, R.; Fokas, C.; Deckert, V.; Zenobi, R.; Sick, B.; Hecht, B.; Wild, U. P., High-quality near-field optical probes by tube etching. *Appl. Phys. Lett.* **1999,** 75, (2), 160-162.

Chapter 5

High-Resolution Near-Field Scanning Optical Microscopy Studies of Vaults and Nuclear Pore Complexes.

5.1 Introduction

Nuclear pore complexes were reviewed in depth in Chapter 1 in which many details about their structure and functional roles are outlined. Most of this structural information to date has been attained through high-resolution imaging techniques such as EM and AFM.[1-11] AFM has proven particularly useful as it is capable of imaging the nuclear membrane in the absence of contrast agents and under benign conditions. Specifically, AFM was instrumental in understanding NPC structural changes following treatments known to alter cisternal calcium levels. In these studies, the depletion of calcium through IP_3 receptor activation was found to result in the apparent simultaneous displacement of the central mass toward both the nuclear and cytoplasmic rings.[4, 6, 11] From these observations, we hypothesized that the central mass in not moving within the pore, but rather the nuclear and cytoplasmic rings collapse towards one another as a function of release of cisternal calcium. This mechanism accounts for the apparent displacement of the central mass towards both faces of the NPC as well as the simultaneous widening of the pore resulting from the necessary rearrangement of the nucleoporins to accommodate this structural change.[12, 13] The presence and proposed Ca^{2+} sensitivity of the trans-membrane nucleoporin gp210, discussed in Chapter 1, led to the speculation that it may play a role as a specific calcium sensor within the cisternal region of the NE.[14, 15]

The exact mechanism by which gp210 could induce these conformational changes is unclear, although immunoblocking through the expression of a monoclonal antibody against gp210 resulted in dramatically reduced cyto-nuclear transport in cultured cells.[16] This indicates that it is essential in the transport function of NPCs and together with previous data suggests that it may do so through inducing calcium-dependent conformational changes within the pores themselves, although currently there is no direct evidence to support this.

Links between the central mass and cisternal calcium levels have led to much speculation as to the identity of this enigmatic structure and although there is much debate, numerous studies indicate that it most likely represents cargo transiting the pore.[8, 17] Chapter 2 outlines several studies undertaken in an effort to specifically identify transiting vault ribonucleoprotein particles as the central mass. Similarities in the size and shape of vault proteins to the central mass as well as studies implicating vaults in cyto-nuclear transport have led to speculation that the central mass may represent vaults transiting NPCs.[18-21] In an effort to investigate this relationship directly, Förster resonance energy transfer (FRET) was utilized as a means of identifying interactions between NPCs and the large vault ribonucleoproteins. By labeling vaults and NPCs with a FRET dye pair, significant energy transfer was measured on *Xenopus* nuclear envelopes, suggesting a specific interaction. Furthermore, depletion of cisternal calcium from within the nuclear envelope resulted in a systematic increase in energy transfer efficiency, which is in good agreeance with the previous AFM data outlining the spatial relationship between the central mass within the pore.[4, 6, 11]

The FRET studies outlined above and detailed in Chapter 2 provide compelling evidence that vault proteins and NPCs are colocalized at the nuclear envelope. The calcium dependence of the energy transfer suggests a specific interaction between vaults and NPCs that is sensitive to changes in cisternal calcium levels. Although this could be the direct result of vaults representing the plugs located within the lumen of NPCs, other mechanisms cannot be ruled out from these studies. For example, the changes in energy transfer could result from an interaction between NPCs and vaults located at the periphery of the pore rather than within. In this case, the calcium-dependent changes in pore diameter could result in changes in FRET efficiencies. Though FRET measurements are extremely sensitive to nanometric changes in interaction, they lack the ability to directly reveal the absolute location of vaults with respect to nuclear pores and for this reason, are unable to rule out these possibilities.

In order to directly investigate the location of vaults with respect to NPCs, the small dimensions of the pores require that a high-resolution technique must be utilized. Traditionally, high-resolution studies of nuclear pores have been achieved through techniques such as transmission electron microscopy (TEM) and AFM, but unfortunately both prove problematic for directly locating vaults to NPCs. AFM has the resolution necessary to accurately resolve NPCs and to locate small structures such as vaults at the nuclear envelope, but the technique's inherent lack of sample specificity does not allow for the identification of small structures such as vaults. For example, Fig. 5.1 shows an AFM image of a 1 μm^2 area of NPCs on an isolated *X. laevis* nuclear envelope. The location of NPCs is clear as their distinct toroidal morphology is evident in the image. However, note that there are numerous small structures throughout the scan that are approximately the same size as vault particles (arrows). Some of these structures reside within the NPCs as the central mass while others are located on the membrane peripheral to the nuclear pores. The lack of distinct morphological differences among these particles does not allow for AFM to identify the structures. In other words, AFM is not able to determine if or where vaults are located at the NE, only that particles with vault-like size and shape reside there. The necessary specificity can be achieved by immunolabeling the vaults in order to locate them at the membrane. High-resolution TEM studies, such as those discussed in Chapter 2, have been used to colocalize gold immunolabeled vaults to NPCs,[18, 19] although the use of large immunogold labels likely increases the degree of non-specific interactions and has led to some concerns.

Because of the specificity inherent to immunolabeling and the non-perturbative nature of optical techniques, direct observation of vaults and NPCs through fluorescence detection is desirable. Unfortunately, as discussed in Chapter 3, traditional optical techniques are resolution-limited to approximately $\lambda/2$, or ~250 nm when working within the visible spectrum.[22-24] The impact of this limited resolution

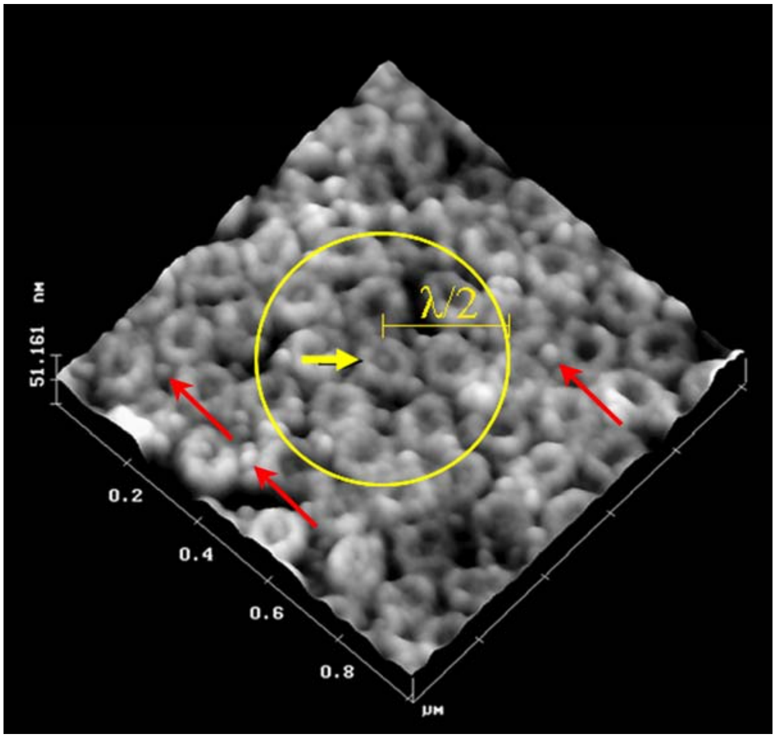

Figure 5.1 A 1µm x 1µm AFM scan of nuclear pores illustrating their size relative to the limit of optical diffraction. The yellow circle overlaid onto the image has a radius of 250 nm. This represents the Rayleigh limit of resolution for visible excitation radiation with a wavelength of 500 nm. The impact of the resolution limit is that fluorescent labels within the circle cannot be resolved from one located at the central NPC, indicated by a yellow arrow. The image also identifies several structures with similar size and shape to the vaults peripheral to the NPCs (Red arrows).

is shown in Fig. 5.1. The circle overlaid onto the AFM image of NPCs has a radius of 250 nm which represents the Rayleigh limit of resolution for excitation radiation with a wavelength of 500 nm. As defined by the Rayleigh criterion, a fluorophore located at the central pore (indicated by yellow arrow) can therefore not be resolved from any other fluorescent marker within the circle. This lack of resolution makes direct correlations between vaults and NPCs on a pore-by-pore basis extremely difficult. Alternatively, the high-resolution force and fluorescence detection capabilities of NSOM, outlined in Chapter 3, as well as the studies in Chapter 4 indicating minimal heat transfer from near-field probes to the sample make NSOM an ideal technique for directly observing interactions between vaults and NPCs.

5.2 Experimental

5.2.1 SDS-PAGE and Western Blot Utilizing a Monoclonal Antibody against the Major Vault Protein

Mouse anti-human MVP monoclonal antibody, clone: 1014 (Labvision, Fremont, CA) was characterized for use in *X. laevis* systems by western blot analysis. Stage VI oocytes were harvested from mature *Xenopus laevis* (*Xenopus* express, Homosassa, FL) as detailed in Chapter 2. The oocytes were immediately placed in a freshly prepared, protease inhibitor containing, modified mock internal buffer consisting of 10 mM HEPES (Sigma Aldrich, St. Louis, MO), 1.4 mM $MgCl_2$, 140 mM KCl (Fisher Chemical, Fair Lawn, NJ), 10 μM Leupeptin, 10 μM Pepstatin A, and 100 μM Phenylmethanesulfonyl fluoride (PMSF) (Sigma-Aldrich, St. Louis, MO) and adjusted to pH 7.2 with $NaHCO_3$.

The cytoplasm from approximately one oocyte was transferred to a 0.5 mL eppendorf tube and centrifuged into a pellet. The supernatant was replaced with 15 μl of fresh lysis buffer containing 50 mM Tris-HCL, 1 mM EDTA, 1 mM β-mercaptoethanol (Sigma-Aldrich, St. Louis, MO), 1% triton X-100 (Sigma-Aldrich, St. Louis, MO), 0.1% sodium dodecyl sulfate (SDS), 10 μM Leupeptin, 10 μM Pepstatin A, and 100 μM PMSF. The samples were diluted with a fresh protein dilution solution (PDS) containing 2% SDS, 100 mM dithiothreitol (DTT) (Bio-Rad, Hercules, CA), 60 mM Tris-HCl, 10% glycerol, 0.01% bromophenol blue (Sigma-Aldrich, St. Louis, MO), and 0.5% β-mercaptoethanol. The solution was adjusted to pH 6.8

All samples were placed in a 95˚C water bath for 5 minutes and 5 μL of each sample were loaded onto a 4% stacking, 7.5% resolving vertical polyacrylamide Tris-HCl gel (Bio-Rad, Hercules, CA). Lanes in the gel included cytoplasmic extract and an unstained high molecular weight SDS-PAGE standard (Bio-Rad, Hercules, CA). The protein was transferred to an immune-blot polyvinylidene fluoride (PVDF) membrane (Bio-Rad, Hercules, CA), dried, and fixed with 7.5% acetic acid for 15 minutes on an orbital shaker. The membrane was stained with SYPRO Ruby (Molecular Probes, Carlsbad, CA) for 15 minutes and imaged on a Typhoon Trio imaging system. The membrane was then blocked for 1 hour in 5% dry skimmed milk, and floated on a 1 μg/ml mAb1014:TTBS solution for 2 hours prior to subsequent exposure to 1:3000 Alexa 633 goat anti-rabbit (Molecular Probes, Carlsbad, CA):TTBS solution for 1 hour. After drying, the membranes were imaged again on the Typhoon Trio imaging system in order to visualize antibody-binding specificity.

5.2.2 Preparation of Nuclear Membranes for Analysis

The membranes were prepared for analysis as in Chapter 2. Stage VI oocytes were harvested from mature *Xenopus laevis* (*Xenopus* express, Homosassa, FL). The oocytes were immediately placed in a freshly prepared, protease inhibitor containing, modified mock internal buffer described above. Nuclei were manually removed from the oocyte utilizing a dissecting microscope and fine-point forceps. The cytoplasmic debris was removed from the nuclei via repeated gentle pipetting through a glass Pasteur pipette. The removal of the nuclei from the whole oocytes was accomplished on custom made Teflon-bottom dishes in an effort to prevent unwanted attachment of the nuclei. The cleaned nuclei were then transferred to another set of Teflon-bottom dishes where they were allowed to incubate for 20 minutes in a pH 7.3 Ca^{2+} free mock buffer comprised of 10mM HEPES, 90 mM KCl, 10 mM NaCl, 2 mM $MgCl_2$, and 1.1 mM EGTA (Fisher Chemical, Fair Lawn, NJ). The nuclei then chemically fixed through exposure to 5% paraformaldehyde in TBS for 20 minutes. The chemically fixed nuclei were transferred to 25 mm x 25mm #1.5 coverglass (Fisher Scientific, Fair Lawn, NJ) where the nuclear envelopes were manually lysed with 125 μm diameter glass fiber that had been heated and pulled to a fine point, allowing for the removal of the nuclear contents. Specifically, the membranes were laid flat, cytoplasmic side up, the surrounding solution was removed, and the nuclei were allowed to air dry. Once dry and adhered to the substrate, the nuclei were gently rinsed with ultrapure water (18 MΩ) and subsequently labeled for detection of membrane bound vault complexes. The dried membranes were covered with 1% bovine serum albumin (BSA) in TBS for 1 hour to block nonspecific binding of antibodies. The BSA solution was removed and replaced with a 20 µg/ml solution of mAb 1014 in 0.5% BSA/TBS for 4 hours at room temperature. The primary antibody solution was removed and the membranes were gently rinsed three times with TBS. The nuclei were then covered with an Alexa 647 conjugated goat anti-mouse secondary antibody in 0.5% BSA/TBS solution for 4 hours at room temperature. In the cases when NPCs were fluorescently visualized, they were exposed to a 0.1 µg Alexa 488 wheat germ agluttinin (WGA) (Invitrogen, Carlsbad, Ca) solution in addition to the fluorescently conjugated secondary antibody after a time point of 3.5 hours, giving a total exposure time of 30 min for the WGA. The labeling solutions were then removed and the samples thoroughly rinsed with ultrapure water to ensure that no salt crystals formed. The membranes were allowed to air dry and were subsequently imaged.

5.2.3 Far-Field Fluorescence Detection of Vaults and NPCs

The labeling densities and distributions of vaults and NPCs on isolated *X. laevis* nuclear envelopes were visualized with an Olympus IX71 inverted microscope.

The 488 nm and 568 nm laser lines from a Kr/Ar mixed gas laser (Coherent Innovent 70 Spectrum, Santa Clara, CA) were coupled into the scope in order to visualize the vault and NPC labels. The fluorescence was collected through a 60X 1.45 NA objective and directed through appropriate emission filters onto a cooled electron multiplying CCD camera (Photometrics Cascade 650, Tucson, AZ). An overlay of the fluorescence images depicting vault and NPC locations within the NE was achieved with Slidebook software (Intelligent Imaging Innovations, Inc, Denver, CO).

5.2.4 Near-Field Instrumental Setup

The NSOM instrument utilized for these studies was described in previous chapters. Briefly, the instrument is built on a Zeiss Axiovert 135TV inverted microscope. A Nanoscope IIIa controller and Digital Instruments Nanoscope software are utilized to monitor feedback and maintain the desired tip-sample gap. The probe is held within a homebuilt head which is responsible for induction and monitoring of the lateral probe oscillation necessary for shear-force feedback and also includes a piezo tube which controls the precise z-position of the probe. The sample is scanned beneath the probe by a Mad City Labs closed loop x-y piezoelectric scanner. The appropriate excitation laser line is coupled into the distal end of the fiber probe and the fluorescence emission radiating from the sample is collected through a 60X 1.45 NA oil objective and focused onto an avalanche photodiode (APD) detector after passing through an appropriate set of emission filters.

All of the probes used in these experiments were produced by heating and pulling single mode fiber optic (Nufern, East Granby, CT) with a Sutter P-2000 micropipette puller. Precise control of the parameters of the micropipette puller allows for the creation of probes with various distinct geometries. The probes for these experiments were intentionally made to have exceptionally long tapers and small cone angles such as the one shown in Fig. 3.7C. Though this drastically decreases the probe throughput efficiencies, this geometry has been shown to reduce the aperture size of the probe, thus increasing resolution.[23, 25] The pulled fibers were then introduced into a vacuum chamber in which they were held at an angle of 35° from parallel and rotated on their axis as ~50-100 nm of aluminum was evaporated onto the tapered regions of the fibers. This confines the excitation light within the fiber and forms the necessary aperture at the apex of the probe.

5.3 Results and Discussion

5.3.1 Verifying Vault Antibody Specificity in X. laevis

The specificity of mAb 1014, a commercially available monoclonal antibody raised against human MVP, was characterized for use with *X. laevis* oocytes as it had not been previously utilized in this system. Figure 5.2 is a western blot illustrating the efficiency and specificity of mAb 1014 for *X. laevis* MVP. Lane *a* represents a total protein stain of the soluble protein within a *X. laevis* oocyte and lane *b* is the resulting western blot in which a single band at ~100 kDa verifies the recognition of *Xenopus* MVP by mAb 1014.

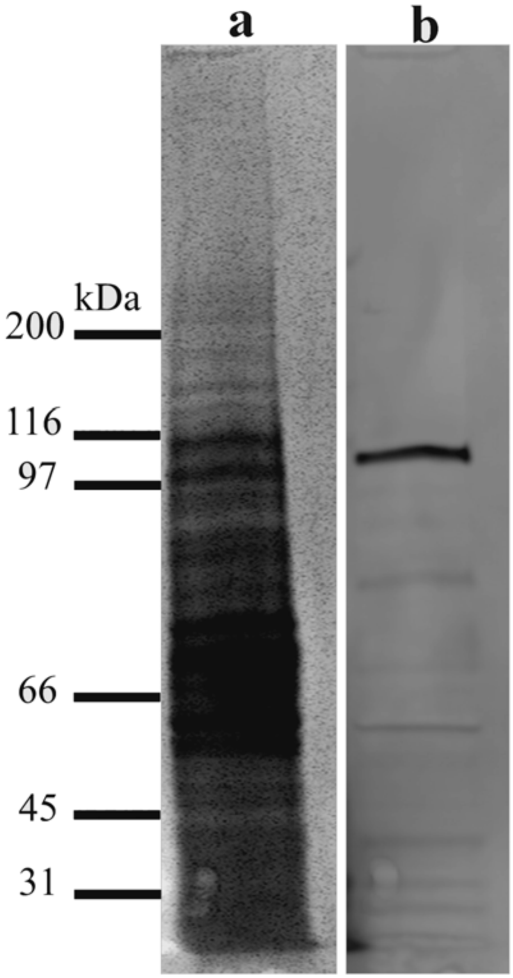

Figure 5.2 Western blot analysis showing specificity of the mAb 1014 monoclonal antibody toward *Xenopus laevis* MVP. Lane *b* represents the cytoplasmic extract from *Xenopus* oocytes probed with the mAb 1014 antibody, revealing a single band at ~100 kDa, the expected molecular weight of MVP. Lane a represents the total protein stain from the oocyte sample prior to incubation with the antibody. *a* and *b* represent the same lane of protein blotted from an SDS gel with *b* resulting from the removal of the Sypro protein stain and the detection of MVP with mAb 1014.

5.3.2 Colocalization of Vaults with Nuclear Pore Complexes

Figure 5.3 is a series of far-field fluorescence images taken of isolated *X. laevis* nuclear membranes. Figure 5.3A shows the distribution of NPCs as labeled with an Alexa 488 conjugated lectin (WGA). Figure 5.3B outlines the location of vault proteins at the nuclear envelope as labeled with mAb 1014 and an Alexa 647 conjugated goat anti-mouse secondary. Controls in which the membranes were imaged in the absence of fluorescent labels and those resulting from incubation with fluorescent secondary antibodies only resulted in no significant labeling, confirming the fluorescence seen in Fig. 5.3A and 5.3B is specific for NPCs and vaults, respectively. Figure 5.3C is the overlay of the two images. The strong fluorescence signal in the vault channel (Fig. 5.3B) indicates that vaults are located at the nuclear envelope and the overlay in 5.3C should allow for a direct correlation of vault and NPC location. Unfortunately, the inability to optically resolve individual NPCs precludes this correlation as the unresolved individual fluorescent markers in the NPC channel (5.3A) result in a strong background on the membrane rather than a punctuate distribution of fluorescence locating individual pores. Again, the fluorescence resulting from the location of antibodies specific for MVP (Fig. 5.3B) confirms that vaults are located at the nuclear envelope, although the technique's lack of resolution does not allow for the precise mapping of vault location relative to NPCs. In order to directly visualize the location of vaults relative to nuclear pores, the specificity of immunolabeling and the high-resolution force and fluorescence capabilities of NSOM were utilized. By simultaneously mapping the location of NPCs in the force image

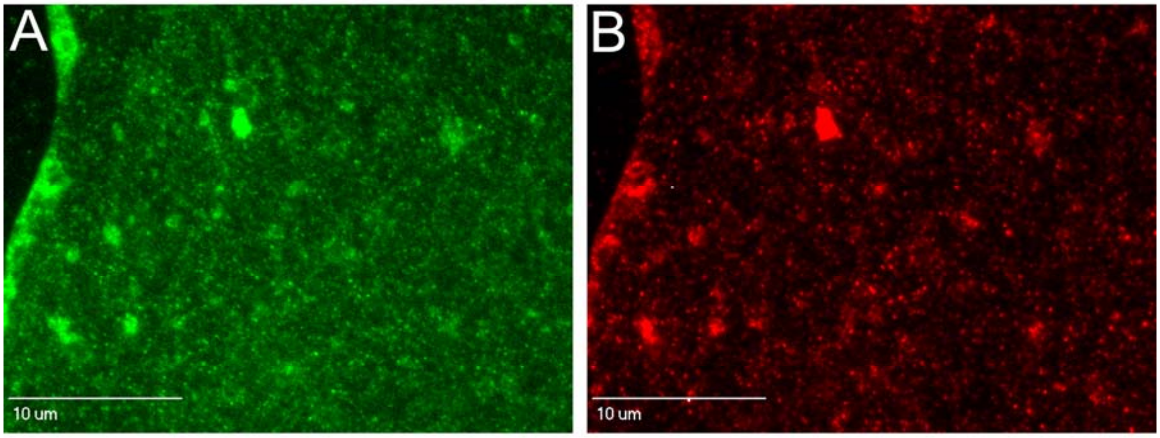

NPCs

Vaults

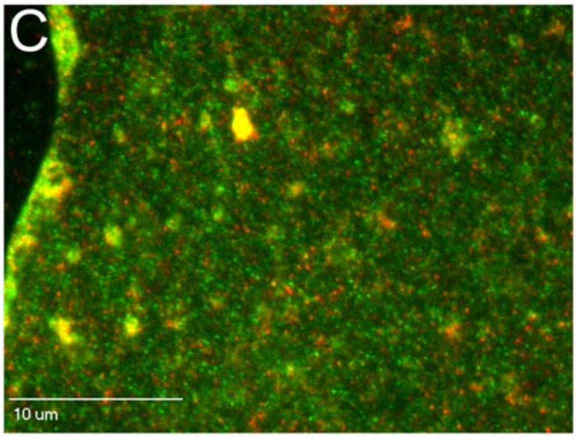

Overlay

Figure 5.3 Far-field fluorescence images mapping the location and distribution of NPCs (A) and vaults (B). The overlay of the two (C) illustrates the difficulty in directly visualizing the location of vaults with respect to nuclear pores. Though the technique is capable of detecting fluorescence from single fluorophores, many NPCs do not appear as single fluorescent points, but rather as an unresolved signal resulting from the fluorescence of several neighboring pores. The scale bars are 10 μm.

and the location of fluorescently labeled vaults in the fluorescence channel, a direct comparison of the two can be achieved, allowing for the discrimination of vaults and other small membrane structures.

Figure 5.4 shows representative 10 μm x 10 μm NSOM images of a *X. laevis* nuclear envelope in which the NPC locations are apparent in the force image (A) and the location of the vault complexes are revealed in the high-resolution fluorescence channel (B). Again, because the two channels are collected simultaneously by the same probe, the resulting overlay of the two channels (Fig. 5.4C) allows for the direct visualization of the colocalization/interaction of vaults and NPCs on a pore-by-pore basis. Specifically, the overlay in Fig. 5.4C illustrates a striking colocalization between the NPCs in the force image and fluorescently labeled vaults. Furthermore, we find that vaults not only locate to NPCs, but in the regions of the membrane excluding nuclear pores, the corresponding region in the fluorescence channel lacks vault signal. This indicates that vaults not only interact with pores, but that they do so specifically, avoiding regions of bare membrane. Therefore, the small bumps between NPCs seen in AFM images are not likely vaults at the membrane, but rather other membrane-associated proteins such as ribosomes.

In order to further characterize the interactions between vaults and nuclear pores, isolated *X. laevis* nuclear envelopes were visualized by 2-color NSOM in which the location of both vaults and NPCs were monitored in the high-resolution fluorescence channel. This can be beneficial when directly comparing the location of

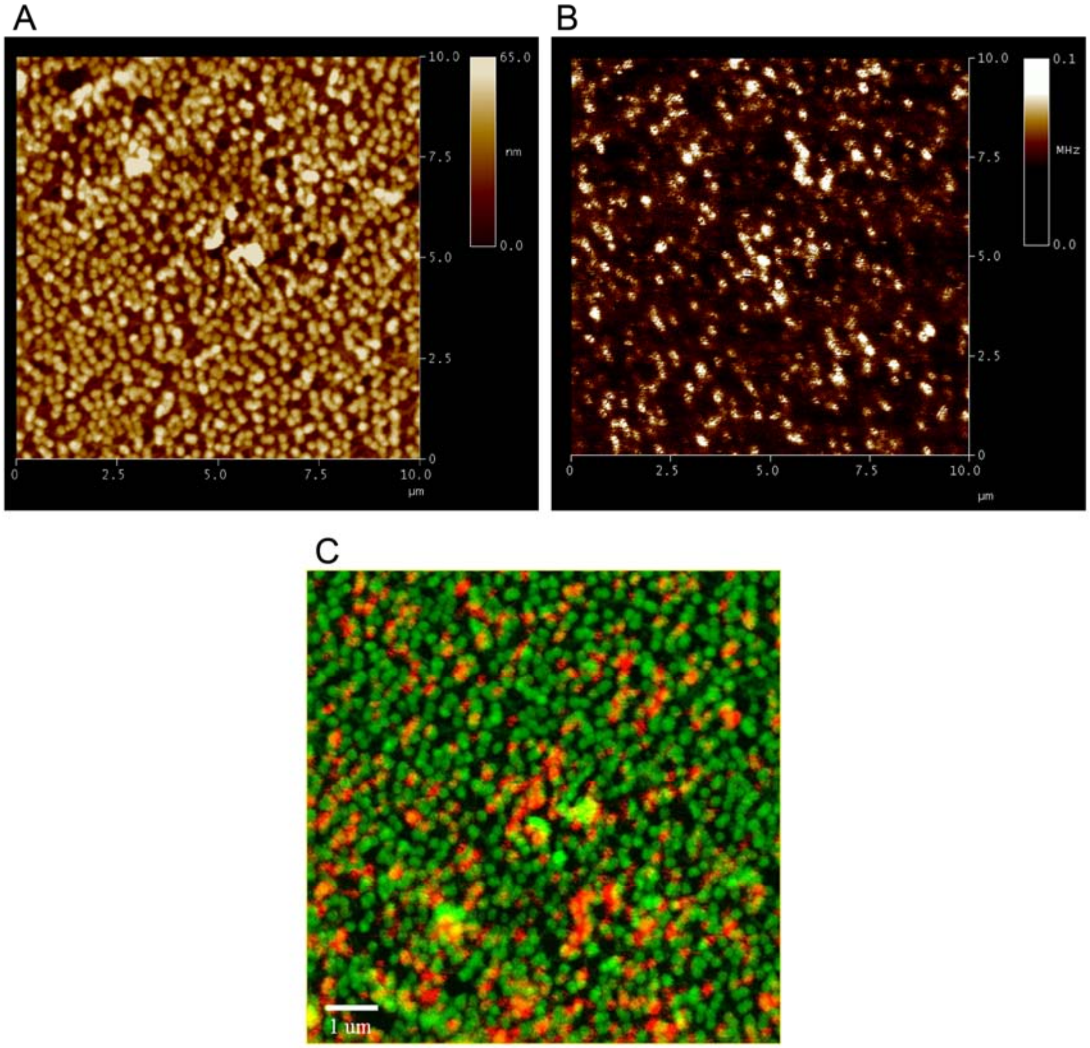

Figure 5.4 Simultaneously collected force (A) and fluorescence (B) NSOM images of a 10 µm x 10 µm region of nuclear membrane in which vaults have been fluorescently labeled. The NPCs are identified in the force image (A) and the vaults are simultaneously located in the high-resolution fluorescence channel (B). The overlay of the two (C) demonstrates a significant colocalization between vaults (Red) and NPCs (Green). The high-resolution capabilities of NSOM allow for the investigation of interaction on a pore-by-pore basis. The scale bar is 1 µm.

proteins to one another as the collection of the same data type (fluorescence) allows for a more direct comparison of the images. Figure 5.5 shows representative NSOM images of a region of isolated membrane in which the NPCs have been fluorescently labeled with WGA-Alexa 488 (Fig. 5.5A) and the vaults have again been labeled with mAb 1014 and an Alexa 647 secondary antibody (Fig. 5.5B). As mentioned, because the location of NPCs and vaults are both detected in the fluorescence channel, free from chromatic aberrations introduced by focusing elements, we can directly correlate the two images on a pixel-by-pixel basis. Comparing the two images qualitatively, we again see that the high-resolution, punctate fluorescence signal locating vaults (Fig. 5.5B) corresponds to regions of the membrane also exhibiting labeling from NPCs (Fig. 5.5A). In order to more precisely map the colocalization of vaults and NPCs, a fluorescence correlation plot was constructed and is shown in Fig. 5.6. The plot is created by mapping the intensity of each pixel in both channels against one another. The intensity of a given pixel in the vault channel corresponds to the X axis value of the scatter plot and the intensity of the same pixel in the NPC channel determines the coordinate value on the Y axis. Control experiments confirmed that the use of the two spectrally separated fluorophores, Alexa 488 and Alexa 647, along with appropriate emission filter sets reduces bleed-through from one channel to the other which would result in false positives in the correlation maps.

The fluorescence correlation map shown in Fig. 5.6 supports the assignment of direct interactions between vaults and NPCs which was visually apparent in Fig. 5.4. The linear region in the plot indicates that as the intensity in any given pixel in

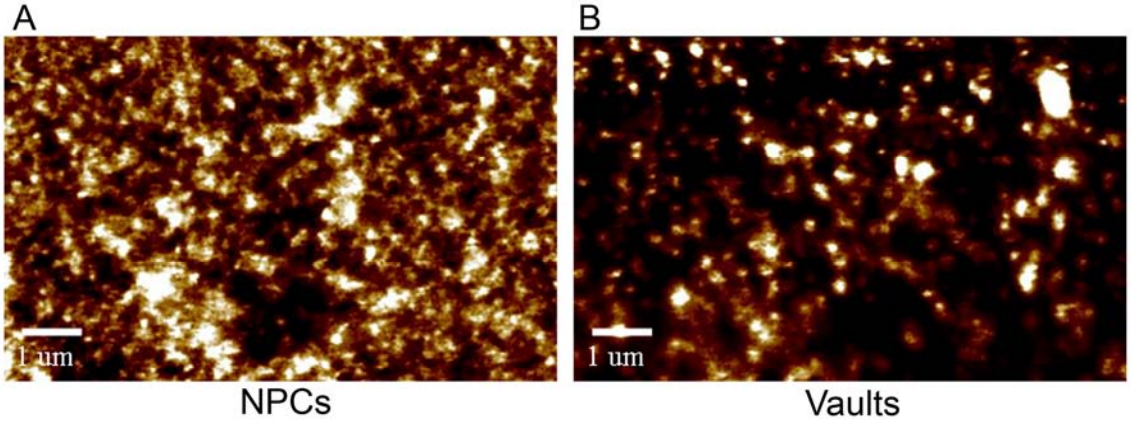

Figure 5.5 2-color NSOM images of NPCs (A) and vaults (B). The collection of spectrally separated high-resolution fluorescence mapping the location of both NPCs and vaults on a nuclear envelope allows for a direct comparison of the two images.

the vault channel is high, the intensity in the NPC channel is likely to be high as well, resulting from their direct spatial correlation. The clustered region of points located at the left of the plot indicates that in the absence of signal in the vault channel, detecting signal from an NPC is random. Again, this confirms what we see directly in Fig. 5.4 where the majority of vaults are located to pores, but not all pores contain a vault. These results are in good agreement with the previous FRET studies in Chapter 2 indicating that vaults are specifically located at NPCs within the nuclear envelope and helped to rule out FRET interactions occurring between NPCs and vaults located on the nuclear envelope rather than specifically at nuclear pores.

5.4 Conclusions and Future Directions

The collection of high-resolution force and fluorescence data on isolated *X. laevis* nuclear membranes allowed for a direct pore-by-pore visualization of colocalization/interaction between vaults and NPCs. This correlation was strikingly apparent when the location of pores in the force channel was directly compared to the location of labeled vaults in the fluorescence channel (Fig. 5.4). By using a fluorescent WGA construct in lieu of the force image to probe the location of NPCs, 2-color NSOM was able to directly correlate the spectrally separated fluorescence channels marking the location of vaults and NPCs (Fig. 5.5). Directly comparing the fluorescent distribution in two channels allowed for the creation of correlation plots. (Fig. 5.6). The linearity found in the high-intensity regions of the plot indicate that the majority of vaults are correlated to NPCs, while the lack of a defined pattern in

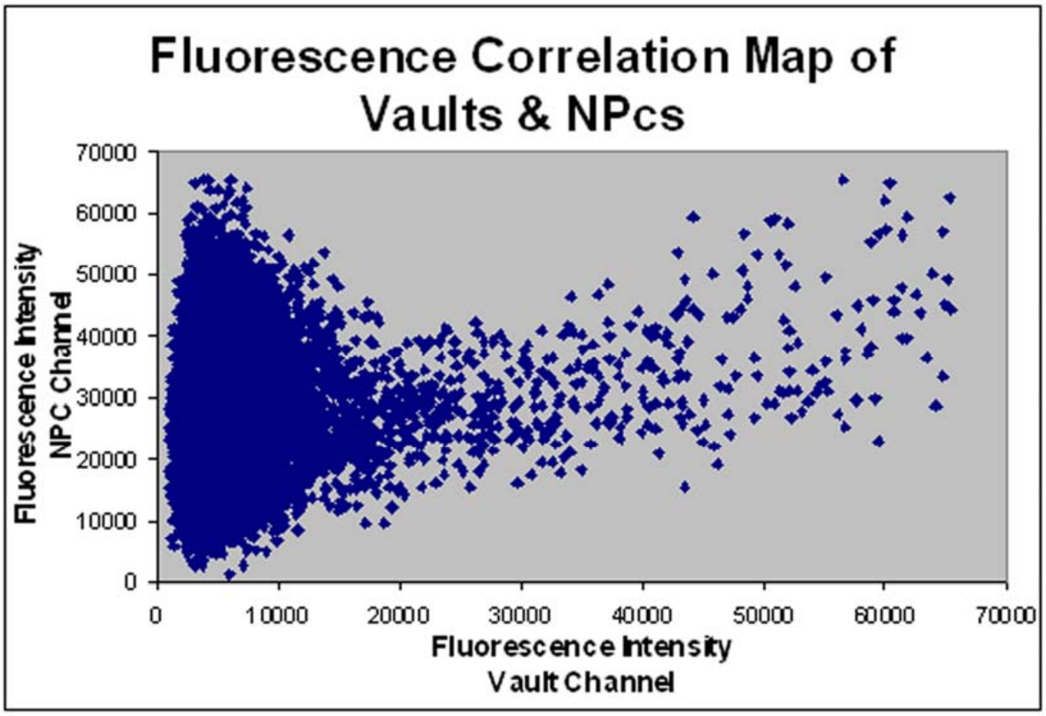

Figure 5.6 Fluorescence correlation map comparing the NSOM images locating NPCs and vaults. Each data point in the plot represents a corresponding pair of pixels in the NSOM images. The fluorescence intensity of a given pixel in the vault image is measured along the X coordinate while the corresponding pixel in the NPC image measured along the Y coordinate. The linear region of data points verifies the correlation between the location of vaults and NPCs. The non-linearity of the data points located at the left of the plot indicates that in regions of the membrane lacking a vault, the presence of a NPC is neither correlated nor anti-correlated. Together, this indicates that vaults interact specifically with NPCs, but that many nuclear pores do not contain vaults.

the low-intensity regions indicates that neither the presence not absence of NPCs is correlated to regions lacking vaults.

This interpretation of is in good agreeance with FRET and EM data in Chapter 2, as well as the direct visualization of this interaction afforded by the simultaneous collection of high-resolution force and fluorescence near-field data (Fig. 5.4). Several studies have shown that vaults are able to act as cellular transport vessels and that they are capable of residing within the nuclei of some cells.[20] This implies that they are capable of crossing the NE and since NPCs represent the only direct passageway to do so, vaults must be specifically interacting with NPCs at some point. Similarities in size and shape to EM constructs, the calcium dependent FRET efficiencies discussed in Chapter 2, and the high-resolution correlations afforded by NSOM further suggest that the NPC central mass may be a transiting vault protein.

5.4.1 Future Directions

At first glance, the NSOM fluorescence locating labeled NPCs (Fig. 5.5B) appears to have lower resolution than the previous scan locating immunolabeled vaults (Fig. 5.5A). However, measuring the full width at half maximum (FWHM) of the smallest features in both images results in similar values of ~75 nm, indicating that the variations between the images are not related to the tip or the feedback mechanism. Rather, the differences in feature size results from the labeling technique implemented. In Fig. 5.5A, the FG repeats in the nuclear pores were labeled with a fluorescently conjugated lectin (WGA) rather than with the use of an antibody against specific nucleoporins within the NPC. WGA has been used extensively in studies where the location of either the nuclear envelope or nuclear pores needed to be outlined.[26, 27] The popularity of this NPC label results from its high affinity for the numerous FG domains located within the channel of the pore as well as those found at the periphery. This leads to a strong, but diffuse fluorescence signal that is generated from sites all around the pore, resulting in labeling as seen in Fig. 5.3A by far-field collection and in Fig. 5.5A by high-resolution NSOM. The use of an antibody, such as mAb 414, which was used in the FRET studies in Chapter 2 as a label for NPCs, would allow for less diffuse labeling of NPCs. However, because the mAb 1014 antibody raised against vault MVP and mAb 414 raised against NPCs are both mouse-raised monoclonal antibodies, difficulties in differentially labeling the two proteins arose.

Future studies utilizing NSOM to investigate the interactions between vaults and NPCs could be improved by extending the work above to include simultaneous 2-color NSOM of antibody-labeled NPCs and vaults. The concurrent use of two monoclonal antibodies could be achieved by directly conjugating spectrally distinct fluorophores to the respective antibodies, eliminating the need for specific secondary antibody recognition. This labeling scheme would provide a more precise location of NPCs as compared to the use of WGA, while maintaining the specificity of mAb 1014 for MVP.

The simultaneous collection of emission from both NPC and vault labels will also allow for a direct pixel-by-pixel comparison of their distribution. Due to difficulties in introducing multiple excitation lines into a NSOM probe and the simultaneous collection of spectrally separated emission by two APDs, the 2-color studies outlined in this chapter resulted from concurrent scans in which the excitation lines and emission filters were switched between scans.

5.5 References

(1) Akey, C. W., Interactions and structure of the nuclear pore complex revealed by cryo-electron microscopy. *J. Cell Biol.* **1989,** 109, (3), 955-70.

(2) Akey, C. W.; Radermacher, M., Architecture of the Xenopus nuclear pore complex revealed by three-dimensional cryo-electron microscopy. *J. Cell Biol.* **1993,** 122, (1), 1-19.

(3) Beck, M.; Lucic, V.; Forster, F.; Baumeister, W.; Medalia, O., Snapshots of nuclear pore complexes in action captured by cryo-electron tomography. *Nature* **2007,** 449, (7162), 611-5.

(4) Erickson, E. S.; Mooren, O. L.; Moore-Nichols, D.; Dunn, R. C., Activation of ryanodine receptors in the nuclear envelope alters the conformation of the nuclear pore complex. *Biophys. Chem.* **2004,** 112, (1), 1-7.

(5) Fahrenkrog, B.; Stoffler, D.; Aebi, U., Nuclear pore complex architecture and functional dynamics. *Curr. Top. Microbiol. Immunol.* **2001,** 259, 95-117.

(6) Moore-Nichols, D.; Arnott, A.; Dunn, R. C., Regulation of nuclear pore complex conformation by IP(3) receptor activation. *Biophys. J.* **2002,** 83, (3), 1421-8.

(7) Pante, N.; Aebi, U., Toward the molecular details of the nuclear pore complex. *J. Struct. Biol.* **1994,** 113, (3), 179-89.

(8) Stoffler, D.; Feja, B.; Fahrenkrog, B.; Walz, J.; Typke, D.; Aebi, U., Cryo-electron tomography provides novel insights into nuclear pore architecture: implications for nucleocytoplasmic transport. *J. Mol. Biol.* **2003,** 328, (1), 119-30.

(9) Wang, H.; Clapham, D. E., Conformational changes of the in situ nuclear pore complex. *Biophys. J.* **1999,** 77, (1), 241-7.

(10) Yang, Q.; Rout, M. P.; Akey, C. W., Three-dimensional architecture of the isolated yeast nuclear pore complex: functional and evolutionary implications. *Mol. Cell* **1998,** 1, (2), 223-34.

(11) Mooren, O. L.; Erickson, E. S.; Moore-Nichols, D.; Dunn, R. C., Nuclear side conformational changes in the nuclear pore complex following calcium release from the nuclear membrane. *Phys. Biol.* **2004,** 1, 125-134.

(12) Erickson, E. S.; Mooren, O. L.; Moore, D.; Krogmeier, J. R.; Dunn, R. C., The role of nuclear envelope calcium in modifying nuclear pore complex structure. *Can. J. Physiol. Pharm.* **2006,** 84, (3-4), 309-318.

(13) Mooren, O. L.; Erickson, E. S.; Dickenson, N. E.; Dunn, R. C., Extending Near-Field Scanning Optical Microscopy for Biological Studies. *JALA* **2006,** 11, (4), 268-272.

(14) Greber, U. F.; Gerace, L., Depletion of calcium from the lumen of endoplasmic reticulum reversibly inhibits passive diffusion and signal-mediated transport into the nucleus. *J. Cell Biol.* **1995,** 128, (1-2), 5-14.

(15) Greber, U. F.; Senior, A.; Gerace, L., A major glycoprotein of the nuclear pore complex is a membrane-spanning polypeptide with a large lumenal domain and a small cytoplasmic tail. *Embo. J.* **1990,** 9, (5), 1495-502.

(16) Greber, U. F.; Gerace, L., Nuclear protein import is inhibited by an antibody to a lumenal epitope of a nuclear pore complex glycoprotein. *J. Cell Biol.* **1992,** 116, (1), 15-30.

(17) Danker, T.; Oberleithner, H., Nuclear pore function viewed with atomic force microscopy. *Pflugers Arch.* **2000,** 439, (6), 671-81.

(18) Chugani, D. C.; Rome, L. H.; Kedersha, N. L., Evidence that vault ribonucleoprotein particles localize to the nuclear pore complex. *J. Cell. Sci.* **1993,** 106 (Pt 1), 23-9.

(19) Dickenson, N. E.; Moore, D.; Suprenant, K. A.; Dunn, R. C., Vault ribonucleoprotein particles and the central mass of the nuclear pore complex. *Photochem. Photobiol.* **2007,** 83, (3), 686-691.

(20) Slesina, M.; Inman, E. M.; Rome, L. H.; Volknandt, W., Nuclear localization of the major vault protein in U373 cells. *Cell Tissue Res.* **2005,** 321, (1), 97-104.

(21) van Zon, A.; Mossink, M. H.; Houtsmuller, A. B.; Schoester, M.; Scheffer, G. L.; Scheper, R. J.; Sonneveld, P.; Wiemer, E. A., Vault mobility depends in part on microtubules and vaults can be recruited to the nuclear envelope. *Exp. Cell Res.* **2006,** 312, (3), 245-55.

(22) Dunn, R. C., Near-Field Scanning Optical Microscopy. *Chem. Rev.* **1999,** 99, (10), 2891-2928.

(23) Novotny, L.; Hecht, B., *Principles of Nano-Optics*. Cambridge University Press: New York, 2006; p 539.

(24) Pohl, D. W., Some thoughts about scanning probe microscopy, micromechanics, and storage. *IBM J. Res. Dev.* **1995,** 39, (6), 701-711.

(25) Novotny, L.; Pohl, D. W.; Regli, P., Light-Propagation through Nanometer-Sized Structures-The 2-Dimensional-Aperture Scanning Near-Field Optical Microscope. *Journal of the Optical Society of America a-Optics Image Science and Vision* **1994,** 11, (6), 1768-1779.

(26) Finlay, D. R.; Newmeyer, D. D.; Price, T. M.; Forbes, D. J., Inhibition of Invitro Nuclear Transport by a Lectin That Binds to Nuclear-Pores. *J. Cell Biol.* **1987,** 104, (2), 189-200.

(27) Miller, M.; Park, M. K.; Hanover, J. A., Nuclear-Pore Complex - Structure, Function, and Regulation. *Physiol. Rev.* **1991,** 71, (3), 909-949.

Chapter 6

Single-Molecule Transport Measurements through NPCs

6.1 Introduction

The works outlined in the previous chapters of this thesis focused on probing the structural aspects and specific protein interactions of the nuclear pore complex. Specifically, Chapter 2 discusses a series of sensitive energy transfer measurement studies which found that the interaction and spatial relationship between vault complexes and NPCs were highly dependent on cisternal calcium levels. This dependence is in good agreement with AFM studies having previously shown the relative location of the unidentified central mass within NPCs to also depend on cisternal calcium levels.[1-3] Chapter 5 outlines a study in which the high-resolution imaging capabilities of NSOM were exploited to directly visualize vault proteins at nuclear pores. These and many other techniques such as atomic force microscopy and electron microscopy have proven useful in mapping out the physical architecture of the pore and probing interactions with cellular components.[4-8] However, the static nature of these studies essentially provides snapshots of NPCs in time. In order to investigate the NPC dynamics of transport directly, other techniques have to be employed.

6.1.1 Bulk Measurements of Nuclear Transport

As reviewed in Chapter 1, passage through the nuclear pore complex occurs via distinct pathways. Small molecules are allowed to passively diffuse across the NE as a function of concentration gradients.[9-11] Transport of molecules larger than ~40 kDa however, is energy dependent and requires the involvement of a number of chaperone proteins, and the cargo must contain a conserved peptide sequence targeting the molecule to the appropriate chaperone.[11, 12] Much of the early understanding of nuclear transport resulted from the *in situ* monitoring of bulk movement of fluorescent cargo into cell nuclei.[9, 10] For example, Breeuwer and Goldfarb demonstrated that the microinjection of several small fluorescently conjugated nonnuclear proteins ranging from 14.4 kDa – 21 kDa resulted in a rapid and significant accumulation of fluorescence within the cell nuclei.[13] Neither cooling the cells to 4 °C nor energy depletion through drug treatment affected the distribution of these molecules, suggesting that their transport relies on simple concentration gradient driven diffusion. The microinjection of large, 158 kDa, fluorescent dextrans, however, resulted in a homogeneous distribution throughout the cytoplasm and exclusion from the nucleus under all conditions, confirming that there is a size limit for molecules passively transiting NPCs. This is in stark contrast with previous results investigating the cellular distribution of large proteins containing nuclear localization sequences. In this case, both cooling the cells and drug mediated energy depletion caused reversible elimination of nuclear transport, outlining the differences between active transport and passive diffusion across NPCs.[14]

Studies such as those outlined above have proven instrumental in delineating the differences between active and passive transport and identifying the cellular factors involved in regulating them (Chapter 1, Fig. 1.2). Quantification of nuclear import as a function of time has allowed these studies to be extended in an effort to probe the specific rates at which cargo transits NPCs. In one example, Ribbeck and Görlich were able to monitor the facilitated transport of fluorescently conjugated nuclear transport factor 2 (NTF2).[15] NTF2 is an essential transport component which mediates the cyto-nuclear trafficking of Ran-GDP in order to maintain the necessary energy gradient across the nuclear envelope (NE). The authors were able estimate the frequency of fluorescent NTF2 transport events through NPCs by calibrating the fluorescence intensity of NTF2 to concentration, estimating the number of NPCs per nucleus, and monitoring nuclear fluorescence as a function of time. For NTF2, a transport frequency of ~2500 NTF2 homodimers NPC^{-1} s^{-1} was estimated, although the accuracy of this rate is limited by the ability to determine the number of NPCs per nucleus. However, these studies also found that the frequency of non signal-mediated diffusion of the similarly sized green fluorescent protein (GFP) was ~120 times less than that of NTF2.[15] Despite the uncertainties in estimating the number of NPCs per nucleus, this comparison illustrates the importance and efficiency of facilitated transport. Additionally, the observed frequency of the GFP translocation is ~4 times slower than that predicted for a molecule of its size to transit an empty channel in the NPC. This has been attributed to interactions within the pore in which the FG domains slow down, but do not inhibit passively diffusing molecules, while actively transported cargo requires the presence of the proper karyopherins to navigate the pore.

6.1.2 *Transport Studies of Individual NPCs*

Because the studies outlined above relied on average fluorescence flux into a nucleus containing ~2800 NPCs, it is impossible to discern single transport events that would reveal insight into the specific mechanism of transport. Rather, the results represent ensemble averaged events over a large area and number of pores. Traditionally, transport through individual membrane channels is monitored with a patch clamp technique in which electrical current through a physically and electrically isolated patch of membrane is monitored.[16] This has proven extremely successful in studying membrane bound ion channels, although extending it to study NPCs has proven difficult due to the physical size of NPCs. Peters and co-workers were able to circumvent this by implementing a fluorescence microscopic method which they named optical single transporter recording (OSTR).[17]

Briefly, OSTR involves sealing an isolated nuclear membrane onto an isoporous filter and covering the membrane with a fluorescent transport solution. The filter pore diameter can be varied, but those with pore diameters of 180 nm were used in an effort to obtain an average of one NPC per filter cavity. Monitoring of the accumulation of fluorescently labeled dextrans within the cavities below the membrane as a function of time allows for the calculation of diffusional frequencies at individual NPCs. As expected, the frequencies of calculated events were found to be inversely proportional to the size of the diffusing cargo with rate constants for 4 kDa, 10 kDa, and 20 kDa dextrans being 0.053, 0.020, and 0.008 dextrans NPC^{-1} s^{-1}, respectively.[17] By comparing the experimental rate constants and their distribution to computationally derived histograms, the authors concluded that the NPC contains only one channel through which passive diffusion can occur while further calculations determined that the dimensions of the channel are ~10 nm in diameter and ~45 nm long.

Active transport was similarly investigated using large ~130 kDa proteins expressed with GFP and a NLS or NES.[18] The transport rates for these signal-mediated proteins were significantly higher than those found previously for the passive diffusion of small dextrans, confirming the importance and efficiency of facilitated transport across the NE. Specifically, facilitated import and export of the expressed proteins were found to be 2 molecules NPC^{-1} s^{-1} and 4 molecules NPC^{-1} s^{-1}, respectively.[18] Furthermore, it was found that the import proteins containing a NLS were only transported from the cytoplasmic to nuclear sides of the membrane, export proteins containing a NES only moved from the nuclear to cytoplasmic regions, and control proteins containing neither were unable to cross the NE under any conditions, thus validating the OSTR method. The significant differences in the transport rates of ~2500 NPC^{-1} s^{-1}determined in the previous bulk studies of NTF2 and the OSTR results finding a nuclear transport frequency of 2 NPC^{-1} s^{-1} are somewhat unclear. However, differences in concentration gradients, transported cargoes utilized, and sample conditions makes comparisons problematic.

6.1.3 Single-Molecule Dwell Time Analysis

The studies outlined above provided some of the first insights into transport at individual nuclear pores, although they still relied on the extrapolation of event frequencies from fluorescence intensities. With recent advancements in cooled charged coupled devices (CCD), especially electron multiplication and on chip amplification, it has become possible to record fluorescence images at rates exceeding 500 Hz with great efficiency. Kubitscheck and co-workers were some of the first to take advantage of this technology to measure single-molecule dwell times of fluorescent molecules actively transported across the nuclear envelope in live permeabilized cells.[19] Histograms of interaction times between transiting fluorescent cargo and NPCs expressing a GFP-POM 121 nucleoporin were created. The average dwell times were calculated by fitting the frequency of events to an exponential decay function. This resulted in dwell times of 5.8 ± 0.2 ms and 7.2 ± 0.25 ms for NFT2 and transportin, respectively. Interestingly, the same study found that the cargo-bound forms of these karyopherins transited NPCs more rapidly than the unbound forms, which was accounted for by what the authors referred to as a “shielding effect” in which the bound cargo shields the karyopherins from the FG domains within the pore allowing for more rapid transport.[19]

Further analysis of the single-molecule transport times led to yet another interesting insight. Assuming a single transport channel, a molecule such as NTF2, exhibiting a 5.8 ± 0.2 ms dwell time, should have a maximum kinetic rate of ~170 molecules NPC^{-1} s^{-1}.[19] This is significantly less than the rate of ~2500 molecules

NPC^{-1} s^{-1} measured in permeabilized cells by Ribbeck and Görlich[15] and the rate of ~1500 molecules NPC^{-1} s^{-1} that Siebrasse and Peters found in isolated *X. laevis* oocyte nuclei,[20] suggesting that multiple parallel pathways for active transport exist in each pore.

Other studies have utilized similar single-molecule techniques to investigate non signal-mediated transport through NPCs. Specifically, the investigation of passive diffusion of small molecules (10 kDa dextrans and the S13 subunit of the small ribosomal subunit) found dwell times of 2.2 ± 0.1 ms and 3.3 ± 0.1 ms, respectively.[21] Interestingly, the addition of the karyopherin importin β was found to decrease the dwell times to a point such that they were no longer measureable (<0.5 ms). Because importin β does not interact directly with non signal-mediated cargo, it has been hypothesized that instead it interacts with the FG network within the NPCs increasing their fluidity and decreasing opposition to passage of even small molecules.[21]

Dynamic studies of NPC transport have led to the identification of differences between active and passive transport across the nuclear envelope and an understanding of processes involved in signal-mediated transport. Recently the ability to probe single-molecule transport events at individual pores has opened many doors for the study of NPC transport including calculation and comparison of NPC dwell times and transport efficiencies.[18, 21, 22]

Although these studies have been extremely informative, they have also proven to be difficult and time consuming. Because single-molecule transport studies require the ability to identify and analyze individual transport events, the background within the system has to be sufficiently low to allow for the identification and tracking of individual fluorescent particles. Alternatively, single-molecule studies also require that the number of events recorded is large in order to statistically represent the population. Here, we introduce a novel method for monitoring single-molecule transport events at individual nuclear pores in isolated *X. laevis* oocyte nuclear membranes. By utilizing the shallow excitation field afforded by total internal reflection (TIR) to monitor diffusion of fluorescent dextrans out of an isolated nucleus, individual transport events through NPCs are specifically recorded while background fluorescence is practically eliminated. This allows for the use of nuclei containing a high concentration of dextrans, affording hundreds of transport events per analysis, thus resulting in a selective and efficient process for monitoring single-molecule transport as a function of various conditions.

6.2 Total Internal Reflectance Fluorescence Microscopy (TIRF-M)

Total internal reflectance fluorescence microscopy (TIRF-M) is a technique which allows for the selective visualization of fluorescent molecules near a sample interface through the use of an evanescent excitation field. The principles of TIRF are based upon the refraction of light as an interface. As light passes through an interface, moving from high refractive index to low, it is refracted away from the normal as described by Snell's law which states:

$$n_1 \sin(\theta_1) = n_2 \sin(\theta_2) \qquad (6.1)$$

where n_1 is the refractive index of the substrate such as a glass coverslip (n_{glass} = 1.52), n_2 is the refractive index of the next medium which is generally air or a buffered solution (n_{air} = 1.00, n_{water} = 1.33). θ_1 defines the incident angle of the light and θ_2 is the angle of the refracted light measured from the sample normal. Total internal reflection (TIR) occurs when $\theta_2 \geq 90°$, resulting in all of the excitation light being reflected back into the substrate with no refracted light entering the sample. However, this produces a non-propagating, exponentially decaying, evanescent field which extends ~150 nm - 200 nm into the sample. Utilizing this evanescent field as an excitation source results in a dramatic reduction of background fluorescence and allows for an increased signal-to-noise for molecules near the interface, as those beyond the narrow evanescent field are not excited. As outlined by Eq. 6.1, the conditions under which TIR can occur are based upon the refractive indices of the substrate and sample as well as the incident angle of light. Rearranging Eq. 6.1 and setting $\theta_2 = 90°$ results in the equation:

$$\theta_{critical} = \sin^{-1}\left(\frac{n_2}{n_1}\right) \tag{6.2}$$

where $\theta_{critical}$ is the critical angle (incident angle at which TIR occurs) and n_1 and n_2 are the refractive indices of the substrate and sample as defined above.

Historically, prisms have been used to introduce excitation light externally from the collection objective in order to obtain the high incident angles necessary to induce TIR. Recently, however, the introduction of high numerical aperture (NA) objectives has allowed for the routine implementation of TIRF-M, as the large focal volumes of objectives with an NA ≥ 1.40 are able to support the high incident angle necessary to initiate TIR, thus eliminating the need for an external prism.

Coupling TIRF-M with a strong excitation source and a sensitive CCD detector exhibiting a fast refresh rate allows for the detection of single-molecule fluorescence with high time resolution. Specifically, in the case of single-molecule transport studies, the shallow excitation field introduced by TIRF selectively monitors transport events through individual NPCs located near the sample interface. This allows for the use of nuclei containing high concentrations of dye and high-intensity excitation sources without limitations due to a strong background signal. Together, these advantages result in the selective and efficient collection of single-molecule transport events which can be studied under varying biological conditions. The details of the experimental design and setup will be further discussed in the experimental section.

6.3 Experimental

6.3.1 Preparation of Isolated X. laevis Oocyte Nuclei

Stage VI oocytes were harvested from mature *Xenopus laevis* (*Xenopus* express, Homosassa, FL) as detailed in Chapter 2. The oocytes were immediately placed in a freshly prepared, protease inhibitor containing, modified mock internal buffer containing 10 mM HEPES (Sigma Aldrich, St. Louis, MO), 1.4 mM $MgCl_2$, 140 mM KCl (Fisher Chemical, Fair Lawn, NJ), 10 μM Leupeptin, 10 μM Pepstatin A, and 100 μM Phenylmethanesulfonyl fluoride (PMSF) (Sigma-Aldrich, St. Louis, MO) and adjusted to pH 7.2 with $NaHCO_3$. Nuclei were manually removed from the oocyte utilizing a dissecting microscope and fine-point forceps. The cytoplasmic debris was removed from the nuclei via repeated gentle pipetting through a glass Pasteur pipette. The dissection of the nuclei from the oocytes was accomplished on custom made Teflon-bottom dishes in an effort to prevent unwanted attachment of the nuclei. The cleaned nuclei were then transferred to separate Teflon-bottom dishes containing appropriate dextran solutions in order to pre-load them. Texas Red conjugates of 10 kDa, 40kDa, and 70 kDa dextrans (Invitrogen, Carlsbad, CA) were all utilized at 15 nM concentrations in the modified mock buffer described above. 1.5% by weight polyvinylpyrrolidone (PVP) (Calbiochem, San Diego, CA) was added to the dextran solutions in order to prevent osmotic swelling of the nuclei. After the appropriate incubation time, nuclei were removed from the dextran solution, gently rinsed three times in modified mock buffer containing PVP, and immediately imaged. In the case of nuclei which have been treated with wheat germ agglutinin (WGA) (Biomeda Corp., Foster City, CA), the pre-loaded and rinsed nuclei were exposed to the appropriate concentrations of WGA in the modified mock-PVP solutions and were imaged at indicated timepoints.

6.3.2 Cell Culture and Microinjection

Freshly split human arterial smooth muscle (HASM) cells (American Type Cell Culture, Manassas, VA) were cultured in Dulbecco's modified Eagle medium (DME-M) (Sigm-Aldrich, St. Louis, MO) supplemented with 10% fetal bovine serum

(Hyclone, Logan, UT), 100 U/ml penicillin, and 100 μg/ml streptomycin (Mediatech, Manassas, VA) and grown on #1.5 glass coverslips at 37 °C and 5% CO_2. For studies in which transport cargo was introduced into the cells via microinjection, microinjection pipettes with ~5 μm diameter openings were fabricated by heating and pulling 1.5 mm O.D. 0.86 mm I.D. borosilicate glass capillaries with a Sutter P2000 micropipette puller (Sutter Instrument, Novato, CA). The pipettes were backfilled with the injection solution consisting of the fluorescent transport molecules in transport buffer (20 mM HEPES, 1mM EGTA, 110 mM KOAc, 5 mM NaOAc, 2 mM MgOAc (Sigma Chemical Company, St. Louis, MO) pH 7.3) supplemented with 1 μg/ml of each of the following protease inhibitors: Pepstatin A, Leupeptin, and phenyl methyl sulfonyl fluoride (Sigm-Aldrich, St. Louis, MO). The microinjected cells were maintained at 37 °C in a modified mock buffer throughout the microinjection and imaging processes with the use of a stage heater and temperature controller (Heatwave, Dagan Corp., Minneapolis, MN).

6.3.3 Detection of Single-Molecule Translocation

6.3.3a Passive Transport

For the study of passive diffusion of Texas Red conjugated dextrans through isolated *X. laevis* nuclei, the pre-loaded nuclei were placed into a 35 mm dish with a #1.5 coverglass bottom (MatTek, Ashland, MA) containing modified mock buffer. The nuclei were gently pressed and held at the surface of the coverslip utilizing a custom apparatus consisting of a 3-axis micromanipulator and a Pasteur pipette which had the end sealed and flattened by heat. The fluorescent dextrans were visualized by excitation with the 568 nm line of a Kr-Ar mixed gas laser (Coherent Innovent 70 Spectrum, Santa Clara, CA). Molecules at the interface were specifically targeted with the use of TIRF-M to selectively excite fluorophores within ~200 nm of the surface and to reduce background signal. The fluorescence was collected through a 100X 1.45 N.A. objective and focused onto a cooled, electron multiplied CCD (Photometrics Cascade 128+, Tucson, AZ) at a collection rate of 200 Hz – 500 Hz.

6.3.3b Active Transport

The active transport of either bovine serum albumin (BSA) conjugated with a NLS and Rhodamine dye (Sigma-Aldrich, St. Louis, MO) or the more photostable allophycocyanin labeled with a NLS was observed after microinjection into a live HASM cell. The APC-NLS conjugate was prepared by Elizabeth Erickson and is detailed elsewhere.[23] The fluorophores were excited by the 568 nm and 647 nm lines of a Kr/Ar mixed gas laser, respectively. The emission was collected through a 60X 1.45 N.A. objective and focused onto a cooled, electron multiplied CCD (Photometrics Cascade 650, Tucson, AZ).

6.3.4 Measurement of Single-Molecule Dwell Times

Single-molecule dwell times for dextrans passively diffusing through NPCs in isolated *X. laevis* nuclei were measured with the use of Slidebook software (Intelligent Imaging Innovations, Inc, Denver, CO) and analyzed with AxoGraph

(Molecular Devices, Sunnyvale, CA) software. Because of the shallow excitation field produced by TIRF, only fluorescent events at the nuclear envelope were recorded and manually selected in Slidebook (version 4.2.0.3). Intensity versus time data for each event was imported and plotted in AxoGraph X in order to determine the dwell times of individual transiting dextrans. This was done by identifying fluorescent events with amplitudes of ≥5 times the calculated background noise and measuring their full-width-at-half-maximum (FWHM) values. Histograms of the resulting dwell times were then fit to an exponential decay function in order to determine the transport lifetimes.

6.4 Results and Discussion

NPCs have the ability to support both active and passive transport mechanisms which are determined by a number of factors including size, shape, and primary structure.[24] Much about these transport mechanisms has been elicited, although the precise interactions and mechanisms of transport within NPCs remain unclear. As discussed in Chapter 1, there are currently several mechanisms proposed which attempt to describe both facilitated transport and passive diffusion through NPCs.[15, 25-28] These mechanisms were primarily based on studies observing effects on bulk transport, while it has not been until recent years that dynamic single-molecule transport information has come to light.[9, 19, 21, 22] Advancements in technology have allowed for the detection of single fluorescent particles transiting the nuclear envelope through NPCs. By monitoring dwell times between NPCs and fluorescent cargo as a function of ATP, karyopherin concentration, and cargo size, studies have led to insights into the mechanisms of cyto-nuclear transport which were previously hidden in bulk ensemble measurements. This set of experiments is aimed at further eliciting the nature of selective permeability exhibited by NPCs and the mechanisms by which cargo is transported across the nuclear envelope.

6.4.1 Diffusion Times of Individual Cargo through NPCs in X. laevis Oocytes

Though many factors such as the size, charge, and secondary structure are important, it is well understood that generally small molecules (≤ 40 – 60 kDa) are allowed to diffuse through NPCs while larger molecules require a more complicated energy-dependent mechanism.[29] Several studies have suggested, however, that passive transport may not be as simple as diffusion through a hollow channel within the NPC.[7, 21, 30] This was specifically demonstrated by Yang and Musser who showed that the dwell times of 10 kDa dextrans at NPCs were drastically decreased by the addition of importin β, an import karyopherin. Because importin β does not specifically interact with non signal-mediated transport molecules, these studies suggest that the importin β disrupts the FG network lining the pore, facilitating passage of even small molecules through the NPC.[21] In order to investigate this more directly, we chose to monitor dwell times of various small dextrans as a function of FG domain availability.

Isolated *X. laevis* nuclei were incubated in solutions of either 10 kDa or 70 kDa fluorescent dextrans in order to ensure that the isolation procedure did not rupture the nuclei. Figure 6.1 shows two nuclei which have been exposed to Texas Red conjugated 10 kDa (Fig. 6.1A) or 70 kDa (Fig. 6.1B) dextran solutions for ~1 hour prior to imaging. While the nucleus bathed in a solution with the 10 kDa dextrans appears bright throughout it’s volume, the one incubated in the 70 kDa dextran solution shows primarily peripheral staining as the large dextrans are known to be unable to transit NPCs. This confirms that careful isolation of nuclei from oocytes does not physically damage the membrane itself and that dextrans crossing the NE must pass through NPCs. Similar studies of 40 kDa dextran solutions indicated that they are also able to diffuse into the nuclei, providing another fluorescent probe for studies of diffusion through NPCs.

Direct observation of the transport of both 10 kDa and 40 kDa Texas Red dextrans were observed by placing the pre-loaded nuclei into a clean solution of modified mock buffer and allowing them to settle onto the surface of #1.5 glass bottom dishes. By exciting the fluorescent dextrans with TIRF, only the fluorophores exiting the NE located at the glass interface were excited and visualized. As the nuclei themselves are not perfect spheres, but rather contain numerous folds and invaginations extending beyond the reach of the generated evanescent field, only small areas of the nucleus were able to be observed with TIRF-M, limiting the number of visible transport events. This was overcome with the use of a custom made manipulator. Briefly, a glass Pasteur pipette with a flat sealed surface was produced by melting and molding the glass with a Bunsen burner. The pipette was held with a 3-axis micromanipulator and lowered to the top of the nucleus. Gentle

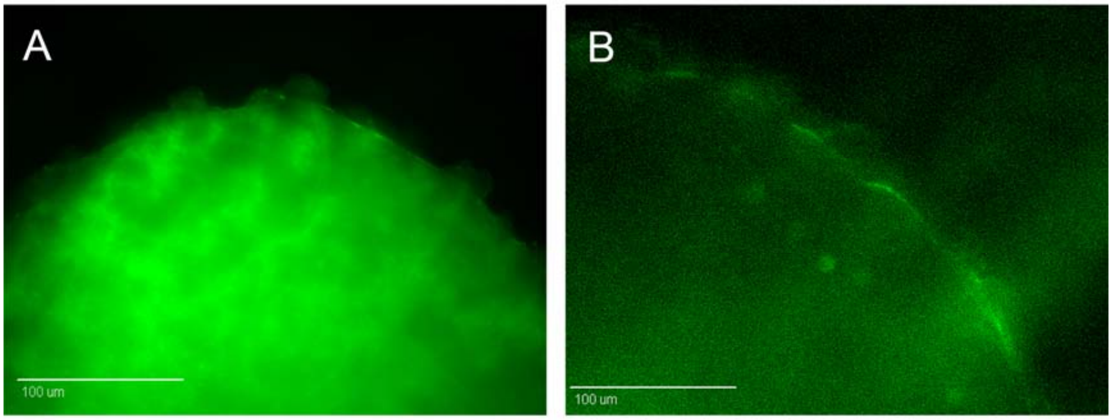

Figure 6.1 Fluorescence images of isolated *Xenopus* oocyte nuclei incubated in (A) 10 kDa Texas Red dextrans and (B) 70 kDa Texas Red dextrans. The 10 kDa dextrans passively diffuse through the nuclear envelope as is evident by the fluorescence throughout the volume of the nucleus. The 70 kDa dextrans are too large to pass through nuclear pores and results in primarily peripheral staining of the nucleus. This size exclusion of large dextrans was used to verify that the membranes of the isolated nuclei remain intact after dissection from the oocytes. Scale bars are 100 μm.

pressure was exerted on the nucleus, forcing a larger surface area of the membrane into the evanescent TIRF field while also preventing movement of the nucleus resulting from convection currents within the buffer. Using this approach, the transport of single dextrans through nuclear pores was observed through a 100X 1.45 N.A. objective and collected onto a Cascade 128+ CCD at a frame rate of 200 Hz over time periods of several seconds. Figure 6.2 shows a representative series of images collected at 5 ms time intervals, extracted from a 7 second series of frames. The appearance of a fluorescent event represents a Texas Red 10 kDa dextran entering a NPC and the disappearance of the signal corresponds to its release, presumably at the cytoplasmic face. Notice that the fluorescent events are limited to regions where the nuclear envelope resides within the evanescent excitation field. This indicates that the technique is insensitive to fluorescent molecules that are not slowed by confinement within NPCs, as the 5 ms exposure times of the CCD are too short to collect sufficient photons to detect molecules diffusing freely in the buffer. The specificity of the technique for transporting molecules was confirmed with the addition of 120 μM WGA, resulting in the rapid and dramatic decrease in observed events. As WGA is known to block transport through NPCs through binding the numerous FG domains within pore, this indicates that the previously observed events were in fact the result of fluorescent dextrans moving through NPCs and not molecules simply diffusing into and out of the evanescent field.

The individual transport times of the fluorescent dextrans were determined by first manually selecting events in the image sequences where transport occurred (a

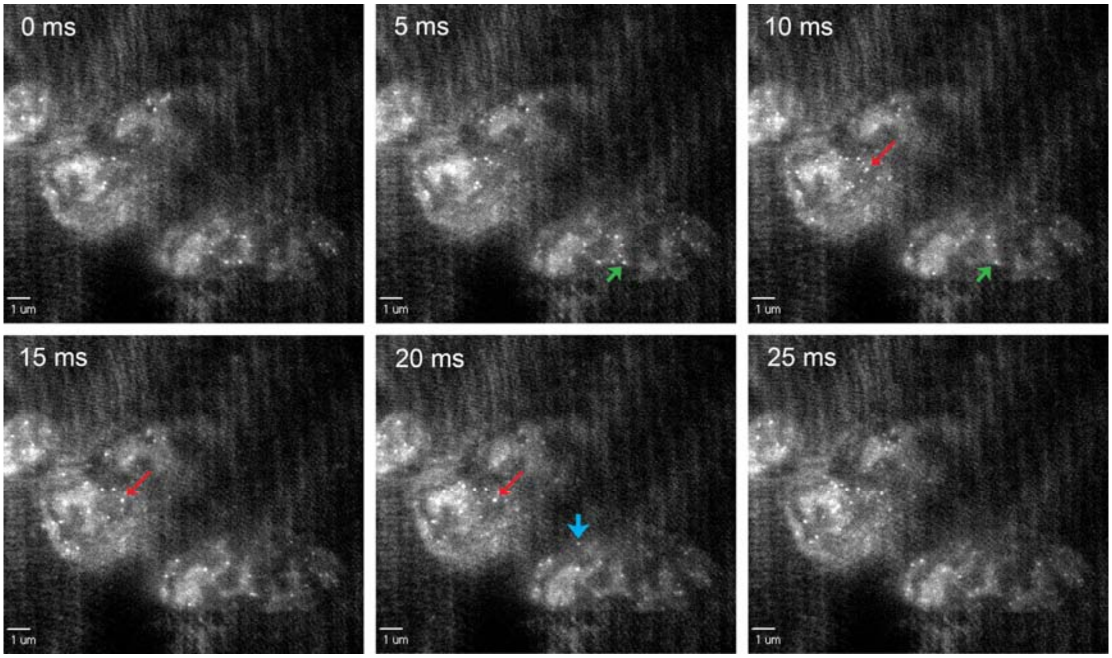

Figure 6.2 Sequence of fluorescence images visualizing transport events of 10 kDa fluorescent dextrans through NPCs. The regions of the membrane near the interface are seen as bright semicircular regions in the images as they are located within the TIRF evanescent field, while the dark background results from regions where the membrane resides beyond the excitation field. Individual transport events are recorded as the appearance and disappearance of diffraction-limited spots as outlined by the arrows. Monitoring the fluorescence intensity of these events as a function of time allows for the calculation of individual dwell times at NPCs. Scale bars are 1 μm.

diffraction limited fluorescent spot appeared and disappeared). The intensity of these pixels as a function of time was then plotted in AxoGraph. A representative trace is shown in Fig.6.3 where the short bursts of high fluorescence intensity represent individual transport events.

The traces such as those shown in Fig. 6.3 were analyzed to quantify individual dwell times for transport. This was done by measuring the full-width-at-half-maximum (FWHM) for all events exhibiting a peak amplitude greater than five times the calculated noise. Histograms of the dwell time distributions were created for both 10 kDa and 40 kDa dextrans. As shown previously,[19, 21] by fitting an exponential decay function to the histograms, lifetimes for the diffusion of the dextrans through NPCs were determined. Fig 6.4 shows the histograms and decay functions describing the dwell times of 10 kDa and 40 kDa dextrans to be 8.0 ± 0.4 ms and 7.2 ± 0.9 ms, respectively. These values are consistent with those found by other groups for transport of single fluorescent molecules.[19, 21]

Yang and Musser previously showed that the introduction of high levels of importin β resulted in decreased diffusion times of 10 kDa dextrans through NPCs.[21] This was attributed to a disruption of the FG network within the pore by importin β, allowing for less interaction between the dextrans and the reactive FG domains. We, and many others, have shown that the addition of WGA to the transport solution stops both active and passive movement through the pores as it tightly binds to the FG regions and likely occludes the NPCs.[31, 32] Interestingly, however, we found that short exposure to a dilute concentration of WGA (50 μg/ml) had contrary results.

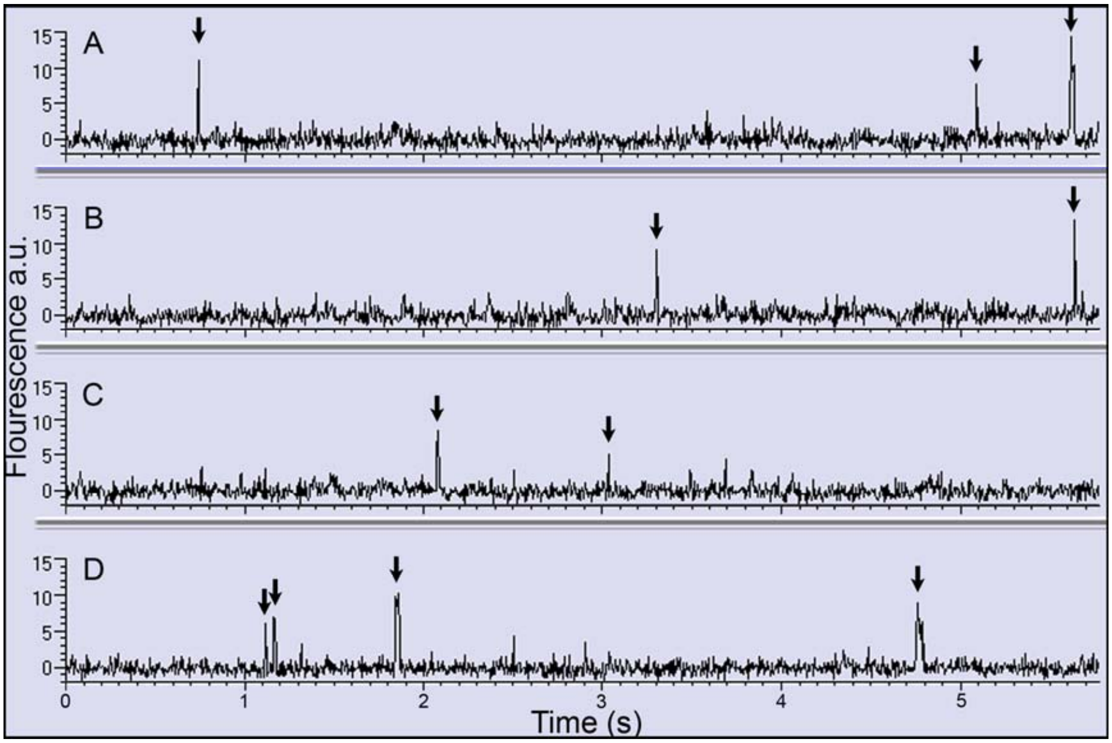

Figure 6.3 Traces of fluorescence intensity versus time of individual fluorescent dextrans transiting NPCs. The transport events within several traces are marked by arrows. The dwell times of individual events are determined by measuring the full-width-at-half-maximum intensity (FWHM) of the events.

Exposing nuclei containing 10 kDa dextrans to dilute WGA decreased the dwell time from 8.0 ± 0.4 ms to 5.1 ± 0.4 ms, indicating a shorter interaction time with NPCs. In the case of 40 kDa dextrans, however, the addition of WGA resulted in a dwell time of 6.7 ± 0.9 ms which is statistically similar to the 7.2 ± 0.9 ms dwell time measured prior to the addition of WGA. Histograms of individual events and the exponential fits used to determine the dwell times for 10 kDa and 40 kDa dextrans after the addition of dilute WGA are shown in Figs. 6.4C and 6.4D, respectively. A comparison of the dwell times for several dextrans as a function of WGA are outlined in Table 6.1.

These results, along with other recent studies,[21] suggest that non signal-mediated transport may not occur as simple diffusion through an open channel as previously believed. Rather, it is likely that even small molecules diffusing through nuclear pores may interact with the FG domains within NPCs. Although long incubations in high concentrations of WGA resulted in blocking diffusion of dextrans through NPCs, the addition of lower concentrations for shorter incubation times resulted in a significant decrease in the dwell times of 10 kDa dextrans, but had little effect the transport of 40 kDa dextrans.

This can most easily be explained by a transport mechanism such as the selective phase model in which the FG domains form a hydrogel-like network within the interior of the pore.[33] Small molecules are able to diffuse through the many openings of the sieve-like network while large molecules are excluded. In this model, it is easy to imagine that the addition of large amounts of WGA occludes the pore,

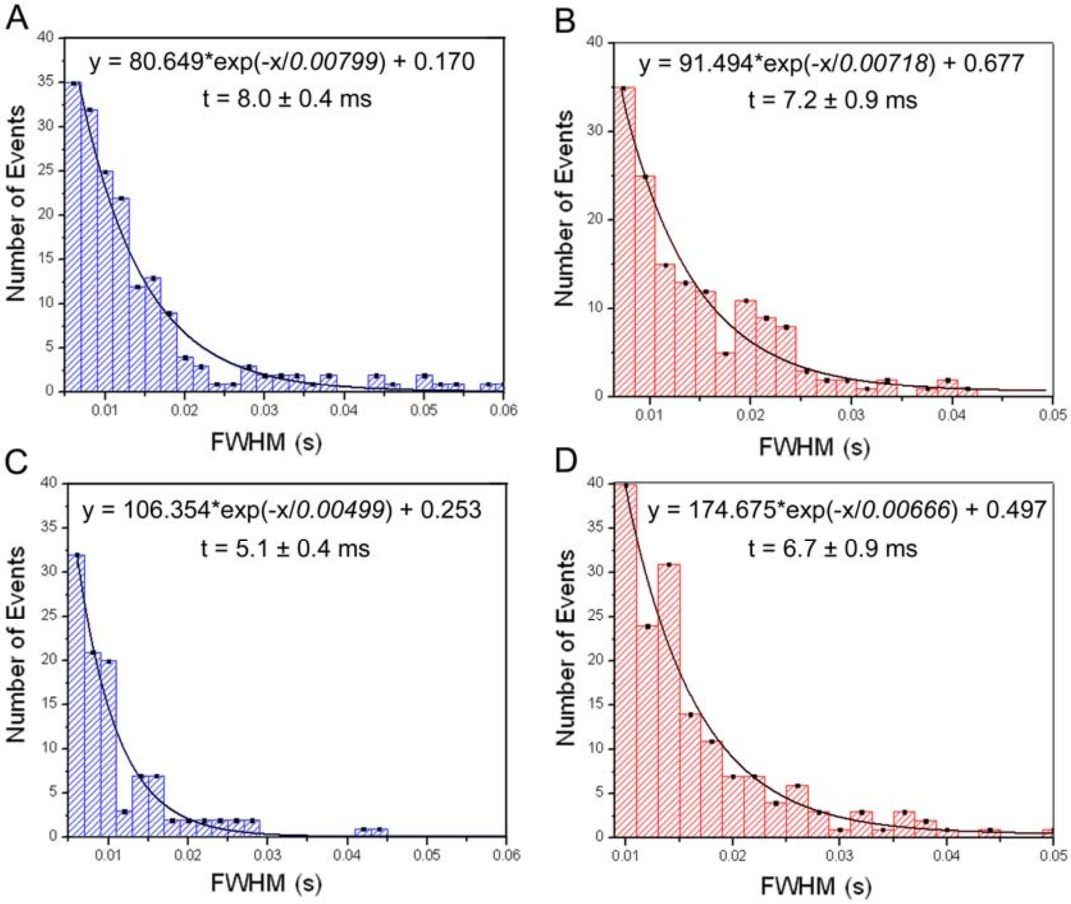

Figure 6.4 Histograms of the single-molecule transport times for fluorescent dextrans. The individual transport times were determined by measuring the FWHM of the intensity versus time traces shown in Fig. 6.3. Fitting the values with an exponential decay function resulted in calculated dwell times of 8.0 ± 0.4 ms and 5.1 ± 0..37 ms for (A) 10 kDa dextrans in buffer and (C) in50 μg/ml WGA. The fitting determined dwell times for the 40 kDa dextrans to be 7.2 ± 0.9 ms and 6.7 ± 0.9 ms for nuclei in (B) buffer and (D) in 50 μg/ml WGA. *All of the histograms were fit by single exponential decays.

Transport Molecule	**Treatment**	**NPC Dwell Time (ms)**
10 kDa Texas Red Dextrans	Modified Mock Buffer	8.0 ± 0.4
10 kDa Texas Red Dextrans	10 Min. 50 µg/ml WGA	5.1 ± 0.4
10 kDa Texas Red Dextrans	30 Min. 120 µg/ml WGA	NA*
40 kDa Texas Red Dextrans	Modified Mock Buffer	7.2 ± 0.9
40 kDa Texas Red Dextrans	10 Min. 50 µg/ml WGA	6.7 ± 0.9
40 kDa Texas Red Dextrans	30 Min. 120 µg/ml WGA	NA
70 kDa Texas Red Dextrans	Modified Mock Buffer	NA
70 kDa Texas Red Dextrans	10 Min. 50 µg/ml WGA	NA

Table 6.1 Results of the single-molecule dwell time analysis for several fluorescent dextrans. The measured dwell times for each condition are given in milliseconds. *NA indicated that no transport was observed under those conditions.

inhibiting transport entirely, while the addition of small amounts of WGA may cap off or passivate some of the FG domains within the pore. This would result in a reduction of nonspecific interaction with small cargo as it passes through the FG meshwork, resulting in an overall decrease in transit time as seen in the case of 10 kDa dextrans. For the larger 40 kDa dextrans, on the other hand, this would not necessarily hold true as several studies have shown that 40 kDa dextrans are at the upper size limit for passive diffusion through NPCs.[34] Because of the large size of 40 kDa dextrans, the passivation of some of the FG domains through the addition of small amounts of WGA would likely have little effect on the transit times, as the rate-limiting step involves the physical movement through the small meshwork rather than interaction with the FG domains. Although the results of these studies strongly implicate that diffusion of small molecules through NPCs is not only dependent on size, but also and interaction with the FG domains, it is clear that further work needs to be undertaken in order to verify the proposed mechanism.

6.5 Conclusions

The studies outlined in this chapter take advantage of previous single-molecule transport work and the novel implementation of TIRF-M to directly visualize and quantify non signal-mediated transport times of fluorescently conjugated dextrans through NPCs. By pre-loading intact isolated *X. laevis* oocyte nuclei with fluorescent dextrans of various sizes, export in small patches of membrane near the buffer/coverglass interface were monitored with TIRF-M. This not only decreased the background fluorescence resulting from the concentrated dextrans in the nucleoplasm, increasing the signal-to-noise, but the finite depth of the evanescent field from the coverglass allowed for an enhanced sensitivity to molecules transiting the NE near the interface. Furthermore, because of the large field of view afforded by detection with a CCD and the significant number of transport events recorded per analysis, large populations of transport events were collected for each study. From this, NPC dwell times for 10 kDa and 40 kDa dextrans were determined to be 8.0 ± 0.4 ms and 7.2 ± 0.9 ms, respectively. The addition of high concentrations of WGA was found to eliminate transport events while interestingly, incubation with small amounts of WGA had different effects on the various dextrans. Specifically, the dwell time of the 10 kDa dextrans was found to be reduced to 5.1 ± 0.4 ms while the dwell time of the 40 kDa dextrans was essentially unchanged at 6.7 ± 0.9 ms.

Though these results were puzzling at first, it appears that the trends in transport times are in good agreeance with other studies suggesting that the disruption of the FG network in NPCs facilitates passive transport of small dextrans.[21] These results are consistent with the decrease in dwell times that we observed upon addition of small amounts of WGA to nuclei containing 10 kDa dextrans. In the case of 40 kDa dextrans, which did not exhibit a change in dwell time upon addition of WGA, the rate-limiting factor may be related to physically navigating through the tight meshwork of FG domains rather than interaction with the domains themselves. This would result in little effect on dwell times by the addition of small amounts of WGA, as seen experimentally. These results would be expected for a gating mechanism such as that described by the selective phase model, which is based upon the premise that the FG domains within the pores form a hydrogel-like meshwork acting as a size-exclusion sieve for transported molecules.[33] Although these studies have helped to delineate the processes of passive diffusion through nuclear pores, a continuation of these studies involving numerous other non signal-mediated cargos and various physiological conditions such as depleted cisternal calcium levels would allow for further insights into these mechanisms.

6.6 Future Directions

Several single-molecule transport studies of large signal-mediated proteins have been instrumental in delineating important components involved in both active import and export through NPCs.[19, 21, 22] As an extension of the study above in which transport times were determined for various fluorescent dextrans through NPCs as a function of FG domain availability, we are further interested in active transport as a function of cellular signals. As outlined in the beginning of this chapter, bulk transport studies have implicated a number of important biological factors in the efficiency of cyto-nuclear transport.[10, 35, 36] For example, depletion of calcium from the cisternal space has been shown to hinder active transport through NPCs, although subsequent studies indicate contradictory results.[30, 37-40] By observing individual events, a clearer understanding of the effects of various stimuli on transport rates and efficiencies can be uncovered.

Extending these studies to explore the specific effects of cisternal calcium concentrations on NPC transport is important to clarify the contradictory results in the literature. Several bulk studies have found that the specific depletion of cisternal calcium through the activation of IP_3Rs hinders both active and non signal-mediated transport,[7, 30] though this was met with subsequent studies suggesting that altering calcium levels has little or no effect on transport.[39, 40] A direct view of single-molecule transport as a function of cisternal calcium levels would finally lead to a clear answer. Before these studies can begin, however, it is necessary to create a protocol for visualizing single-molecule nuclear transport in intact systems. Towards this goal, a BSA-Rhodamine construct labeled with a nuclear localization sequence was diluted in transport buffer and microinjected into live HASM cells with an injection time of 0.25 seconds and a pressure of 19 psi. The movement of the transport cargo was monitored by far-field excitation with a 568 nm laser line and fluorescence emission was collected through a 60X 1.45 N.A. objective and focused onto a Cascade 650 CCD. Figure 6.5 shows a sequence of time-lapse images collected following microinjection. While many of the BSA constructs are found randomly diffusing throughout the cytoplasm, individual molecules appear to interact with the NE prior to entry into the nucleus (large arrowhead). Fluorescent molecules located within the nucleoplasm provide further evidence for successful transport of the construct across the nuclear envelope (small arrowhead).

In an effort to explore yet another fluorescent transport construct, a more photostable allophycocyanin fluorophore conjugated with a NLS was also utilized.

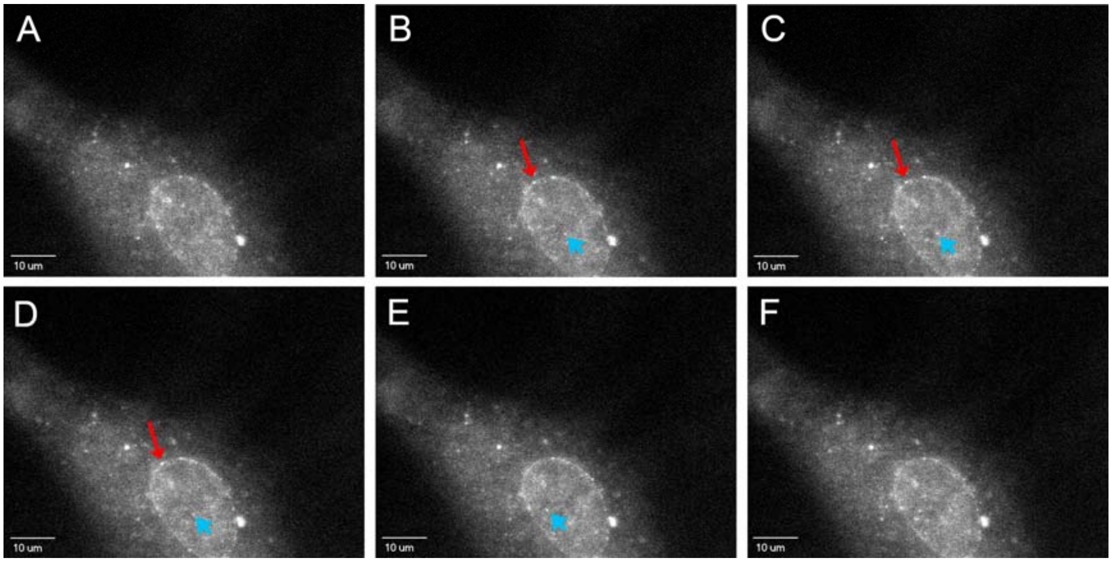

Figure 6.5 Representative sequence of fluorescence images depicting the distribution of a microinjected rhodamine-BSA-NLS transport complex within a live HASM cell. The larger red arrows identify an interaction of a single BSA complex with the nuclear envelope. The smaller blue arrows follow the movement of a single BSA complex within the nucleoplasm. Together, these events demonstrate that the rhodamine-BSA-NLS complex is capable of facilitated nuclear transport following microinjection into live cells. The scale bars are 10 μm and the images were collected at 90 ms intervals.

As with the BSA construct, a 0.25 second injection at 19 psi delivered small amount of the APC-NLS construct into the HASM cells. Figure 6.6 shows a sequence of images demonstrating the results of the microinjection of the APC-NLS solution into a HASM cell. The cell and nuclear membranes are visible in the transmission image taken prior to injection (Fig. 6.6A), while the distribution of the fluorescent cargo immediately following injection is apparent in Fig. 6.6B. Figure 6.6C was taken 5 minutes post-injection. The pattern of fluorescence immediately following injection (Fig. 6.6B) illustrates a homogeneous distribution through the cytoplasm though the nucleus appears to specifically exclude the complex. After five minutes, the APC-NLS conjugate appears to have successfully transited the nuclear envelope into the cell nucleus, as much of the fluorescence is now confined within the nucleoplasm (Fig. 6.6C). The high concentrations of APC-NLS that were injected into the cells and the far-field collection techniques did not allow for the visualization of single transport events, although we did discover that the cargo was successfully transported into the nucleus. To visualize single-molecule transport events of the APC-NLS construct, a significant decrease in the number of injected APC molecules will be necessary in order to reduce the background signal.

These active transport studies show promise as we have devised a protocol for injection, visualization, and transport of fluorescent cargo through NPCs, although they have proven difficult for a number of reasons. First, the cell nuclei reside beyond the reach of the evanescent field produced by TIR, precluding the use of TIRF-M for visualizing transport. As a result, the significant background from both

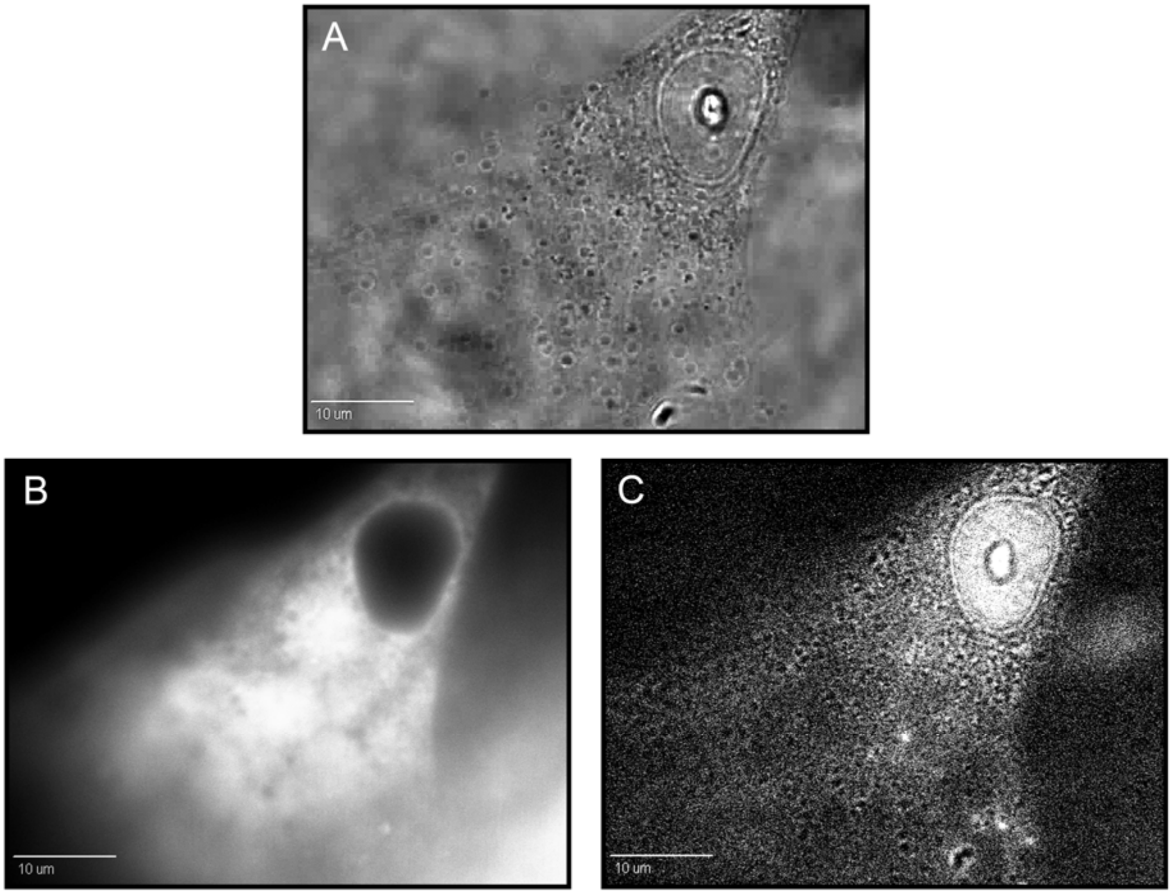

Figure 6.6 Series of images of a live HASM cell illustrating the cyto-nuclear transport of an APC-NLS complex. The borders of the cell and nucleus are clear in the transmission image (A). The fluorescence distribution of the APC-NLS transport complex immediately following microinjection (B) shows that the complex is homogenous throughout the cytoplasm and excluded from the nucleus. The distribution of the APC complex 5 minutes after injection (C) indicates significant redistribution of the APC complex as it has been effectively transported into the nucleus of the cell. The scale bars are 10 μm.

autofluorescence originating from the cell and fluorescent transport complexes outside of the focal plane make the signal-to-noise problematic for single-molecule studies. Second, the determination of dwell times at the nucleus is difficult as the absolute location of the NE is unclear and will likely require a second fluorescent label be introduced into the protocol. Finally, we find that the constant visualization of fluorescence distribution with the high laser powers necessary to locate single molecules rapidly photobleaches the fluorescent cargo complexes, further complicating these experiments. Despite the numerous difficulties listed above, overcoming these difficulties could lead to greater understandings of nuclear transport mechanisms and the factors controlling them.

6.7 References

(1) Erickson, E. S.; Mooren, O. L.; Moore-Nichols, D.; Dunn, R. C., Activation of ryanodine receptors in the nuclear envelope alters the conformation of the nuclear pore complex. *Biophys. Chem.* **2004,** 112, (1), 1-7.

(2) Moore-Nichols, D.; Arnott, A.; Dunn, R. C., Regulation of nuclear pore complex conformation by IP(3) receptor activation. *Biophys. J.* **2002,** 83, (3), 1421-8.

(3) Mooren, O. L.; Erickson, E. S.; Moore-Nichols, D.; Dunn, R. C., Nuclear side conformational changes in the nuclear pore complex following calcium release from the nuclear membrane. *Phys. Biol.* **2004,** 1, 125-134.

(4) Akey, C. W., Interactions and structure of the nuclear pore complex revealed by cryo-electron microscopy. *J. Cell Biol.* **1989,** 109, (3), 955-70.

(5) Beck, M.; Lucic, V.; Forster, F.; Baumeister, W.; Medalia, O., Snapshots of nuclear pore complexes in action captured by cryo-electron tomography. *Nature* **2007,** 449, (7162), 611-5.

(6) Fahrenkrog, B.; Stoffler, D.; Aebi, U., Nuclear pore complex architecture and functional dynamics. *Curr. Top. Microbiol. Immunol.* **2001,** 259, 95-117.

(7) Perez-Terzic, C.; Pyle, J.; Jaconi, M.; Stehno-Bittel, L.; Clapham, D. E., Conformational states of the nuclear pore complex induced by depletion of nuclear Ca2+ stores. *Science* **1996,** 273, (5283), 1875-7.

(8) Wang, H.; Clapham, D. E., Conformational changes of the in situ nuclear pore complex. *Biophys. J.* **1999,** 77, (1), 241-7.

(9) Hicks, G. R.; Raikhel, N. V., Protein import into the nucleus: an integrated view. *Annu. Rev. Cell. Dev. Biol.* **1995,** 11, 155-88.

(10) Peters, R., Fluorescence microphotolysis to measure nucleocytoplasmic transport and intracellular mobility. *Biochim. Biophys. Acta.* **1986,** 864, (3-4), 305-59.

(11) Bednenko, J.; Cingolani, G.; Gerace, L., Nucleocytoplasmic transport: navigating the channel. *Traffic* **2003,** 4, (3), 127-35.

(12) Fried, H.; Kutay, U., Nucleocytoplasmic transport: taking an inventory. *Cell Mol. Life Sci.* **2003,** 60, (8), 1659-88.

(13) Breeuwer, M.; Goldfarb, D. S., Facilitated nuclear transport of histone H1 and other small nucleophilic proteins. *Cell* **1990,** 60, (6), 999-1008.

(14) Richardson, W. D.; Mills, A. D.; Dilworth, S. M.; Laskey, R. A.; Dingwall, C., Nuclear protein migration involves two steps: rapid binding at the nuclear envelope followed by slower translocation through nuclear pores. *Cell* **1988,** 52, (5), 655-64.

(15) Ribbeck, K.; Gorlich, D., Kinetic analysis of translocation through nuclear pore complexes. *Embo. J.* **2001,** 20, (6), 1320-30.

(16) Jurkat-Rott, K.; Lehmann-Horn, F., The patch clamp technique in ion channel research. *Curr. Pharm. Biotechnol.* **2004,** 5, (4), 387-95.

(17) Keminer, O.; Peters, R., Permeability of single nuclear pores. *Biophys. J.* **1999,** 77, (1), 217-28.

(18) Keminer, O.; Siebrasse, J. P.; Zerf, K.; Peters, R., Optical recording of signal-mediated protein transport through single nuclear pore complexes. *Proc. Natl. Acad. Sc.i U S A* **1999,** 96, (21), 11842-7.

(19) Kubitscheck, U.; Grunwald, D.; Hoekstra, A.; Rohleder, D.; Kues, T.; Siebrasse, J. P.; Peters, R., Nuclear transport of single molecules: dwell times at the nuclear pore complex. *J. Cell Biol.* **2005,** 168, (2), 233-43.

(20) Siebrasse, J. P.; Peters, R., Rapid translocation of NTF2 through the nuclear pore of isolated nuclei and nuclear envelopes. *EMBO Rep.* **2002,** 3, (9), 887-92.

(21) Yang, W.; Musser, S. M., Nuclear import time and transport efficiency depend on importin beta concentration. *J. Cell Biol.* **2006,** 174, (7), 951-61.

(22) Yang, W.; Musser, S. M., Visualizing single molecules interacting with nuclear pore complexes by narrow-field epifluorescence microscopy. *Methods* **2006,** 39, (4), 316-28.

(23) Erickson, E. S., Characterization of Structural Changes Within the Nuclear Pore Complex and Development of Novel Methods Toward Understanding Pore Dynamics, University of Kansas, Lawrence, Kansas, September 2006.

(24) Fahrenkrog, B.; Aebi, U., The nuclear pore complex: nucleocytoplasmic transport and beyond. *Nat. Rev. Mol. Cell Biol.* **2003,** 4, (10), 757-66.

(25) Macara, I. G., Transport into and out of the nucleus. *Microbiol. Mol. Biol. Rev.* **2001,** 65, (4), 570-94, table of contents.

(26) Rout, M. P.; Aitchison, J. D.; Magnasco, M. O.; Chait, B. T., Virtual gating and nuclear transport: the hole picture. *Trends Cell Biol.* **2003,** 13, (12), 622-8.

(27) Ben-Efraim, I.; Gerace, L., Gradient of increasing affinity of importin beta for nucleoporins along the pathway of nuclear import. *J. Cell Biol.* **2001,** 152, (2), 411-7.

(28) Pyhtila, B.; Rexach, M., A gradient of affinity for the karyopherin Kap95p along the yeast nuclear pore complex. *J. Biol. Chem.* **2003,** 278, (43), 42699-709.

(29) Stewart, M.; Baker, R. P.; Bayliss, R.; Clayton, L.; Grant, R. P.; Littlewood, T.; Matsuura, Y., Molecular mechanism of translocation through nuclear pore complexes during nuclear protein import. *FEBS Lett.* **2001,** 498, (2-3), 145-9.

(30) Lee, M. A.; Dunn, R. C.; Clapham, D. E.; Stehno-Bittel, L., Calcium regulation of nuclear pore permeability. *Cell Calcium* **1998,** 23, (2-3), 91-101.

(31) Finlay, D. R.; Newmeyer, D. D.; Price, T. M.; Forbes, D. J., Inhibition of Invitro Nuclear Transport by a Lectin That Binds to Nuclear-Pores. *J. Cell Biol.* **1987,** 104, (2), 189-200.

(32) Cserpan, I.; Udvardy, A., The mechanism of nuclear transport of natural or artificial transport substrates in digitonin-permeabilized cells. *J. Cell Sci.* **1995,** 108 (Pt 5), 1849-61.

(33) Frey, S.; Richter, R. P.; Gorlich, D., FG-rich repeats of nuclear pore proteins form a three-dimensional meshwork with hydrogel-like properties. *Science* **2006,** 314, (5800), 815-7.

(34) Thorogate, R.; Torok, K., Ca2+-dependent and -independent mechanisms of calmodulin nuclear translocation. *J. Cell Sci.* **2004,** 117, (Pt 24), 5923-36.

(35) Bustamante, J. O.; Michelette, E. R.; Geibel, J. P.; Dean, D. A.; Hanover, J. A.; McDonnell, T. J., Calcium, ATP and nuclear pore channel gating. *Pflugers Arch* **2000,** 439, (4), 433-44.

(36) Wilson, G. L.; Dean, B. S.; Wang, G.; Dean, D. A., Nuclear import of plasmid DNA in digitonin-permeabilized cells requires both cytoplasmic factors and specific DNA sequences. *J. Biol. Chem.* **1999,** 274, (31), 22025-32.

(37) Greber, U. F.; Gerace, L., Depletion of calcium from the lumen of endoplasmic reticulum reversibly inhibits passive diffusion and signal-mediated transport into the nucleus. *J. Cell Biol.* **1995,** 128, (1-2), 5-14.

(38) Stehno-Bittel, L.; Luckhoff, A.; Clapham, D. E., Calcium release from the nucleus by InsP3 receptor channels. *Neuron* **1995,** 14, (1), 163-7.

(39) Enss, K.; Danker, T.; Schlune, A.; Buchholz, I.; Oberleithner, H., Passive transport of macromolecules through Xenopus laevis nuclear envelope. *J. Membr. Biol.* **2003,** 196, (3), 147-55.

(40) Wei, X.; Henke, V. G.; Strubing, C.; Brown, E. B.; Clapham, D. E., Real-time imaging of nuclear permeation by EGFP in single intact cells. *Biophys. J.* **2003,** 84, (2 Pt 1), 1317-27.

Chapter 7

Conclusions and Future Directions

7.1 Dissertation Summary

The breadth of the work outlined in this thesis is centered around probing the structure and function of the nuclear pore complex (NPC). NPCs are enormous (~125 MDa) protein structures that span the double bilayer membrane of the nuclear envelope (NE).[1, 2] As NPCs provide the only known route of transport both into and out of the nucleus, much effort has been expended toward understanding their structure and functional roles. As high-resolution electron microscopy (EM) and atomic force microscopy (AFM) imaging of NPCs began to dissect the complex structure of the NPC, one enigmatic component occasionally presented itself within the central channel of the complex.[3-8] The identity of the central mass has been unclear as many investigators have suggested that it may represent cargo transiting the pore,[3, 9] an integral part of the NPC,[10, 11] or even an artifact of the sample preparation method in which the filamentous nuclear basket collapses within the pore.[5, 12]

Given the transport function of NPCs and the results of several studies, including those outlined in this thesis, the central mass most likely represents cargo caught shuttling through nuclear pores. As many cellular components including ribosomes, RNAs, and histones, are known to cross the NE via NPCs, it is possible that the central mass is comprised of numerous constituents. However, similarities in size and shape to the central mass have led some to speculate that vault ribonucleoproteins may be involved, although direct evidence was lacking. These large, hollow ribonucleoproteins are expressed ubiquitously in nearly all eukaryotes although their precise functional roles remain unclear. Their large size, hollow nature, and link to multidrug resistance led to the speculation that they play important sequestering and shuttling roles within the cell.[13, 14] These implications of transport, along with their distinctly similar morphologies, have fostered a belief that vaults may represent the enigmatic central mass.[15, 16] If vault proteins not only represent the central mass, but are actively imported into the nuclei of various cell lines, one can imagine applications in treatments such as gene therapy and directed drug delivery.

The work described in the beginning of this thesis probed the relationship between vaults and NPCs in order to determine if the central mass is in fact comprised of vaults transiting nuclear pores. Firstly, transmission electron microscopy (TEM) found a significant spatial correlation between immunolabeled vaults and NPCs. In order to gain a quantitative insight into this relationship, Förster resonance energy transfer (FRET) measurements between vaults and NPCs were probed. The observed energy transfer confirmed a colocalization between vaults and NPCs As previous atomic force microscopy studies (outlined in Chapter 1) found that the relative location of the central mass within NPCs is highly dependent upon cisternal calcium concentrations, the energy transfer efficiencies between vaults and NPCs were investigated as a function of cisternal calcium levels as well, resulting in increasing FRET efficiencies with the decrease of cisternal calcium. This evidence not only strongly implicates an interaction between vault proteins and nuclear pore complexes, but further suggests that vaults represent the central masses of NPCs.

Though the FRET studies provide strong evidence for the interaction between vaults and NPCs, the nature of these bulk measurements were unable to directly visualize individual interactions at nuclear pores. The use of near-field scanning optical microscopy (NSOM) allowed for the direct observation of immunolabeled vaults in the high-resolution fluorescence channel and NPCs in the simultaneously collected force channel. Comparing the two channels specifically located the vast majority of individual vault particles specifically to NPCs. 2-color NSOM fluorescence studies were then carried out in which spectrally separated vault and NPC labels were both detected in high-resolution fluorescence channels. Correlation plots of the two fluorescence channels again confirmed a direct relationship between the location of vault proteins and NPCs, further suggesting that they specifically interact with one another. This ability to visualize single-particle interactions between vaults and NPCs supports the hypothesis that vaults specifically reside at nuclear pores, representing the controversial central mass.

The NSOM studies on NEs have proven valuable in discerning the relationship between vaults and NPCs and have been equally as useful in a number of other biological studies.[17, 18] Unfortunately, extending NSOM for use on fragile biological samples such as live cells has been a long difficult process. Chapter 3 outlines the adaptations and advancements necessary for extending near-field from solid state applications to biological samples. One of the major concerns for this transition revolved around possible thermal damage to biological samples as a result of NSOM probe heating. As excitation light passes toward the aperture of a NSOM probe, the loss of supported propagating modes results in the formation of a highly inefficient evanescent field. Modeling studies have determined that at this point, much of the light is directed back up the probe fiber while some continues toward the aperture, although the majority is absorbed into the metal coating and dissipated as heat.[19] Early studies indicated that probe temperatures reach extremes that would instantly ablate biological samples,[20, 21] although we knew this was not the case simply from the successful use of NSOM on the NPC samples above. However, the question as to the absolute temperature felt by a sample as it is scanned by an NSOM probe remained relevant. In order to investigate sample heating by NSOM, our group had previously developed a method in which NSOM probes produced by heating and pulling were maintained nanometers above a thermochromic polymer in order to directly probe sample heating, finding that temperatures did not exceed ~65 °C.[22] Though the mild temperatures encountered should pose little problem for use on biological samples, we investigated alternate probe designs in order to determine if even lower sample heating could be achieved.

Chemically etched NSOM probes are a popular alternative to those produced by heating and pulling as they exhibit much steeper tapers and higher light throughput efficiencies.[23, 24] We speculated that these increased efficiencies would result in less absorption of light into the aluminum coating and thus a reduced sample heating. In order to investigate this, the same perylene/NA polymer as used previously for pulled probes was prepared and spread onto a coverslip to be imaged by a series of NSOM probes fabricated by the chemical etching method. Surprisingly, the sample heating versus output power profiles for etched probes are strikingly similar to those produced by the less efficient pulled probes. Again, the sample temperature rapidly increased as a function of output power, reaching a maximum temperature of ~60 °C. This suggests that both pulled and etched probe designs impart similar heating onto the sample and that the modest temperatures should in fact be amendable with sensitive samples.

As an extension to the investigation of sample heating by NSOM probes, the mechanisms of light-induced failure were investigated for both heated and pulled and chemically etched NSOM probes. The consequence of probe failure resulting from coupling too much light into a NSOM tip is clear, although the underlying mechanisms have been debated, suggesting it occurs from either the differential elongation of the aluminum coating past the dielectric core or direct thermal damage of the metal coating.[24] Interestingly, both mechanisms are likely to be responsible, although they vary depending on the probe design itself. The long tapers of the pulled NSOM probes result in damage to the aluminum shell as a result of stresses induced through differential elongation. However, the shorter tapered regions of chemically etched NSOM probes decrease the magnitude of this elongation and allow for higher destruction thresholds and eventual failure due to direct thermal damage of the aluminum. In both cases, the loss of a well-defined aperture renders the probes useless, although the higher efficiencies and destruction thresholds of chemically etched probes may lead to further advances in NSOM afforded by greater power densities at the aperture.

Finally, dynamic studies of passive transport through NPCs were undertaken. Chapter 6 describes a novel method for probing transit times of individual fluorescent dextrans through nuclear pores in isolated *Xenopus laevis* oocyte nuclear envelopes. By utilizing TIRF-M, dwell times were determined for 10 kDa and 40 kDa dextrans passing through NPCs. We validated this method with the addition of high concentrations of wheat germ agglutinin (WGA), which arrested transport through binding to the FG domains within the pore. Surprisingly however, the addition of small amounts of WGA significantly reduced the dwell time for 10 kDa dextrans while the 40 kDa dextrans appeared to be unaffected. Though this obviously requires further investigation, it suggests that capping a small amount of the FG domains within the pore with WGA decreases the interactions felt by the small dextrans (10kDa), allowing them to pass through the pore more freely and rapidly. Alternatively, for the larger 40 kDa dextrans, the tight meshwork of FG domains described by the selective phase model would make their passage difficult under any conditions, likely not making interactions with the FG domains the rate limiting step. Rather, the physical movement through the small hydrogel-like mesh is responsible for the dwell times of non-signal mediated transport of molecules near the size cutoff for passive transport. In this case, the blocking of the FG domains would have little overall effect on the transport times, as seen experimentally.

7.2 Future Work

7.2.1 Probing the Effect of Inositol 1,4,5-trisphosphate Receptor Proximity on the Displacement of the NPC Central Mass Following IP$_3$ Receptor Activation

The importance of cisternal calcium levels on NPC structure and function has been shown in numerous studies as it was found to alter the physical properties of the NPC and possibly the permeability of NPCs to both actively and passively transported cargo.[7, 11, 25] The physiological release of calcium from within the cisternal region of the nuclear envelope and the ER is primarily achieved through the activation of 1,4,5-trisphosphate receptors (IP$_3$Rs) within the membrane. AFM studies have specifically shown the appearance and apparent displacement of the central mass within the NPCs to be extremely sensitive to the activation of IP$_3$Rs with the potent agonist Adenophostin A.[6, 8] Activation of IP$_3$Rs has been computationally determined to either result in calcium blips or puffs in which a single Ca^{2+} channel or small cluster of Ca^{2+} cannels are opened, respectively, although difficulties in measuring these events have arisen due to their small dimensions and rapid kinetics.[26]

Questions arise as to whether NPCs in close proximity to IP$_3$Rs react differently to receptor activation than those located a further distance away. If, in fact, there is a spatial dependence, it may provide a mechanism for the cell to regulate transport in certain regions of the nucleus while limiting it in others. It is known that NPCs are able to dynamically break down and assemble in the membrane, but orchestrating an organized rearrangement of NPCs in the NE would require significantly more effort than redistributing the much smaller IP$_3$Rs.

Future studies involving the use of both NSOM and AFM would enable measurements of NPC morphology, such as the location of the central mass within NPCs, as a function of distance to an IP_3R. Although AFM has proven capable of measuring the surface morphology of NPCs with high-resolution, its lack of selectivity makes locating the smaller IP_3Rs within the membrane difficult. However, preliminary NSOM data was collected in which fluorescent immunolabeled IP_3Rs within isolated *X. laevis* oocyte nuclear envelopes are located in the high-resolution fluorescence detection channel (Fig. 7.1) while the NPCs are identified in the in the simultaneously collected force image (Fig. 7.1A). As with the NSOM studies probing vault locations on the nuclear envelope, an overlay of the two channels allows for a direct comparison of the location and distribution of NPCs and IP_3Rs within a region of the NE (Fig 7.1C). As is apparent in Fig. 7.1A, although the force channel effectively located NPCs within the membrane, the lack of topographical resolution does not allow for the characterization of the central mass location within the NPCs. However, by imaging the same region of membrane with high-resolution AFM and correlating it with markers in the NSOM force channel, the high resolution fluorescent channel locating IP_3Rs could be directly compared to NPC morphology, thus discerning the effect of IP_3R proximity on NPCs.

7.2.2 Extending Single-Molecule Transport Studies

Chapter 6 discusses a series of experiments in which the passive transport of single fluorescent dextrans through NPCs was achieved. The studies were able to

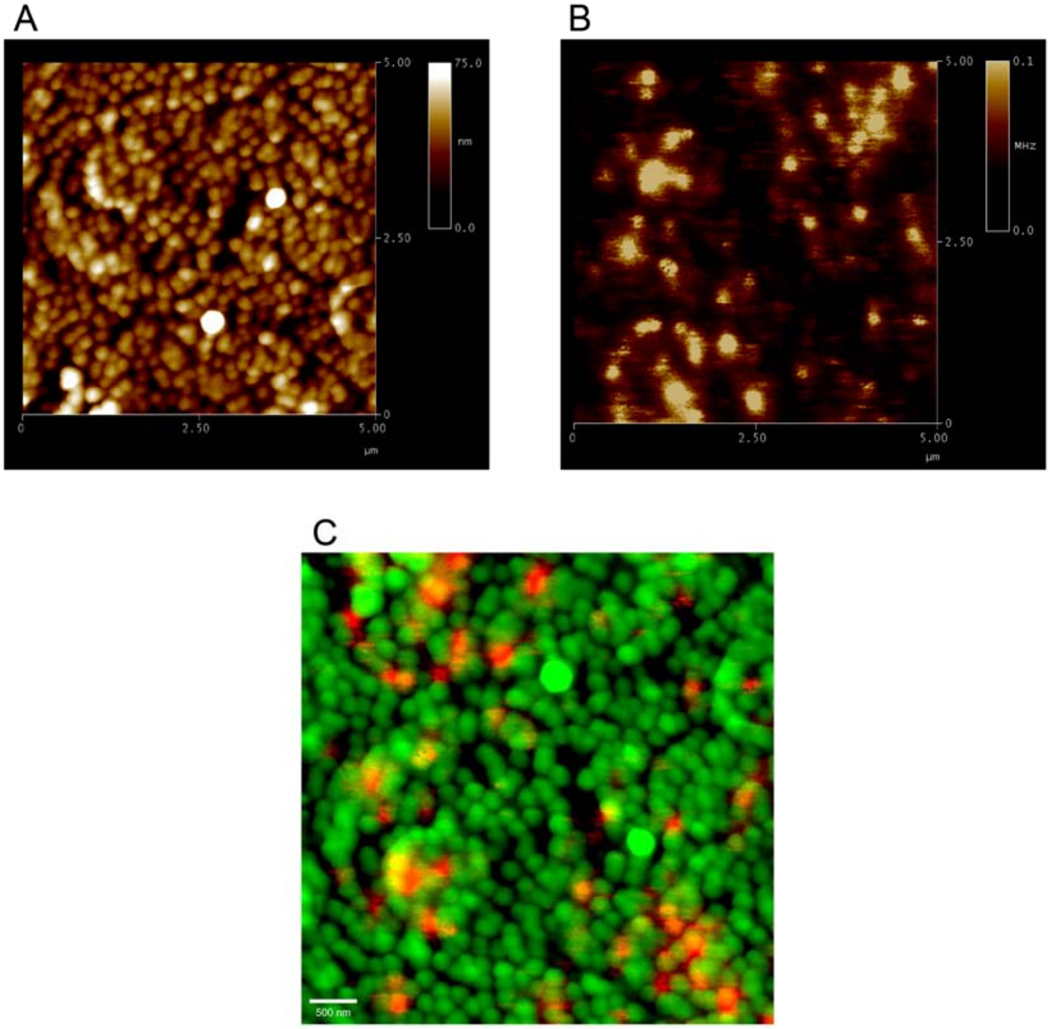

Figure 7.1 Simultaneously collected force (A) and fluorescence (B) NSOM images of a 5 µm x 5 µm region of nuclear membrane in which IP$_3$Rs have been fluorescently labeled. The NPCs are identified in the force image (A) and the IP$_3$Rs are simultaneously located in the high-resolution fluorescence channel (B). The overlay of the two (C) indicates that the small receptors (Red) in the membrane are distributed evenly and located in regions of the membrane between NPCs (Green). The scale bar is 500 nm.

discern small changes in NPC dwell times which likely would have been lost in bulk measurements. Chapter 6 also outlines the use and characterization of large signal mediated NPC transport cargos. Both BSA-Rhodamine-NLS and APC-NLS complexes were investigated and found to successfully cross the nuclear envelope following microinjection into live human arterial smooth muscle (HASM) cells. There are a number of single-molecule dynamics studies which could be investigated using the outlined transport protocols, with particular interest in the effects of cisternal calcium release on single NPC permeability and transport times. Bulk measurements of the effect of cisternal calcium levels on NPC permeability have been quite contradictory as several groups have suggested that is has drastic effects on NPC permeability and release of cisternal calcium essentially shuts down transport,[25, 27] while others suggest that it has no effect at all.[28, 29] The stark differences in experimental results likely result from not only variable experimental conditions, but also as a result of the bulk transport assays employed. The ability to quantitatively determine dwell times and transport efficiencies of single nuclear pores as a function of cisternal Ca^{2+} in a systematic manner will finally lead to a definitive answer as to the role of cisternal calcium on cyto-nuclear transport.

7.2.3 Utilizing NSOM for Real-Time Single-Molecule Optical Recording of Cyto-Nuclear Transport

As we have demonstrated, NSOM has the unique ability to resolve single NPCs within an isolated NE and through minor alterations to probe design and feedback mechanisms, it is capable of functioning in biologically benign conditions including buffered solutions. Chapter 5 exploited the simultaneous collection of high-resolution force and fluorescence data to locate vault proteins to individual nuclear pores. It would be interesting to couple the high-resolution fluorescence capabilities of NSOM with dynamic studies of cyto-nuclear transport. It is clear that the short dwell times of transiting cargo and the slow scan speeds of NSOM would not allow for the study of dynamic processes such as transport on a large area of membrane, but rather one could utilize the force channel to hover the NSOM probe over an individual pore while maintaining active feedback, as illustrated in Fig. 7.2. The detection of single transport events would then be collected as the transiting fluorescent cargo enters the excitation field of the NSOM probe. This technique would have several advantages over far-field collection as the recorded transport events would be definitively assigned to an individual NPC, even further decreasing any ambiguities from averaging. The TIRF-M technique utilized in Chapter 6 to collect single-molecule transport data relied on the membrane residing within ~200 nm from the surface in order to selectively excite fluorescent transport molecules with the evanescent field generated in TIRF. This was key in reducing background fluorescence to the point that single transport events could be recorded, but it raises the question as to what effects the proximity of the substrate has on transport. By placing the NSOM probe at the upper hemisphere of an isolated nucleus, any effects from the coverslip would be removed. Furthermore, the exponentially decaying intensity of the excitation field from the probe aperture would allow for the selective

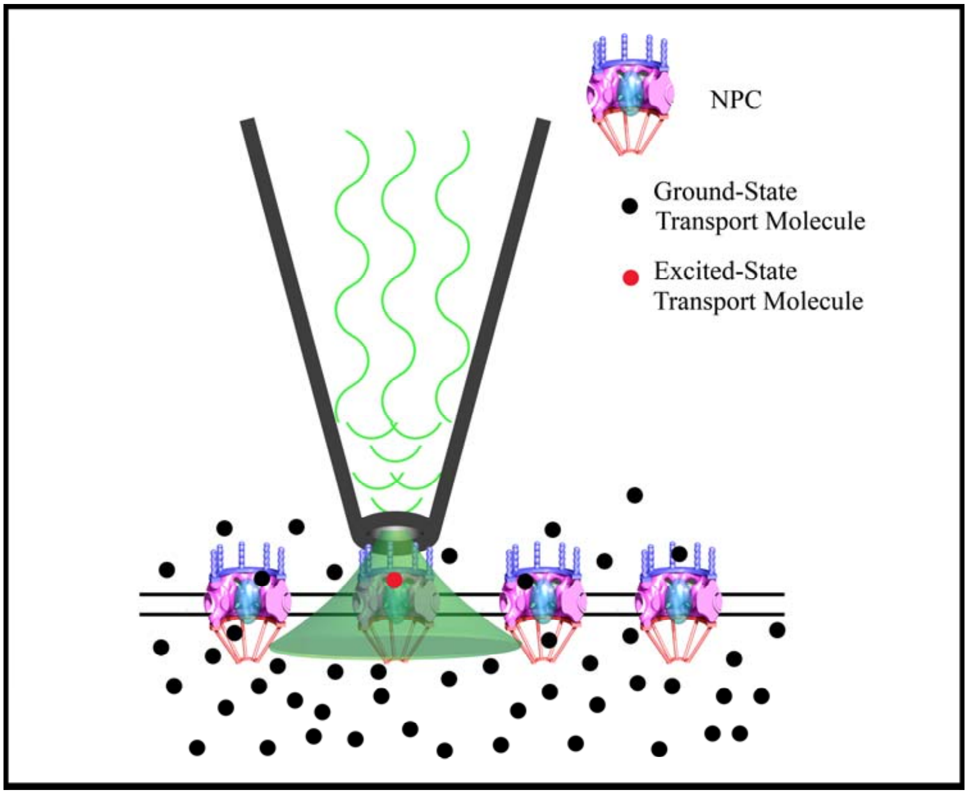

Figure 7.2 Illustration of a NSOM probe placed over a single nuclear pore. This configuration would allow for the detection of single-molecule transport events through a single NPC with the high spatial resolution afforded by NSOM.

excitation of fluorescent molecules at or very near the NPC of interest, reducing background and increasing signal-to-noise. This technique will admittedly suffer from low data collection as it is limited to a single nuclear more per collection series, but it is this resolution that will ultimately enable a true event-by-event analysis at an individual pore, thus allowing for an understanding of transport where the only variable is the condition under investigation.

7.3 References

(1) Reichelt, R.; Holzenburg, A.; Buhle, E. L., Jr.; Jarnik, M.; Engel, A.; Aebi, U., Correlation between structure and mass distribution of the nuclear pore complex and of distinct pore complex components. *J. Cell Biol.* **1990,** 110, (4), 883-94.

(2) Rout, M. P.; Wente, S. R., Pores for thought: nuclear pore complex proteins. *Trends Cell Biol.* **1994,** 4, (10), 357-65.

(3) Akey, C. W., Interactions and structure of the nuclear pore complex revealed by cryo-electron microscopy. *J. Cell Biol.* **1989,** 109, (3), 955-70.

(4) Erickson, E. S.; Mooren, O. L.; Moore-Nichols, D.; Dunn, R. C., Activation of ryanodine receptors in the nuclear envelope alters the conformation of the nuclear pore complex. *Biophys. Chem.* **2004,** 112, (1), 1-7.

(5) Fahrenkrog, B.; Stoffler, D.; Aebi, U., Nuclear pore complex architecture and functional dynamics. *Curr. Top. Microbiol. Immunol.* **2001,** 259, 95-117.

(6) Moore-Nichols, D.; Arnott, A.; Dunn, R. C., Regulation of nuclear pore complex conformation by IP(3) receptor activation. *Biophys. J.* **2002,** 83, (3), 1421-8.

(7) Wang, H.; Clapham, D. E., Conformational changes of the in situ nuclear pore complex. *Biophys. J.* **1999,** 77, (1), 241-7.

(8) Mooren, O. L.; Erickson, E. S.; Moore-Nichols, D.; Dunn, R. C., Nuclear side conformational changes in the nuclear pore complex following calcium release from the nuclear membrane. *Phys. Biol.* **2004,** 1, 125-134.

(9) Jarnik, M.; Aebi, U., Toward a more complete 3-D structure of the nuclear pore complex. *J. Struct Biol.* **1991,** 107, (3), 291-308.

(10) Akey, C. W., Visualization of transport-related configurations of the nuclear pore transporter. *Biophys. J.* **1990,** 58, (2), 341-55.

(11) Perez-Terzic, C.; Pyle, J.; Jaconi, M.; Stehno-Bittel, L.; Clapham, D. E., Conformational states of the nuclear pore complex induced by depletion of nuclear Ca2+ stores. *Science* **1996,** 273, (5283), 1875-7.

(12) Stoffler, D.; Goldie, K. N.; Feja, B.; Aebi, U., Calcium-mediated structural changes of native nuclear pore complexes monitored by time-lapse atomic force microscopy. *J. Mol. Biol.* **1999,** 287, (4), 741-52.

(13) Mossink, M. H.; van Zon, A.; Scheper, R. J.; Sonneveld, P.; Wiemer, E. A. C., Vaults: a ribonucleoprotein particle involved in drug resistance? *Oncogene* **2003,** 22, (47), 7458-7467.

(14) Suprenant, K. A.; Bloom, N.; Fang, J. W.; Lushington, G., The major vault protein is related to the toxic anion resistance protein (TelA) family. *J. Exp. Biol.* **2007,** 210, (6), 946-955.

(15) Slesina, M.; Inman, E. M.; Rome, L. H.; Volknandt, W., Nuclear localization of the major vault protein in U373 cells. *Cell Tissue Res.* **2005,** 321, (1), 97-104.

(16) van Zon, A.; Mossink, M. H.; Houtsmuller, A. B.; Schoester, M.; Scheffer, G. L.; Scheper, R. J.; Sonneveld, P.; Wiemer, E. A., Vault mobility depends in part on microtubules and vaults can be recruited to the nuclear envelope. *Exp. Cell Res.* **2006,** 312, (3), 245-55.

(17) Dunn, R. C., Near-Field Scanning Optical Microscopy. *Chem. Rev.* **1999,** 99, (10), 2891-2928.

(18) Edidin, M., Near-field scanning optical microscopy, a siren call to biology. *Traffic* **2001,** 2, (11), 797-803.

(19) Novotny, L.; Hafner, C., Light propagation in a cylindrical waveguide with a complex, metallic, dielectric function. *Phys. Rev. E. Stat. Phys. Plasmas Fluids Relat. Interdiscip. Topics* **1994,** 50, (5), 4094-4106.

(20) Rosa, A. H. L.; Yakobson, B. I.; Hallen, H. D., Origins and effects of thermal processes on near-field optical probes. *Appl. Phys. Lett.* **1995,** 67, (18), 2597-2599.

(21) Stahelin, M.; Bopp, M. A.; Tarrach, G.; Meixner, A. J.; Zschokke-Granacher, I., Temperature profile of fiber tips used in scanning near-field optical microscopy. *Appl. Phys. Lett.* **1996,** 68, (19), 2603-2605.

(22) Erickson, E. S.; Dunn, R. C., Sample heating in near-field scanning optical microscopy. *Appl. Phys. Lett.* **2005,** 87, (20), 201102.

(23) Moar, P.; Ladouceur, F.; Cahill, L., Numerical analysis of the transmission efficiency of heat-drawn and chemically etched scanning near-field optical microscopes. *Appl. Optics* **2000,** 39, (12), 1966-1972.

(24) Novotny, L.; Hecht, B., *Principles of Nano-Optics*. Cambridge University Press: New York, 2006; p 539.

(25) Lee, M. A.; Dunn, R. C.; Clapham, D. E.; Stehno-Bittel, L., Calcium regulation of nuclear pore permeability. *Cell Calcium* **1998,** 23, (2-3), 91-101.

(26) Swillens, S.; Dupont, G.; Combettes, L.; Champeil, P., From calcium blips to calcium puffs: Theoretical analysis of the requirements for interchannnel communication. *P. Natl. Acad. Sci. USA* **1999,** 96, (24), 13750-13755.

(27) Gorlich, D.; Kostka, S.; Kraft, R.; Dingwall, C.; Laskey, R. A.; Hartmann, E.; Prehn, S., Two different subunits of importin cooperate to recognize nuclear localization signals and bind them to the nuclear envelope. *Curr. Biol.* **1995,** 5, (4), 383-92.

(28) Enss, K.; Danker, T.; Schlune, A.; Buchholz, I.; Oberleithner, H., Passive transport of macromolecules through Xenopus laevis nuclear envelope. *J. Membr. Biol.* **2003,** 196, (3), 147-55.

(29) Wei, X.; Henke, V. G.; Strubing, C.; Brown, E. B.; Clapham, D. E., Real-time imaging of nuclear permeation by EGFP in single intact cells. *Biophys. J.* **2003,** 84, (2 Pt 1), 1317-27.